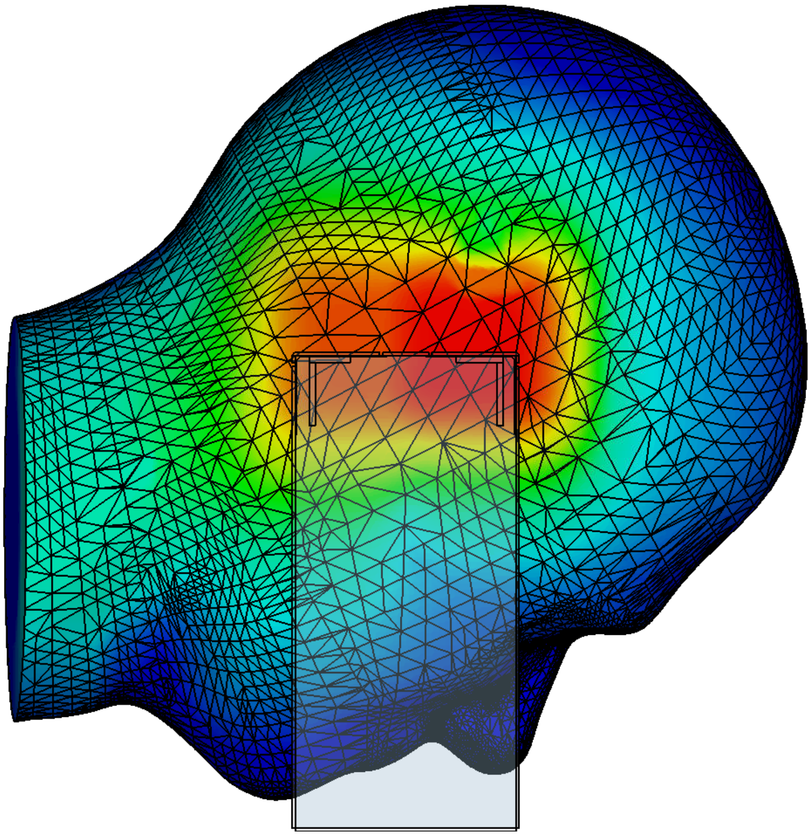

User Equipment antenna design for Non-Terrestrial Network communication

Design, Link budget and Electromagnetic field exposure evaluation for three different UE antennas

Master's thesis in Wireless, Photonic and Space Engineering

Gabriel Berggren

DEPARTMENT OF ELECTRICAL ENGINEERING
CHALMERS UNIVERSITY OF TECHNOLOGY
Gothenburg, Sweden 2026
www.chalmers.se

Master's thesis 2026

User Equipment antenna design for Non-Terrestrial Network communication

Design, Link budget and Electromagnetic field exposure evaluation for three different UE antennas

Gabriel Berggren

Department of Electrical Engineering
Antenna Systems Group
Chalmers University of Technology
Gothenburg, Sweden 2026

User Equipment antenna design for Non-Terrestrial Network communication
Design, Link budget and Electromagnetic field exposure evaluation for three different UE antennas
Gabriel Berggren

Supervisor: Jin Zhang, Stanislav Zhekov & Gang Zou, Ericsson AB
Examiner: Asharf Uz Zaman, Department of Electrical Engineering

Master's Thesis 2026
Department of Electrical Engineering
Antenna Systems Group
Chalmers University of Technology
SE-412 96 Gothenburg
Telephone +46 709 845 757

Cover: Specific absorption rate distribution on SAM phantom for the Bezel antenna

Typeset in LaTeX
Printed by Chalmers Reproservice
Gothenburg, Sweden 2026

User Equipment antenna design for Non-Terrestrial Network communication
Design, Link budget and Electromagnetic field exposure evaluation for three different UE antennas
Gabriel Berggren
Department of Electrical Engineering
Chalmers University of Technology

Abstract

Non-terrestrial networks (NTN) are emerging as an important component of future wireless communication systems, with 3GPP standardization efforts increasingly focused on enabling direct to device (D2D) connectivity for standard user equipment (UE). A key challenge in this context is the impact of different UE antenna designs on the link budget and regulatory compliance with electromagnetic field (EMF) exposure limits. This thesis addresses that challenge through a three part investigation of antenna design, EMF exposure assessment, and uplink link budget performance for NTN-capable UE. Three antenna designs were implemented and characterized at 3.5 GHz, a Bezel antenna, an inverted-F antenna (IFA), and a circularly polarized (CP) patch antenna. Key antenna parameters including peak realized gain and impedance bandwidth that were assessed and compared by simulations. EMF compliance was evaluated in terms of specific absorption rate (SAR) in accordance with IEEE/IEC standards and the impact of increasing transmit power to 26 dBm was also assessed. Uplink link budget analysis was subsequently performed for all three antennas and benchmarked against an isotropic radiator. Results indicate that the Bezel antenna provides the strongest link budget performance and all three antennas show compliance to EMF limits when power duty cycles are considered. The results collectively highlight a fundamental trade-off in NTN UE antenna design between ensuring EMF compliance and link performance, and provide quantitative data directly relevant to ongoing 3GPP standardization discussions. The findings suggest that transmit power class specifications for NTN UE cannot be decoupled from antenna design.

Keywords: UE Antenna, Electromagnetic field exposure, NTN, Link budget, Satellite communication, .

Acknowledgements

I would like to express my sincerest gratitude towards my supervisors at Ericsson, Jin Zhang, Stanislav Zhekov and Gang Zou for the many discussions and their unwavering support throughout this project. It has been an amazing experience to get to work on this research topic and to learn under your guidance. I would also like to thank my supervisor and examiner from Chalmers, Ashraf Uz Zaman for the genuine conversations, help and for making this thesis a possibility. I extend my warmest thanks to all my friends for making my time at Chalmers to such a memorable experience and finally, to my family for always supporting me.

Gabriel Berggren, Gothenburg, April 2026

List of Acronyms

Below is the list of acronyms that have been used throughout this thesis listed in alphabetical order:

16-PSK	Phase Shift Keying
3GPP	3rd Generation Partnership Project
8-PSK	8-Phase Shift Keying
AR	Axial Ratio
BER	Bit Error Rate
BPSK	Binary Phase Shift Keying
C/N_0	Carrier to Noise Density Ratio
CDF	Cumulative Distribution Function
CM	Common Mode
CNR	Carrier to Noise Ratio
CP	Circular Polarization
D2D	Direct to Device
DM	Differential Mode
EEA	European Economic Area
E_b/N_0	Energy Per Bit to Noise Spectral Density
EMF	Electromagnetic Field
ETSI	European Telecommunication Standards Institute
FCC	Federal Communications Commission
FSPL	Free Space Path Loss
G/T	Gain over System Noise Temperature
GEO	Geostationary Earth Orbit
GNSS	Global Navigation Satellite System
GSO	Geosynchronous Earth Orbit
HP	Horizontal Polarization
ICNIRP	International Commission on Nonionizing Radiation Protection
IEC	International Electrotechnical Commission
IEEE	Institute for Electrical and Electronical Engineers
IFA	Inverted F Antenna
ILA	Inverted L Antenna
ISED	Innovation, Science and Economic Development Canada
ITU	International Telecommunication Union

LE	Left Ear
LEO	Low Earth Orbit
LOS	Line of Sight
LP	Linear Polarization
MEO	Medium Earth Orbit
NLOS	Non-Line of Sight
NTN	Non-Terrestrial Network
OEM	Original Equipment Manufacturer
PEC	Perfect Electrical Conductor
PIFA	Planar Inverted F Antenna
PLF	Polarization Loss Factor
QPSK	Quadrature Phase Shift Keying
RE	Right Ear
RL	Return Loss
SAM	Specific Anthropomorphic Mannequin
SAR	Specific Absorption Rate
TEC	Total Electron Count
TN	Terrestrial Network
UE	User-Equipment
UHR	Upper Hemisphere Ratio
VP	Vertical Polarization
VSWR	Voltage Standing Wave Ratio
WLAN	Wireless Local Area Network

Contents

List of Figures

List of Tables

1

Introduction

This chapter presents the background for the thesis and introduces the aim.

1.1 Background

The mobile communication system have been evolving towards 5G, delivering high data rates, ultra-reliable low-latency communication, and near-ubiquitous connectivity across large portions of the globe [1]. Nevertheless, 5G remains fundamentally terrestrial in its architecture, relying on densely deployed base station networks that inherently limit coverage in remote environments such as rural regions, maritime corridors, and airspace [2].

Non-terrestrial networks (NTN) have emerged as a strategic solution to this coverage gap and are increasingly recognized as a foundational component of the forthcoming 6G system [2]. NTN communication introduces a distinct set of propagation challenges. Whereas conventional user equipment (UE) antennas are designed for terrestrial links spanning distances on the order of kilometres, NTN links must maintain stable communication with satellites operating at altitudes of hundreds to thousands of kilometres, across a wide range of elevation angles [3]. This gives rise to substantially greater free-space path losses and imposes new requirements on both the link budget and the antenna characteristics of the UE [4].

A cornerstone of the global telecommunications industry has been the role of standardization, which ensures interoperability between any compliant UE and any conforming network, regardless of vendor or geography. The principal bodies responsible for this work include the International Telecommunication Union (ITU), the European Telecommunications Standards Institute (ETSI), and the 3rd Generation Partnership Project (3GPP) [5]. With respect to NTN, 3GPP has conducted initial feasibility studies and begun establishing system-level requirements [4]. However, these efforts have largely relied on simplified antenna assumptions, in terms of radiation pattern, that may not accurately reflect the characteristics of current or future UE designs [6]. This represents a gap with potential impact in the standardization foundation, as antenna behaviour directly influences link performance, power requirements, and regulatory compliance.

Another critical dimension of this is the transmit power of the UE. The power class prevalent in current deployments is limited to 23 dBm, and investigating whether higher power classes could improve NTN link budgets is therefore, of practical interest [6]. However, any increase in transmit power must be evaluated against electromagnetic field (EMF) exposure that needs to be assessed against the internationally established limits to ensure compliance [7].

A further dimension of this investigation concerns the potential to utilize higher frequency bands for NTN operation. The frequency bands currently standardized by 3GPP for NTN in Release 17 and onwards are the n254- (Uplink: 1980 - 2010 MHz, Downlink: 2170 - 2200 MHz), n255- (Uplink: 1625.5 - 1660.5 MHz, Downlink: 1525 - 1559 MHz) and n256-band (Uplink: 1980 - 2010 Mhz, Downlink: 2170- 2200 Mhz) [4]. However, to avoid congestion, the industry continues to study the possibilities to expand to higher frequency bands [8].

1.1.1 Aim

The aim of this thesis is to design and simulate different UE antennas for the use in direct-to-device (D2D) NTN communication and to evaluate the power levels ensuring EMF compliance and the corresponding implications on the link performance.

2

Theory

This chapter will present all the necessary background information as well as the theory for understanding the report.

2.1 Non Terrestrial Networks

A NTN is considered to be a network utilizing uncrewed aircraft systems (UAS) such as unmanned aerial vehicles (UAV), high altitude platforms (HAPs) or satellites for communications purposes and has of recent become a discussed topic, both as part of 5G and 6G. The discussion of implementing NTN as a compliment to the terrestrial network (TN) began in 3GPP release 15 where the organization outlined use cases mainly focused on enhancing coverage and emergency communication from remote areas or relief during disaster events [4].

2.2 Satellite communication

This sections aims to explain the basics of satellite communication, starting from orbits and ending in the theory behind a communication link.

2.2.1 Orbits

Fundamental to satellite communication is understanding orbital mechanics and more specifically the implications of the orbital height. Based on Newtonian mechanics and Einstein theory of relativity the path of a satellite can be calculated with great precision given six initial conditions which can be described in two different ways, both of which will be supported in 3GPP. Firstly using position and velocity vectors (x, y, z) and (v_x, v_y, v_z) respectively or secondly using the so called six orbital elements; Semi-major axis (a), Eccentricity (e), Epoch of perifocus pass (t_p), Inclination of the orbital plane (i), Argument of perifocus (ω) and the Rectascension of the ascending node (Ω). Using these six elements we can describe the orbits that follows the three Kepler laws and are only valid for objects of much smaller size than the body which the orbits is around. For most astronautical efforts such as satellite orbits this approximation holds well [9].

Orbits around earth are mainly divided into three groups called low earth orbit

(LEO), medium earth orbit (MEO) and geostationary earth orbit (GEO). Each orbit comes with different characteristics which makes them more or less ideal for different purposes. GEO are circular orbits with an orbital height of 35 786 km above the earths equator and orbital period of one sidereal day, or 23 hours, 56 minutes which makes any object in a GEO appear stationary from an earth observer. This characteristic makes them ideal for purposes where the antenna on earth needs to be fix, such as for television broadcasting or when a specific area of the earth is of interest such as for weather satellites [10]. A distinct advantage of GEO satellites apart from their stationary nature is that only four satellites are necessary for true global coverage and their relatively low speed compared to other orbits give rise to minimal Doppler shifts [11]. GEO are a special subset of orbits pertaining to the class geosynchronous orbits (GSO) which share the same orbital height and period but can be inclined of the equatorial plane which makes the ground track a figure eight and thus returns to the same position in the sky for the same time of day but does not appear fix [12].

LEO are a group of inclined circular orbits that orbit around 180 km to 2000 km above the Earths surface where the upper limit is constrained such that the inner Van Allen belt is avoided and the lower limit is a consequence of Earths atmosphere. Satellites positioned in LEO have an orbital period of around 90 minutes which is an orbital velocity of 7.8 km/s with respect to earth. This velocity gives rise to significantly larger Doppler shifts than the GEO but simultaneously suffers much less delay in the signal propagation due to the much lower altitude. Since propagation delay is a physical constraint, LEO makes for an ideal candidate for communications systems that value low latency, such as voice or video calls. Whereas GEO constellations could achieve global coverage with only four satellites, the same would require hundreds of LEO satellites [10], [13]. Reduced launch costs and the development of small form factor LEO satellites still gives economy in large constellations as cost per satellite and launch is significantly reduced compared to their GEO counterpart [14].

The MEOs are positioned in between the LEO and GEO, but again with emphasis on avoiding the Van Allen belts. Most of our navigation satellites resided in these orbits as they offer a middle ground between needing large constellations, cost and delay [10].

2.2.2 Payload

The payload of a satellite refers to the internal components that are used for the mission specific purpose while the satellite bus refers to the vehicle itself, i.e. propulsion, power supply, telemetry, tracking and command, etc. For communications satellite there are two subtypes of payloads, transparent and regenerative. A transparent or bent-pipe payload acts as a radio repeater which receives the signal and transmits it back to earth at the correct frequencies thus also allowing any noise to propagate throughout the link. Regenerative payloads are capable of signal processing onboard the satellite which allows for isolation between the uplink and downlink signal and capabilities beyond simply amplifying and returning the signal. The key difference being the superior performance for the regenerative payload not allowing noise from the uplink to propagate to the downlink by recovering the baseband signal and remodulating it for transmission in the downlink. However, this comes at the expense of increased complexity and cost, power demands and less flexibility as each system is design only for selected data formats [15].

2.2.3 Link budgets

For satellite communication systems it is of great importance to assure oneself of the systems performance before launching the satellite into orbit and the prevailing tactic is to evaluate the systems link budget which tracks the power level of the signal from transmission to reception. The fundamental equation in wireless communication is the so called Friis equation which evaluates the received power according to:

$$P_{rx} = \frac{P_{tx}G_{tx}G_{rx}\lambda^2}{(4\pi d)^2} \tag{2.1}$$

where P_{tx} and P_{rx} is the transmitted power and received power, respectively, G_{tx} and G_{rx} are the gains of the transmitting and receiving antenna, respectively, λ is the carrier wavelength and d is the distance between the transmitter and receiver. The term:

$$\frac{(4\pi d)^2}{\lambda^2} \tag{2.2}$$

here shown inverted compared to equation 2.1 is called the free space path loss (FSPL) and causes the largest attenuation in a satellite communication system. For a system operating at 3.5 GHz in a 600 km LEO orbit and GEO orbit the FSPL values in dB are 159 dB and 194 dB, respectively.

The distance between the UE and satellite is not constant and fluctuates with elevation angle. The elevation angle is defined as the angle between the horizon and the satellite and is illustrated in figure 2.1. The distance d, often refereed to as slant range can be calculated using equation 2.3 where R_E is the radius of the earth, α is the elevation angle and h_0 is the orbital height of the satellite.

$$d = \sqrt{R_E^2 sin^2(\alpha) + h^2 + 2hR_E} - R_E\sin(\alpha) \tag{2.3}$$

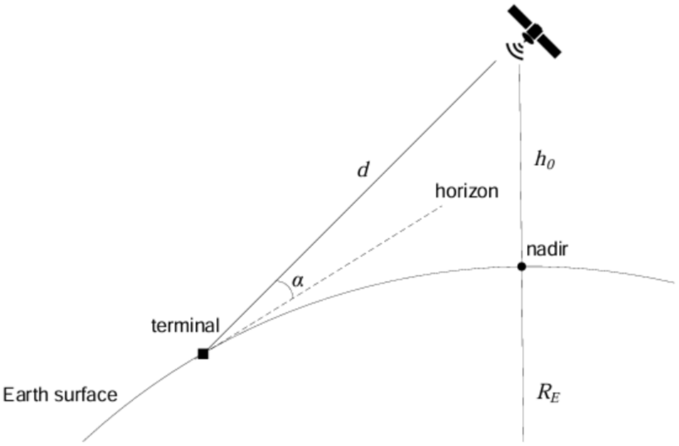

Figure 2.1: Schematic drawing of slant range [16]

To assess the communication link, the noise in the system should be considered therefore, the metric carrier to noise ratio (CNR or C/N) or the carrier to noise density ratio (C/N_0) which relates the carrier power level to the noise power level (N) or noise power density (N_0), respectively is used [17]. The C/N and C/N_0 is defined as

$$C/N = P_{rx} - P_L - N \tag{2.4}$$

$$C/N_0 = P_{rx} - P_L - N_0 \tag{2.5}$$

, respectively where P_L is a lumped term representing all losses in the system, which will be explained in later sections, N and N_0 can be calculated as:

$$N = kTB \tag{2.6}$$

$$N_0 = kT \tag{2.7}$$

where k is the Boltzmann constant, T is the system noise temperature and B is the bandwidth of the signal. The CNR allows for characterization of the overall quality of the link by describing how well the carrier can be discriminated from the noise. Another closely related metric is the energy per bit to noise spectral density (E_b/N_0) which is the ratio of energy in one bit to the noise power density. E_b/N_0 is related to CNR via

$$\frac{C}{N} = \frac{E_b}{N_0}\frac{R_b}{B} \tag{2.8}$$

where E_b is the energy per bit and R_b is the bit rate. This metric allows for comparison between the bit error rate (BER) and the effectiveness of digital modulation schemes without considering actual bandwidth allowing insights into performance of power limited systems [17].

BER is the ratio between faulty bits to total transmitted bits and for modern day communication systems the targeted number is dependent on the application, however for D2D the lowest acceptable BER is typically between 10^{-5} or lower [18]. In figure 2.2 the relation between BER and E_b/N_0 is shown for different modulation schemes and as shown higher order schemes require higher E_b/N_0 for the same BER compared to lower order schemes.

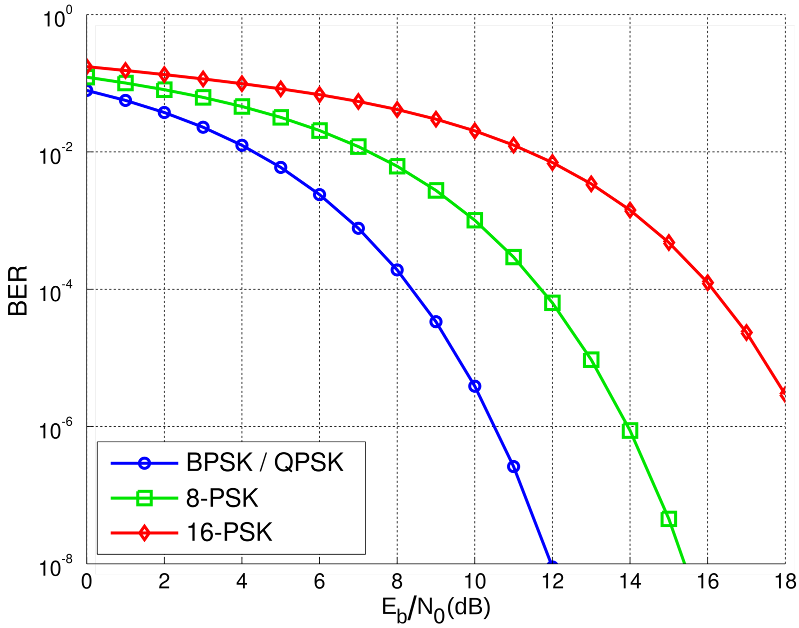

Figure 2.2: BER versus E_b/N_0 for lower order digital modulation schemes [19].

2.2.4 Noise

From the previous section it is noted that the performance of the link is dependent on the noise which is related to the system noise temperature T. The concept of a noise temperature is related to blackbody radiation where sources noise power is equated to that of a blackbody of temperature T which equals said noise power. The system noise temperature is a lumped term that accounts for all noise sources in the receiving system and is measured by convention at the input of the receiver, marked with an arrow as seen in figure 2.3 [20]. The system noise temperature can be calculated according to

$$T = (T_{ant} + T_{FD.in})(1/L_{FD}) + T_{rx.in} \tag{2.9}$$

where T_{ant} is the antenna temperature which is the noise temperature the antenna picks up and not the physical temperature of the antenna itself. $T_{FD.in}$ is the effective temperature of the feeder measured at the input of the receiver, L_{FD} is the attenuation in the feed and $T_{rx.in}$ is the cascaded temperature of the entire receiver chain measured at the input. In figure 2.3 the receiver chain is limited to a Low noise amplifier (LNA), down converter (DC), and IF amplifier.

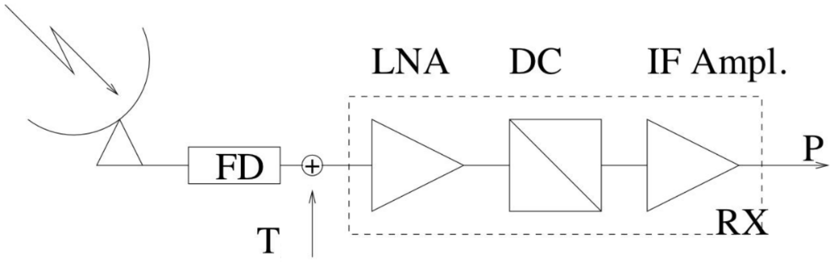

Figure 2.3: Schematic drawing of an earth station receiver[20].

The antenna temperature is dependent on the brightness temperature T_b of an object in the view of the antenna and the gain of the antenna in the objects direction, thus the temperature can be obtained by integrating the product over a sphere [21]:

$$T_{ant} = \int_0^{2\pi} \int_0^{\pi} G(\theta, \phi) T_b(\theta, \phi) sin(\theta) d\theta d\phi \tag{2.10}$$

An important metric used in satellite communication is a ratio called antenna gain to system noise temperature G/T which relates the antenna gain to the system noise temperature measured at the receiver input [22]. Its importance lies in characterizing the quality of the receiving station and also signifies an important area of improvement in communication system where the uplink is power limited as a higher gain and lower noise temperature can yield significant performance enhancements.

More commonly is for components or systems to be given using the noise figure F, which relates to the noise temperature T as:

$$F = 1 + \frac{T}{T_0} \tag{2.11}$$

where T_0 is the reference temperature set to 290 K.

2.2.5 Atmospheric effects

One important attenuator to consider is earths atmosphere. The impact of the atmosphere is highly frequency dependant. One such dependence is due to absorption from atmospheric gases, mainly oxygen, with peak absorption at 60 GHz and water vapour that peaks at 22 GHz [23]. Figure 2.4 illustrates the opacity of the atmosphere and also shows that there are gaps in the atmosphere where certain frequencies are less affected, such as those in the radio frequency domain.

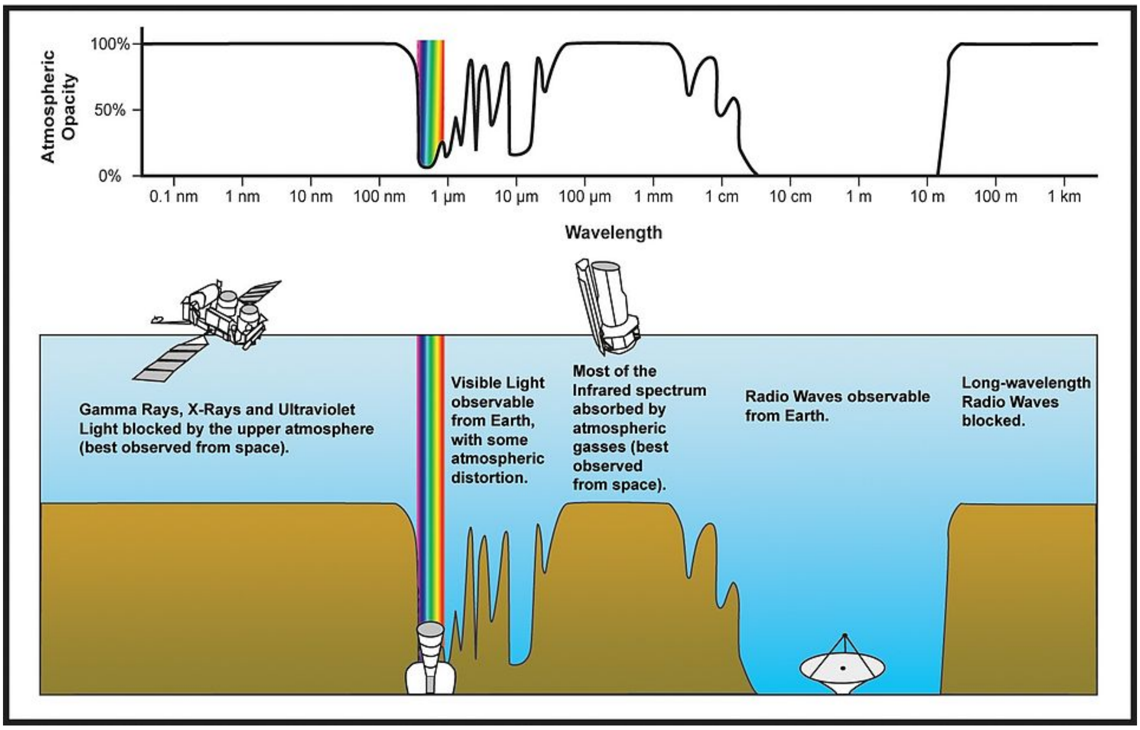

Figure 2.4: Atmospheric opacity as a function of wavelength [24]

The atmosphere can be subdivided into layers based on dominating effects and conditions. Two layers which are of importance are the Ionosphere and Troposphere. The Ionosphere ranges from around $80 - 5000\,\mathrm{km}$ from earths surface and consists of predominantly atomic oxygen as well as free electrons and plasma. The chemical makeup of the Ionosphere makes it behave as a dispersive media which will make the refractive index frequency dependant affecting the phase and group velocity of the incoming wave. Dispersive media also has an attenuating effect and a phase shifting effect which corresponds to a slight increase in path length. Another effect, which is influenced by the total electron content (TEC) and earth's magnetic field is the so-called Faraday rotation which causes a rotation of the state of polarization in linearly polarized electromagnetic waves [23].

The Troposphere extends from the surface up to around 10 km and contains the majority of all the atmospheres water vapour and weather phenomena. Rain and other forms of precipitation becomes the dominating issue at this level as it both absorbs and scatters energy, especially for frequencies above 10 GHz [23]. Since rain is not a constant occurrence, it's impact on communication links has to be dealt with statistically and is often calculated with respect to probability of link failure and is frequency dependant [23] [25].

2.3 Microwave theory

This sections aims to provide the necessary theoretical framework to understand design decisions as well as the fundamental working principles of radiating structures such as antennas.

2.3.1 Electromagnetic field theory

The understanding of electromagnetic field theory is central to the field of antenna engineering, therefore a short introduction follows. Large portions of the following sections are based on the two books, *Microwave Engineering* by Pozar [26] and *Foundations of antenna engineering, a unified approach for line of sight and multipath* by Kildal [27].

2.3.1.1 Maxwells equations

Most fundamental to understanding electromagnetic fields are Maxwells equations, which are a set of four coupled equations that, combined describe the behaviour of electromagnetic fields. Here presented in their time varying differential form in equation 2.12:

$$\nabla \cdot \mathbf{E} = \frac{\rho}{\epsilon_0} \qquad \text{(Gauss' law)} \tag{2.12a}$$

$$\nabla \cdot \mathbf{B} = 0 \qquad \text{(Gauss' law for magnetism)} \tag{2.12b}$$

$$\nabla \times \mathbf{E} = -\frac{\partial \mathbf{B}}{\partial t} \qquad \text{(Faraday's law)} \tag{2.12c}$$

$$\nabla \times \mathbf{B} = \mathbf{J}\mu_0 + \frac{\partial \mathbf{E}}{\partial t}\epsilon_0\mu_0 \qquad \text{(Ampère–Maxwell law)} \tag{2.12d}$$

where $\mathbf{E}$ is the electric field, $\mathbf{B}$ is the magnetic flux density, ρ is the electric charge density, ϵ_0 is the permittivity of free space, μ_0 is the permeability of free space and $\mathbf{J}$ is the current density. The set of equations can analogously be describe in their integral form. Another way to express the equations is via related fields like the electric flux density $\mathbf{D}$:

$$\mathbf{D} = \epsilon_0\mathbf{E} + \mathbf{P} = \epsilon\mathbf{E} \tag{2.13}$$

where $\mathbf{P}$ is the electric polarization and ϵ is the permittivity and the magnetic field $\mathbf{H}$:

$$\mathbf{H} = \frac{1}{\mu_0}\mathbf{B} - \mathbf{M} \tag{2.14}$$

For most applications in microwave engineering the only time variance is of sinusoidal or harmonic nature whereby it is convenient to express this set of equations in complex form using phasors:

$$\nabla \cdot \mathbf{E} = \rho \tag{2.15a}$$

$$\nabla \cdot \mathbf{B} = 0 \tag{2.15b}$$

$$\nabla \times \mathbf{E} = -j\omega\mathbf{B} - \mathbf{M} \tag{2.15c}$$

$$\nabla \times \mathbf{H} = j\omega\mathbf{D} + \mathbf{J} \tag{2.15d}$$

where j is defined as:

$$j = \sqrt{-1} \tag{2.16}$$

and ω is the radian frequency. The current density is related to the electric field via

$$\mathbf{J} = \sigma \mathbf{E} \tag{2.17}$$

where σ is the conductivity. From this definition, combining with the expansion of the permittivity into a real and imaginary part $\epsilon = \epsilon' - j\epsilon''$ where the imaginary part accounts for losses, equation 2.15d becomes

$$\nabla \times \mathbf{H} = j\omega(\epsilon' - j\epsilon'' - j\frac{\sigma}{\omega})\mathbf{E} = j\omega\epsilon'\mathbf{E} + (\omega\epsilon'' + \sigma)\mathbf{E} \tag{2.18}$$

where the term $\omega\epsilon'' + \sigma$ can be considered as the total effective conductivity and a ratio can be defined as

$$\tan\delta = \frac{\omega\epsilon'' + \sigma}{\omega\epsilon'} \tag{2.19}$$

which is called the loss tangent. Dielectric materials are often characterized by their loss tangent and another quantity called relative permittivity ϵ_r, defined as:

$$\epsilon' = \epsilon_r \epsilon_0 \tag{2.20}$$

2.3.1.2 Boundary conditions

The previous section describes electromagnetic fields in free space and expands into dielectric media, however, to understand the effects at the intersection of two media, boundary conditions are required. These boundary conditions can be derived from Maxwells equation by investigating what happens in a enclosed infinitesimally small volume at the intersection between two mediums. One group of such medium which is of importance to microwave engineering is good conductors such as metals, often considered to be lossless. For the idealised case of a perfect electrical conductor (PEC), all fields inside of the conductor are zero which yields the following set of conditions:

$$\hat{n} \cdot \mathbf{D} = \rho_s \tag{2.21a}$$

$$\hat{n} \cdot \mathbf{B} = 0 \tag{2.21b}$$

$$\hat{n} \times \mathbf{E} = 0 \tag{2.21c}$$

$$\hat{n} \times \mathbf{H} = \mathbf{J_s} \tag{2.21d}$$

where $\hat{n}$ is the normal vector to the surface, ρ_s and $\mathbf{J_s}$ are the electric surface charge density and current distribution, respectively. These equations states that the tangential component of the electric field and the normal component of the magnetic field are extinguished at the interface.

For the general case of a non PEC interface the equations expands to:

$$\hat{n} \cdot (\mathbf{D_2} - \mathbf{D_1}) = \rho_S \tag{2.22a}$$

$$\hat{n} \cdot \mathbf{B_2} = \hat{n} \cdot \mathbf{B_1} \tag{2.22b}$$

$$(\mathbf{E_2} - \mathbf{E_1}) \times \hat{n} = \mathbf{M_s} \tag{2.22c}$$

$$\hat{n} \times (\mathbf{H_2} - \mathbf{H_1}) = \mathbf{J_S} \tag{2.22d}$$

where $\mathbf{M_s}$ is the magnetic surface current density and the subscripts 1 and 2 denote two arbitrary mediums 1 and 2. These equations state that the normal component of the electric flux density is shifted by an amount equal to the surface charge density, and in the case of a lossless dielectric with $\rho_s = 0$ it's continuos across the boundary. Similarly the normal of the magnetic flux density is always continuos across the boundary. The tangential component of the electric field is for most mediums continuos across the boundary as $\mathbf{M_s} = 0$, however the magnetic field is affected by the surface current density.

2.3.1.3 Wave equation and plane waves

The behaviour of electromagnetic waves can be derived from Maxwells equations by taking the curl of the result from 2.15c and 2.15d under the conditions of a source free, linear, isotropic and homogenous region, which yields the result:

$$\nabla^2 \mathbf{E} + \omega^2 \mu \epsilon \mathbf{E} = 0 \tag{2.23}$$

which is called the Helmholtz equation or the wave equation. Following the same logic an expression can be derived for the H-field:

$$\nabla^2 \mathbf{H} + \omega^2 \mu \epsilon \mathbf{H} = 0 \tag{2.24}$$

Expanding this into a more general region can be done by first considering the term $\omega^2 \mu \epsilon$ which we can call k and is commonly referred to as the propagation constant and replacing it with another complex propagation constant

$$\gamma = \alpha + j\beta = j\omega\sqrt{\mu\epsilon}\sqrt{1 - j\frac{\sigma}{\omega\epsilon}} \tag{2.25}$$

where α is the attenuation constant, β is the phase constant. Considering a wave travelling in the z-direction of a Cartesian coordinate system and an E-field containing only components along the x-axis, the wave equation simplifies to

$$\frac{\partial^2 E_x}{\partial z^2} - \gamma^2 E_x = 0 \tag{2.26}$$

which has the solution:

$$E_x(z) = E^+ e^{-\gamma z} + E^- e^{\gamma z} \tag{2.27}$$

consisting of a superposition of the forward and backwards travelling waves where E^+ and E^- denote amplitude constant of the forward and backwards component, respectively. The associated H-field is expressed as

$$H_y(z) = \frac{-j\gamma}{\omega\mu}(E^+ e^{-\gamma z} - E^- e^{\gamma z}) \tag{2.28}$$

These assumptions form the basis for the mathematical concept of a plane wave which have the properties of entirely planar wavefronts with equal amplitude and phase.

2.3.2 Transmission lines

Transmission line theory is the bridge between the computationally heavy field analysis and circuit theory. The necessity for the theory becomes apparent when considering the size of components and the electrical wavelength of the signal, as in conventional circuit theory the size of the components are significantly smaller than the wavelength, whereas at microwave frequencies this is no longer the case and circuit theory is no longer applicable.

2.3.2.1 Transmission line model

Transmission lines are modelled using two wire lines as the condition for wave propagation demands at least two conductors and their behaviour can not adequately be described by a single lumped inductor, capacitor, or resistor. However, a infinitesimally small length Δz can be modelled as a lumped element circuit. Using Kirchoff's laws on said circuit two important results can be derived:

$$V(z) = V_0^+ e^{-\gamma z} + V_0^- e^{\gamma z} \tag{2.29a}$$

$$I(z) = I_0^+ e^{-\gamma z} + I_0^- e^{\gamma z} \tag{2.29b}$$

where $V(z)$, $I(z)$ are the voltage and current, respectively and V_0 and I_0 are amplitude constants. This means that both the voltage and the current can be represented as travelling waves along the transmission line, here assuming the direction of propagation is along the z-axis. Akin to ohms law, the so called characteristic impedance Z_0 of the line can be expressed as the ratio between the voltage and current as follows:

$$\frac{V_0^+}{I_0^+} = Z_0 = \frac{-V_0^-}{I_0^-} \tag{2.30}$$

For practical applications, transmission lines have to be connected to a load, such as an antenna with it's own load impedance Z_L which will reflect the incoming wave back such that

$$V_0^- = \frac{Z_L - Z_0}{Z_L + Z_0} V_0^+ \tag{2.31}$$

The amount of reflections can be determined by the ratio

$$\Gamma = \frac{V_0^-}{V_0^+} = \frac{Z_L - Z_0}{Z_L + Z_0} \tag{2.32}$$

where Γ is the reflection coefficient. This imposes a condition on the line. To achieve zero reflections back, Γ has to be zero, meaning that $Z_L = Z_0$ and the load is said to be matched to the line. When the load is not perfectly matched, not all of the energy is transferred to the load and the amount of this loss of power is defined as the return loss (RL), given in dB as:

$$RL = -20 \log_{10} |\Gamma| \tag{2.33}$$

When a forward travelling wave is reflected in a load mismatch, the superposition of incident and reflected waves creates a standing wave pattern along the transmission line. The voltage standing wave ratio (VSWR) is defined as the ratio of the maximum to minimum voltage amplitude along the line:

$$VSWR = \frac{V_{max}}{V_{min}} = \frac{1+|\Gamma|}{1-|\Gamma|} \tag{2.34}$$

which is a number between 1 and infinity, with $VSWR = 1$ implies a perfectly matched load.

2.3.2.2 Scattering matrix

At microwave frequencies, it is often impractical to measure total voltages and currents at circuit ports, therefore its beneficial to characterize the system in terms of incident, reflected and transmitted waves. One such way is via the so called scattering matrix which provides complete knowledge of the system as seen from any port.

Consider an N-port linear system. Let the incident wave be defined by the vector

$$\mathbf{V}^+ = \begin{bmatrix} V_1^+ \\ V_2^+ \\ \vdots \\ V_N^+ \end{bmatrix}$$

and the reflected wave amplitudes by:

$$\mathbf{V}^- = \begin{bmatrix} V_1^- \\ V_2^- \\ \vdots \\ V_N^- \end{bmatrix}.$$

The scattering matrix $\mathbf{S}$ is defined by the linear relation

$$\mathbf{V}^- = \mathbf{S}\mathbf{V}^+. \tag{2.35}$$

Explicitly,

$$\begin{bmatrix} V_1^- \\ V_2^- \\ \vdots \\ V_N^- \end{bmatrix} = \begin{bmatrix} S_{11} & S_{12} & \cdots & S_{1N} \\ S_{21} & S_{22} & \cdots & S_{2N} \\ \vdots & \vdots & \ddots & \vdots \\ S_{N1} & S_{N2} & \cdots & S_{NN} \end{bmatrix} \begin{bmatrix} V_1^+ \\ V_2^+ \\ \vdots \\ V_N^+ \end{bmatrix}. \tag{2.36}$$

Each scattering parameter is defined as

$$S_{ij} = \left.\frac{V_i^-}{V_j^+}\right|_{V_k^+=0,\, k\neq j}, \tag{2.37}$$

that is, the ratio of the outgoing wave at port i to the incident wave at port j, with all other ports terminated by matched loads (i.e., $V_k^+ = 0$ for $k \neq j$).

For passive systems like an antenna element, the S_{11} is the return loss and since it is highly frequency dependent, it is often hard to achieve a good return loss for a large bandwidth. For antenna systems a $S_{11} < -10\,\text{dB}$ corresponding to a VSWR of about 1.9 is considered acceptable at the centre frequency. The frequency range for which the system achieves an S_{11} below $-10\,\text{dB}$ is called the impedance bandwidth. Systems that operate with lower efficiencies, like phones often target $-6\,\text{dB}$.

2.3.3 Antenna theory

This section aims to elucidate some of the core concepts of antennas and antenna engineering which have their origin in Maxwells equations and are based on [27].

2.3.3.1 Field regions

From previous sections it is already noted that at a far enough distance from a source, waves behave as plane waves. This distance from the source is defined as the far field region:

$$r > \frac{2D^2}{\lambda} \tag{2.38}$$

where r is the distance from the source and D is the diameter of the smallest sphere encompassing all structural elements of the antenna. For r smaller than equation 2.38, the region is called the near field and can be further subdivide into two regions, the reactive near field and the radiating near field. The former is closest to the antenna element, whereas the latter makes up the rest.

Assuming a wave is propagating along the z-axis in the far field region, the polarization of the electromagnetic wave can be used to encode different signals on different polarizations. To detect the desired signal, the system thus has to be able to differentiate between the two polarizations and the desired polarization is called the co-polar, whereas the undesired is called the cross-polar. The polarization is defined with respect to the electric field. The desired component of the electric field, denoted E_{co}, is aligned with the co-polar unit vector $\hat{\mathbf{co}}$. Similarly, the cross-polar component E_{xp} is aligned with the cross-polar unit vector $\hat{\mathbf{xp}}$. The general expression of $\hat{\mathbf{co}}$ and $\hat{\mathbf{xp}}$ in a Cartesian coordinate system is defined for an angle ξ

$$\hat{\mathbf{co}} = \cos\xi\hat{\mathbf{x}} + \sin\xi\hat{\mathbf{y}} \tag{2.39a}$$

$$\hat{\mathbf{xp}} = \sin\xi\hat{\mathbf{x}} + \cos\xi\hat{\mathbf{y}} \tag{2.39b}$$

where two notable cases are for $\xi = \pi/2$ and $\xi = 0$ gives polarization aligned with the y- and x-axis in a Cartesian coordinate system, respectively. The definitions in equation 2.39 relates to linear polarization and from convention in antenna engineering, the polarization parallel to the ground is referred to as the horizontal polarization and the orthogonal then referred to as the vertical polarization.

Similarly, circular polarization can be defined by

$$\hat{\mathbf{co}} = \frac{\hat{\mathbf{x}} - j\hat{\mathbf{y}}}{\sqrt{2}} \tag{2.40a}$$

$$\hat{\mathbf{xp}} = \frac{\hat{\mathbf{x}} + j\hat{\mathbf{y}}}{\sqrt{2}} \tag{2.40b}$$

Equation 2.40 is for the case of right hand circular polarization (RHCP), similarly left hand circular polarization (LCHP) is defined by

$$\hat{\mathbf{co}} = \frac{\hat{\mathbf{x}} + j\hat{\mathbf{y}}}{\sqrt{2}} \tag{2.41a}$$

$$\hat{\mathbf{xp}} = \frac{\hat{\mathbf{x}} - j\hat{\mathbf{y}}}{\sqrt{2}} \tag{2.41b}$$

If we define the electric field as:

$$\mathbf{E} = (E_{co}\hat{\mathbf{co}} + E_{xp}\hat{\mathbf{xp}})e^{-jkz} \tag{2.42}$$

where e^{-jkz} is a propagation factor, then the co- and cross-polar components can be found as

$$E_{co} = \mathbf{E} \cdot \hat{\mathbf{co}}^* \tag{2.43a}$$

$$E_{xp} = \mathbf{E} \cdot \hat{\mathbf{xp}}^* \tag{2.43b}$$

Circular polarization is a special case of elliptical polarization and characterization of wave can thus be done in terms of the maximum and minimal values of the electric field strength of the wave in a ratio called the axial ratio (AR) in dB

$$AR = 10\log_{10}|\frac{E_{max}}{E_{min}}|^2 \tag{2.44}$$

where an AR of 0 dB is an ideal circularly polarized wave and an AR of ∞ dB is linearly polarized. For practical engineering purposes an AR below 3 dB is often taken as acceptable for circular polarization in literature. An AR above 3 dB then indicates an elliptically polarized wave.

2.3.3.2 Antenna parameters

Antennas that can radiate power in all directions, are called isotropic antennas and antennas that concentrate more power in a certain direction, are called directive antennas. The ratio between the radiated power in a direction compared to the isotropic case is defined as the directivity D of the antenna. A closely related parameter is the realized gain G of an antenna which depends on the directivity and the efficiency of the antenna system:

$$G = \varepsilon_{ant}D \tag{2.45}$$

where ε_{ant} denotes the realized efficiency of the antenna. Both directivity and gain have angular dependencies which relate to the far field pattern $\mathcal{G}(\theta, \phi)$ as:

$$\mathcal{D}(\theta, \phi) = 10\log_{10}(4\pi|\mathcal{G}(\theta, \phi)|^2/P) \tag{2.46}$$

where P is the radiated power in the isotropic case and $\mathcal{D}$ is the directional gain.

The far field function $\mathcal{G}$ describes how the radiated power is distributed over the unit sphere and relates to the electric field as

$$\mathbf{E}(r, \theta, \phi) = \frac{1}{r}e^{-jkr}\mathcal{G}(\theta, \phi) \tag{2.47}$$

where r is the distance from the antenna and k is the wave number. Depending on the geometry and current distribution of the antenna, the resulting far-field pattern may take on different forms. Omnidirectional patterns exhibit uniform radiation all planes perpendicular to the antenna axis, broadside radiation patterns direct maximum power perpendicular to the antenna axis or plane and endfire patterns radiate strongest along the axis of the antenna, achieving maximum radiation in the forward or backward direction. Hemispherical pattern are constrained to one side of the unit sphere.

2.3.3.3 Arrays

Antenna arrays are formed by combining multiple radiating elements in a controlled geometric arrangement to achieve radiation characteristics that cannot be obtained from a single antenna alone. The overall far field pattern of an array can be expressed as the product of the element far field function and the array factor:

$$\mathcal{G}_A(\hat{\mathbf{r}}) = \sum_{n=1}^{N} A_n e^{j\Phi_n}\mathcal{G}(\hat{\mathbf{r}})e^{jk\mathbf{r_n}\cdot\hat{\mathbf{r}}} \tag{2.48}$$

where the array factor (AF) is the term

$$AF(\hat{\mathbf{r}}) = \sum_{n=1}^{N} A_n e^{j\Phi_n} e^{jk\mathbf{r_n}\cdot\hat{\mathbf{r}}} \tag{2.49}$$

A_n is the amplitude and Φ_n is the phase of the excitation of element n. This equations holds for arrays with identical individual elements. By adjusting these excitation parameters, arrays enable control over main beam direction and beamwidth, making them highly versatile for applications requiring directional enhancement or tracking. By combining far fields of multiple elements, arrays can achieve higher gain than their single element counterpart.

2.3.4 Antenna types

This section aims to describe the fundamentals of the radiating structures considered in this thesis.

2.3.4.1 Microstrip patch antennas

Microstrip patch antennas are among the most common antenna types, in part due to their good performance but also their low fabrication cost. They have hemispherical radiation patterns, typically achieve lower gains around 6 dBi and can achieve both linear and circular polarization in a low volume form factor. However, they have limitations, such as narrow bandwidth and large ohmic and dielectric losses [28].

The microstrip patch antenna consists of a ground plane, substrate and a metallic patch, commonly feed either by a microstrip line or coaxial cable, as shown in figure 2.5. The radiating mechanism can be understood from transmission line theory where microstrip lines share many similarities. For microstrip lines, a thin substrate with high dielectric constant will limit the radiation coming off the line, thus for a patch antenna the opposite is desirable. The main driver of the radiation comes from the fringing fields which add in phase along the top of the patch whereas the current on the top of patch is mirrored on the ground plane, effectively cancelling out radiation from current sources [28][30].

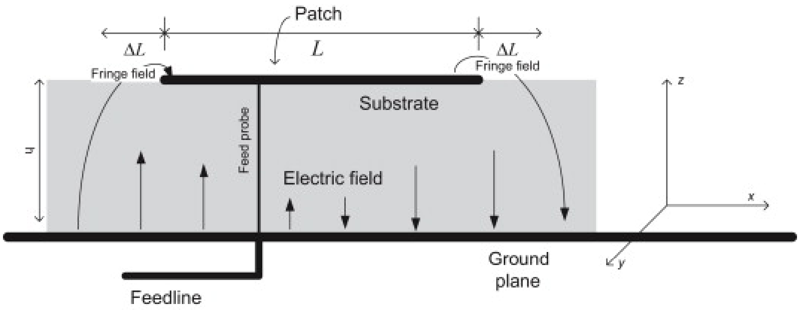

Figure 2.5: Schematic view of a rectangular microstrip patch antenna with fields visible [29].

The microstrip patch can be modelled as an open ended transmission line and the resonance frequency can be determined as

$$f_r = \frac{c}{2(L+\Delta L)\sqrt{\epsilon_{eff}}} \tag{2.50}$$

where c is the speed of light in vacuum, L is the patch length, ΔL is the electrical length added due to the fringing fields, and ϵ_{eff} is the effective permittivity of the substrate. Both ΔL and ϵ_{eff} has been empirically determined as

$$\Delta L = 0.412h\frac{\epsilon_{eff}+0.300}{\epsilon_{eff}-0.258}\frac{W/h+0.0264}{W/h+0.813}$$

(2.51)

$$\epsilon_{eff} = \frac{\epsilon_r+1}{2}\frac{\epsilon_r-1}{2}(1+12\frac{h}{W})^{-1/2} \tag{2.52}$$

where h is the height of the substrate, W is the width of the patch and ϵ_r is the relative permittivity of the substrate [28].

2.3.4.2 Inverted F antennas

Two of the most common antenna types found in phones are the inverted F antenna (IFA) and the planar inverted F antenna (PIFA), shown in figure 2.6. The basic geometry of both antennas is a element parallel to the ground and a short connected to the ground, with the feed offset from the short.

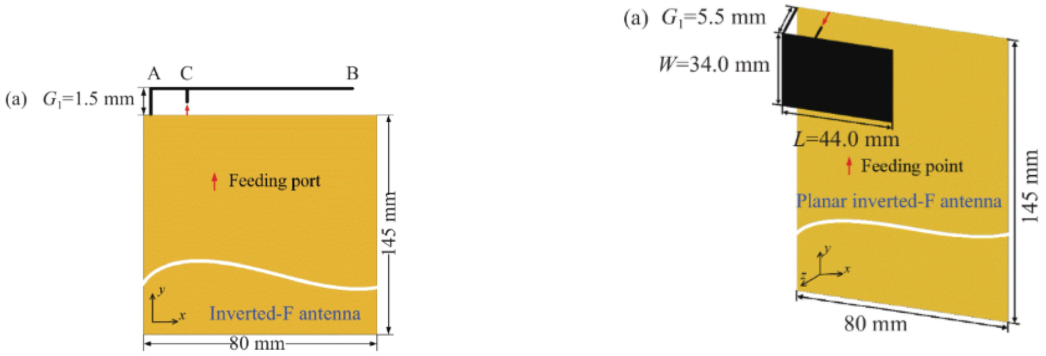

(a) Schematic drawing of an IFA

(b) Schematic drawing of an PIFA

Figure 2.6: Schematic drawing of the basic geometry for the IFA and PIFA antenna element [31].

The basic radiating properties of the IFA is that of a monopole which radiates at a quarter wavelength with odd multiples of the fundamental frequency also available. The radiation pattern given by an IFA is typically directional with heavy influence from the ground plane whereas the PIFA displays a more omnidirectional pattern. Both variations main advantage is their low profile and in the case of the IFA, ability to be etched directly onto the PCB which have made them a staple in modern phones and internet of things (IoT) devices [32], [33].

For the IFA, no universally accepted design equations exist, except in a few highly specific configurations. Nevertheless, a commonly cited rule of thumb states that the total length of the shorting stub should be approximately 20–30% of a quarter wavelength, while the combined length of the shorting stub and the top arm should be close to one quarter of the operating wavelength [33].

2.3.5 Electromagnetic field exposure

Electromagnetic field (EMF) exposure is an important part of device verification. Every wireless device going to market has to be tested for compliance with the EMF regulations. EMF limits, which must be met by all wireless devices available on the market, are set in international guidelines by the International Commission on Nonionizing Radiation Protection (ICNIRP) and the Institute for Electrical and

Electronical Engineers (IEEE) or by national authorities, like the Federal Communications Commission (FCC) and Innovation, Science, and Economic Development Canada (ISED).

2.3.5.1 Specific absorption rate

The ICNIRP and IEEE set exposure limits that have been adopted by the majority of countries, whereas the FCC sets limits for the USA and a few other countries [34]. The EMF limits for frequencies below 6 GHz are defined by the specific absorption rate (SAR), defined as:

$$SAR = \frac{\sigma \mid \boldsymbol{E} \mid^2}{\rho} \tag{2.53}$$

where σ is the electrical conductivity of the tissue in S/m, $\boldsymbol{E}$ is the rms electric field in the tissue in V/m and ρ is the mass density of the tissue in kg/m^3 [35].The local SAR limits are measured for a time averaged period of 6 minutes and either a spatially averaged 1 g or 10 g cubic mass by the FCC and ICNIRP, respectively [35], [36].

The limits for SAR are defined with large safety margins and differ depending on the body part. Limits are lower when measured against the head and torso compared to the extremities. In the case of head and torso, the ICNIRP limits are 2 W/kg over a 10 g mass and the FCC limits are 1.6 W/kg over a 1 g mass. For the limb limits, the ICNIRP and FCC specifies a SAR limit of 4 W/kg over a 10 g mass.[35], [37]. In table 2.1 the relevant limits for each organization are presented.

Table 2.1: RF EMF exposure limits

SAR (W/kg)					
Head and Torso				Limbs	
SAR 1g		SAR 10g		SAR 10g	
ICNIRP	N/A	ICNIRIP	2	ICNIRIP	4.0
FCC	1.6	FCC	N/A	FCC	4.0

The International Electrotechnical Commission (IEC) and IEEE have specified two standardized phantom models for SAR evaluation. Firstly the the so called Specific anthropomorphic mannequin (SAM) is to be used for evaluation of exposure to the head, and for the torso and limbs a flat phantom model is used, both containing two dielectric slabs [38].

3

Methods

This chapter will describe the design process for the antenna elements as well as the simulation setup used for the EMF exposure evaluation and the link budget.

3.1 Literature study on UE antenna design

With increasing integration of satellite connectivity into consumer devices indicates that D2D communication is expected to become a core capability of future 6G architectures. From an original equipment manufacturer (OEM) perspective, this transition carries significant implications: satellite connectivity is progressively viewed less as a premium feature and more as a baseline requirement for future handsets [39]. Accommodating this functionality, however, poses substantial challenges due to the already severe space constraints of modern smartphones. Contemporary handset platforms typically integrate on the order of 20–30 distinct antenna elements, each optimized for specific cellular, short-range, and positioning services, leaving minimal margin for additional hardware [31].

As a result, recent antenna research for NTN has converged on configurations that either reuse existing handset structures, minimize volume, or serve multiple roles without disrupting legacy antenna systems. A unifying observation across the literature is that classical mobile antenna archetypes, most prominently the IFA, PIFA, slot, and loop antennas remain foundational, but are increasingly modified or hybridized to meet NTN-specific radiation and polarization constraints [31]. Rather than introducing fundamentally new antenna classes, published work largely focuses on re-engineering familiar geometries to support upper-hemispherical coverage, circular polarization, or enhanced beam shaping.

One of the most pronounced trends is the migration of radiating structures from the interior of the handset toward the metallic bezel. This shift is motivated both by the scarcity of internal volume and by the bezel's favourable properties as an extended radiating and current-guiding structure [31]. Across multiple studies, the bezel is exploited either as an active radiator or as a parasitic element to improve radiation efficiency and angular coverage. Despite differences in implementation, these designs share a common objective: achieving reliable upper-hemispherical radiation suitable for satellite links while preserving compatibility with dense multi antenna handset layouts [40], [41], [42], [43], [44], [45], [46], [47] and [48]. Importantly, several works

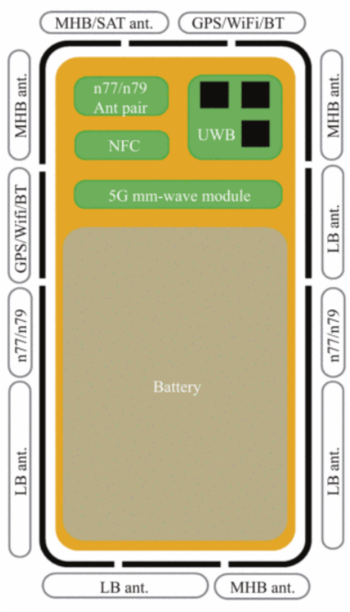

Figure 3.1: Schematic view of a modern handset device with approximate antenna configurations [31].

demonstrate that acceptable hemispherical or end-fire radiation can be obtained without requiring significant protrusions or back-cover real estate, reinforcing the bezel-integrated antenna as a pragmatic solution for NTN inclusion in commercial devices.

A closely related and recurring theme in NTN antenna research is the importance of polarization control, with circular polarization widely adopted to mitigate orientation mismatch between the handset and the satellite. Across both bezel-integrated and compact internal designs, CP is typically realized through multimode excitation, orthogonal current paths, or controlled phase relationships between radiating modes [40], [43] - [47] and [49]. Circular polarization has also been extensively demonstrated within PIFA based and IFA derived handset antennas, where CP performance is achieved either through dual-feed arrangements with a 90° phase offset or through integrated slots and matching networks that combine common and differential modes within a single compact element [50], [51] and [52]. Taken together, these results indicate that polarization robustness can be attained without abandoning well-established handset antenna geometries, reinforcing the feasibility of CP NTN antennas within the constraints of commercial smartphone platforms.

Beyond bezel integration, several studies revisit conventional handset antennas such as IFAs and ILAs, examining their suitability for NTN use when evaluated against different performance metrics. While IFAs are traditionally optimized for terrestrial links, recent work highlights that with appropriate placement, grounding strategies, or nearby parasitic structures, their radiation can be biased toward the upper hemisphere [53]. This suggests that IFAs remain a compelling baseline for NTN exploration, particularly when simplicity, robustness, and integration with existing feed and matching networks are prioritized. In contrast to more specialized CP designs, such antennas emphasize coverage enhancement without radical departure from established handset antenna practices.

A further, but comparatively less explored, aspect in NTN literature is explicit beam control and radiation shaping. While many designs successfully achieve hemispherical coverage, fewer address the directional controllability or orientation sensitivity of the antenna relative to satellite elevation angles. The limited but growing attention to metrics such as upper hemisphere ratio (UHR) indicates an awareness that raw polarization or bandwidth performance alone may be insufficient for robust D2C operation [53] and [54]. This gap suggests room for alternative antenna types that inherently favor controlled broadside or end-fire radiation.

In this context, patch-based antennas, though less common in contemporary smartphones, remain semi relevant in NTN research due to their well defined radiation characteristics and natural compatibility with CP generation. Recent contributions demonstrate that compact or folded patch variants can provide hemispherical CP coverage or high gain end-fire performance when appropriately engineered [55] and [56]. While their integration cost in terms of volume and mechanical constraints is non-trivial, these antennas offer a valuable point of comparison by representing a more classical satellite oriented radiation approach within a handset scale form factor.

3.2 Antenna design

This section presents the design methodology and underlying rationale for the antennas proposed in this thesis. The selected antenna configurations are directly informed by the findings of the preceding literature study and are chosen to collectively span a range of radiation and polarization characteristics. This deliberate selection enables a systematic investigation of how antenna choice influences both the EMF exposure assessment and the associated link budget performance in NTN scenarios.

Three antenna types are considered: a bezel-integrated antenna, an IFA, and a CP patch antenna. The bezel-integrated antenna reflects the dominant design trend identified in recent literature, wherein the metallic bezel is exploited as an active radiating structure, and represents a purpose oriented NTN UE antenna solution. The IFA is included as a compact and well established handset antenna geometry whose radiation characteristics differ from NTN targeted designs, thereby providing a complementary point of comparison in terms of radiation pattern. Finally, the CP patch antenna is included to capture the prominent trend of employing CP to enhance link performance, while also offering well defined radiation characteristics for comparative analysis.

All design and simulation work done on the proposed antennas has been carried out in CST Microwave suite 2025 using the FIT time domain solver.

3.2.1 Bezel antenna

This section describes the rationale and design process for the henceforth named Bezel antenna as well as a parametric study on key design parameters.

3.2.1.1 Antenna concept and configuration

The concept for the Bezel antenna focus on achieving integration of the antenna element into the metallic bezel of modern handset devices as seen in the previous section. The main conceptual design of the antenna comes from [42]. The design goals was to create a simple radiating structure that integrates into the metallic bezel of a modern phone with a widebeam, hemispherical radiation pattern, that closely resembles the prevailing design ideologies for NTN integrated antennas identified in the literature study.

The fundamental idea, from [42] was to use a coupled L shaped branch feed structure to excite the bezel. Antenna 1 shown in figure 3.2 was constructed as rectangular patch coupled to a branch feed with a small ground clearance of 0.5 mm. In figure 3.2a the patch, located at the of the UE is shown in a dark yellow, with the large metallic ground in a shade lighter yellow and the substrate, made of FR-4 set to fully transparent. Figure 3.2b shows the L-shaped feed structure in brown, located at a distance of 0.5 mm from the patch.

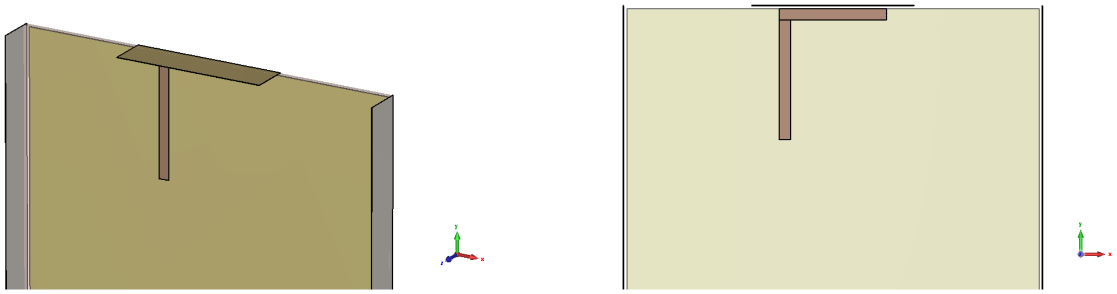
(a) Perspective view of Antenna 1. **(b)** Front view of Antenna 1.

Figure 3.2: Schematic view of Antenna 1.

The reflection coefficient of Antenna 1 can be seen in figure 3.3 with a simulated impedance bandwidth of 215 MHz.

The radiation pattern can be seen in figure 3.4 and it exhibits a endfire radiation pattern with peak realized gain of 4.1 dBi. These characteristics are promising. However, Antenna 1 utilizes only a small part of the top bezel, the Bezel antenna thus seeks to improve upon the utilization of the top bezel by implementing an two element array.

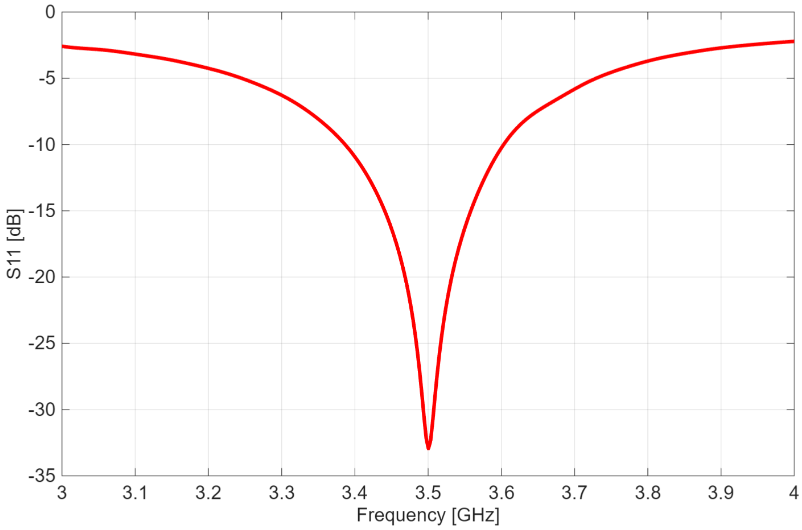

Figure 3.3: Return loss of Antenna 1

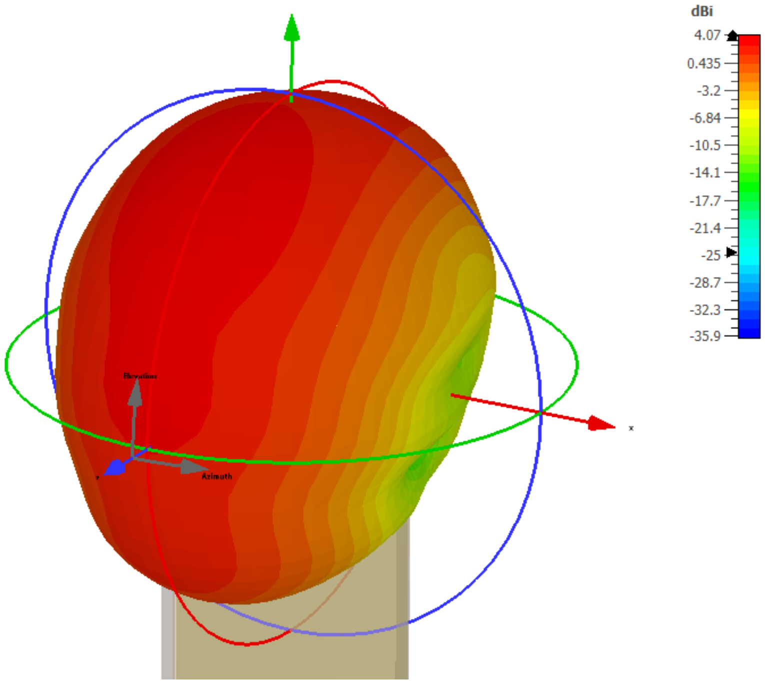

Figure 3.4: Perspective view of the radiation pattern of Antenna 1

The final optimized version of the Bezel antenna is shown in figure 3.5 for both the perspective view and the front view. The antenna is constructed on a FR-4 substrate and modelled out of PEC for all components, including the ground plane, bezel and feeding line. Each of the two antenna elements are placed on either side of the top bezel and extends via a bend onto the sides of the bezel to achieve the correct length for resonance at 3.5 GHz. The elements are separated from the rest of the bezel via a 1 mm slot on either side. Around the antenna elements on the bezel runs a 0.4 mm wide cut out of the ground plane.

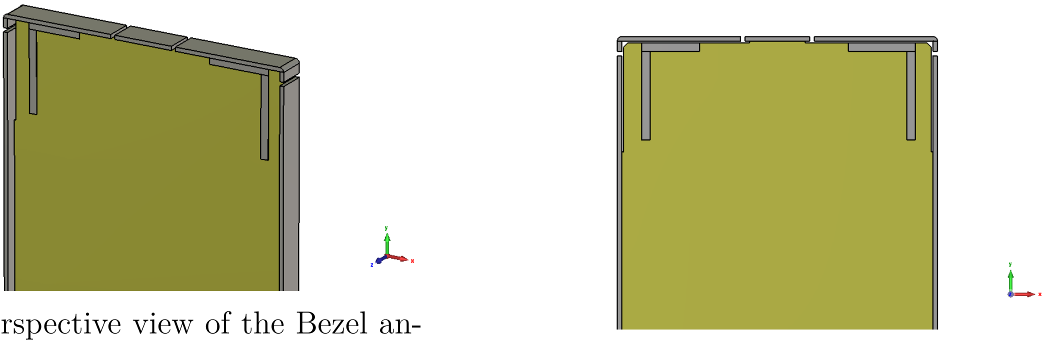

(a) Perspective view of the Bezel antenna.

(b) Front view of the Bezel antenna.

Figure 3.5: Schematic view of the Bezel antenna.

In figure 3.6 the parametrized design is shown, for which W and W_2 denote the width of the patch elements on the top bezel, L_1 and L_2 denote the length of the bend section of each element, W_F and L_F is the length of the horizontal feed and vertical feed respectively. The width of the horizontal feed is denote by k_1 and k_2 and the size of ground plane cut out is denote by d. The final optimized values for each of the parameters are found in table 3.1.

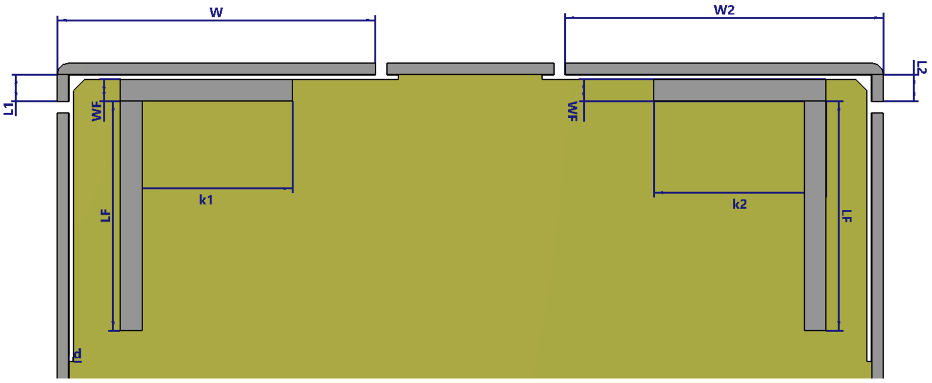

Figure 3.6: Schematic view of the Bezel antenna with complete information on parameters used.

Table 3.1: Optimized parameter for the Bezel antenna, all values presented in mm.

Parameter	Value	Parameter	Value
W	26.725	W_2	26.725
L_1	2.34	L_2	2.34
L_F	20	W_F	1.9
k_1	13	k_2	15
d	0.4		

3.2.1.2 Parametric study

The parametric study was conducted for the impact of the parameters on the single element on the reflection coefficient S_{11}. Figure 3.7 illustrates the influence of the width (W_1) of the top radiating section of the bezel on the antenna performance. This parameter primarily governs the resonant frequency of the antenna, with increasing width shifting the resonance toward lower frequencies due to the increased effective electrical length of the radiating structure. Notably, variations in this width result in large changes to the input impedance in the region around 3.5 GHz, as a result of the matching indicating that the parameter offers rough frequency tuning capability.

In contrast, the length of the side bend (L_1) exhibits a simpler behaviour, as shown in figure 3.8. While changes in the side bend length similarly adjust the resonant frequency, this parameter also has a lessened impact on the impedance matching compared to the width. This shows that the length of the side bend can effectively be used to control the resonant frequency.

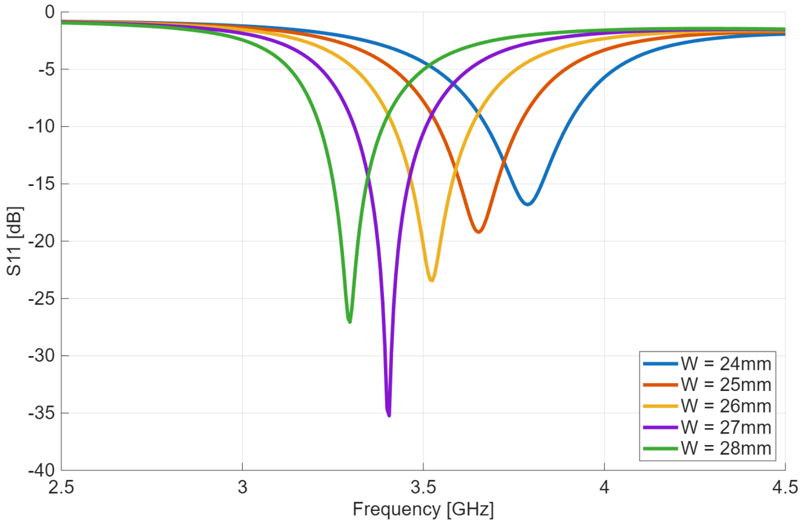

Figure 3.7: Parameter sweep over W for the Bezel antenna, renaming parameter set to values in table 3.1.

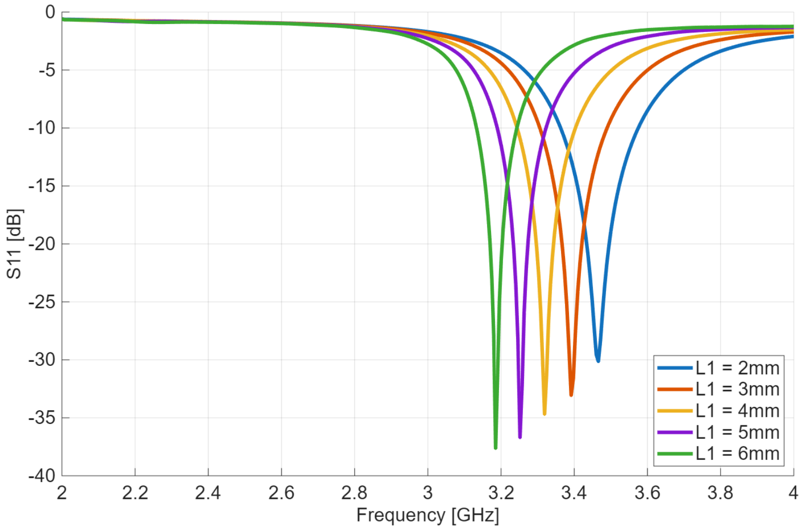

Figure 3.8: Parameter sweep over L_1 for the Bezel antenna, renaming parameter set to values in table 3.1.

The final key parameter is the size of the ground plane cutout, d which is shown in figure 3.9. The figure shows a strong correlation between the impedance matching and the size of d. Notably, the parameter shows little impact on the resonance frequency, which makes it ideal to optimize the efficiency of the antenna.

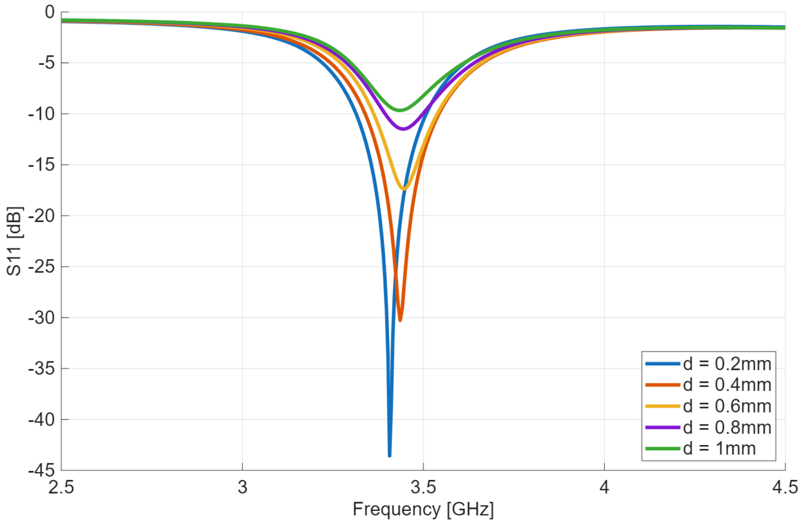

Figure 3.9: Parameter sweep over d for the Bezel antenna, renaming parameter set to values in table 3.1.

To optimize the Bezel antenna for operation in the array configuration, a parametric study was conducted on the active S_{11} for both the length of the first and second feed line. The Bezel antenna has been optimized for a phase feed offset of 180° between the first and second element, which is chosen such that the radiation pattern can be steered more towards either element by applying a lower or higher phase offset.

The effects of the feed-related parameters, namely the feed lengths k_1 and k_2, are presented in figures 3.10 and 3.11, respectively. These parameters have only a minor influence on the resonant frequency but play a dominant role in controlling the impedance matching. Adjusting the feed lengths effectively modifies the input impedance between the feed and the radiating bezel structure, thereby enabling fine impedance tuning without altering the fundamental electrical size of the antenna. Consequently, k_1 and k_2 serve as key matching parameters during the final optimization stage of the antenna design.

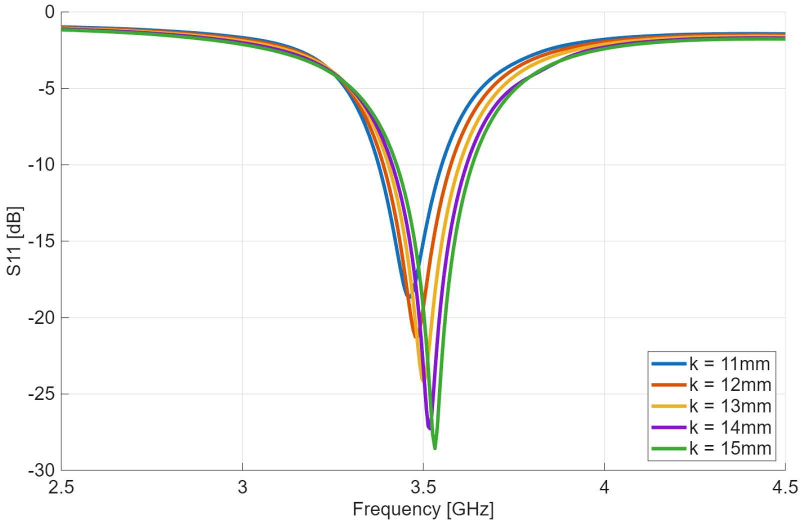

Figure 3.10: Parameter sweep over k for the Bezel antenna, renaming parameter set to values in table 3.1.

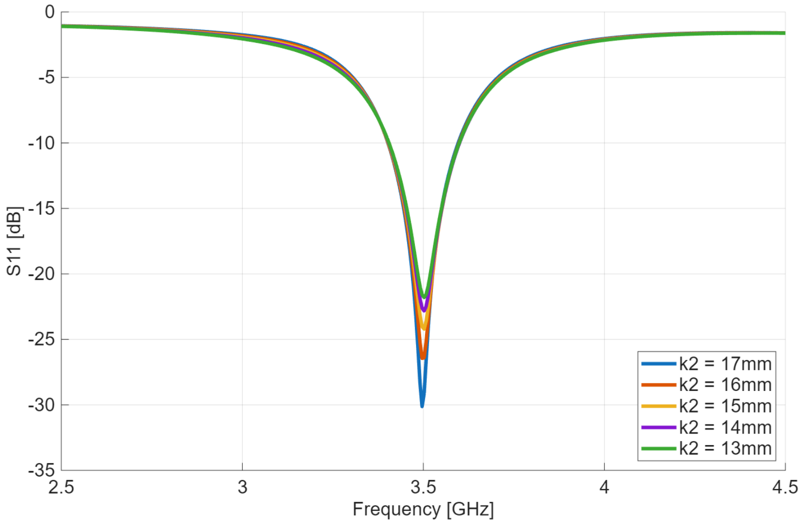

Figure 3.11: Parameter sweep over k_2 for the Bezel antenna, renaming parameter set to values in table 3.1.

3.2.2 Planar inverted F antenna

This section describes the rationale and design process for the inverted F antenna.

3.2.2.1 Antenna concept and configuration

The IFA is a widely adopted design choice in modern UE and is inherently narrowband as bandwidth is proportional to the antenna aperture. However, given the small size of the antenna, ease of integration due to it's planar nature and radiation pattern, it has become a popular choice for UE antennas [57]. In this context, the IFA serves as an appropriate reference design against which the two other proposed antenna concepts may be systematically evaluated with respect to impedance bandwidth, radiation characteristics, and link performance.

The proposed IFA is located at the top edge of the simulated UE ground plane. The antenna geometry and its spatial relationship to the UE chassis are illustrated in figure 3.12. The radiating arm of length L is oriented parallel to the ground plane and elevated by a height h, while the shorting pin establishes a direct electrical connection between the radiating element and the ground plane at one end of the arm. Excitation is provided by a 50 Ω coaxial feed applied at a position intermediate between the shorting pin and the open end of the radiating arm. The distance between the shorting pin and feed location is parametrized by g and the width of the radiating arm, short pin and feeding pin is parametrized by W. Figure 3.13 shows the parametrized IFA

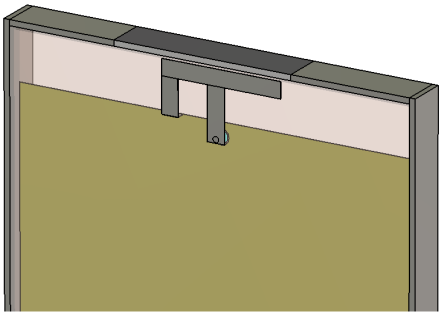

Figure 3.12: Perspective view of the IFA.

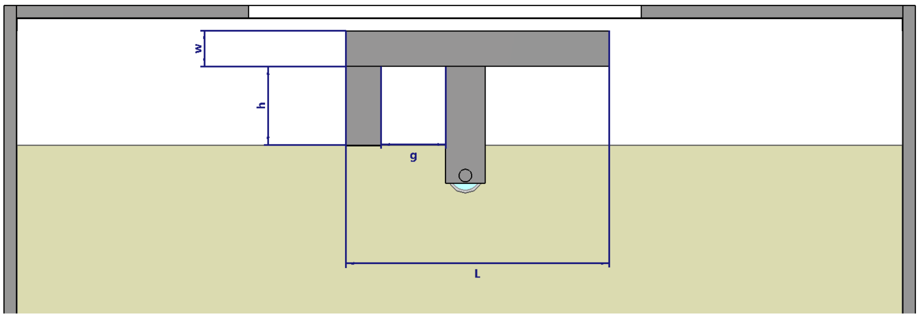

Figure 3.13: Front view of the IFA with parametrized dimensions.

All metallic components, including the radiating arm, shorting pin, feed structure, and UE chassis are modelled as PEC, and are visually differentiated in figure 3.12 to distinguish the antenna structure from the surrounding ground plane. The antenna is mounted on a FR-4 dielectric substrate of thickness t with a ground plane cutout spanning the full width of the UE and size of the IFA as shown in figure 3.13. The UE is then enclosed by a partially metallic bezel with a plastic gap above the radiating arm to facilitate radiation.

The design procedure was initiated through the selection of the radiating arm length, chosen initially to correspond to approximately one quarter wavelength at the target operating frequency of 3.5 GHz. The effective electrical length of the structure is, however, influenced by several secondary geometric factors including the arm height above the ground plane h, the width of the radiating strip, and the proximity of the shorting element. The final optimized values for the parametrized IFA is presented in table 3.2.

Table 3.2: Optimized parameter for the IFA antenna, all values presented in mm

Parameter	Value	Parameter	Value
L	20.8	W	2.81
h	6.22	g	7.89
t	1.6		

3.2.3 Circular polarized patch antenna

This section explains the rationale and design process for the microstrip patch antenna.

3.2.3.1 Antenna concept and configuration

Circular polarization is a desirable property for antennas onboard satellites for much of the aforementioned properties such as mitigation of Faraday rotation and multipath fading. It is therefore of interest to investigate how CP antennas can be implemented on the UE side to mitigate the LP-CP polarization mismatch. Microstrip patch antennas are a natural candidate for CP operation owing to their low profile, ease of fabrication, and compatibility with planar circuit integration. Among the various techniques available to achieve circular polarization from a patch antenna, corner truncation offers a simple solution. By introducing a deliberate geometric truncation to a square patch, two orthogonal degenerate modes are excited with equal amplitude and a 90° phase separation, producing a circularly polarized far field without the complexity of a dual-feed network [28].

Although microstrip patch antennas are not commonly employed in contemporary UEs, they are widely used in satellite communication systems and can be integrated into the device back cover in a manner similar to PIFAs. Owing to their well-defined broadside radiation characteristics and favourable CP performance, microstrip patch antennas also provide a useful reference for comparative evaluation against the two other proposed antenna concepts and for assessing overall link-budget performance.

The designed antenna realizes circular polarization through diagonal corner truncation of a square patch, fed by a single 50 Ω coaxial probe, offset from the centre of the patch and can be see in figure 3.14. This approach was selected for its structural simplicity, as it requires no external phase shifting network or hybrid coupler. The antenna is designed to operate at 3.5 GHz and is implemented on a FR-4 substrate. All metallic surfaces as realized using PEC, shown in figure 3.14 as grey or brass colour to distinguish between UE metallic parts and antenna elements, respectively.

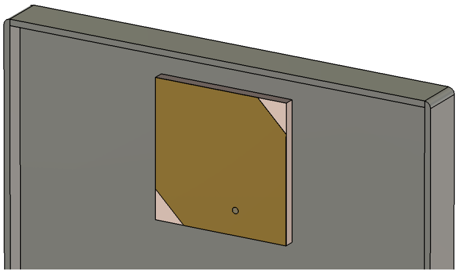

Figure 3.14: Perspective view of the circular polarized microstrip patch antenna.

The initial patch dimensions where derived from equations 2.50 - 2.52 and placed in the middle of the UE ground plane towards the top edge. The truncated version was realized by two orthogonal triangles cut with side length a on the same diagonal.

The key geometric parameters governing antenna performance are the patch width W, the truncation size a, the feed position F_X and F_Y, offset from the patch centre and the substrate of thickness h. The full set of design parameters and their final optimized values are summarized in table 3.3.

Table 3.3: Design parameters and optimized values.

Parameter	Value
W	22.08
a	2.47
F_X	-7.13
F_Y	1.96
h	3

3.3 Electromagnetic field exposure evaluation

This section explains the methodology used to numerically evaluate the EMF exposure of the proposed antenna designs. The evaluation has been carried out in CST studio suit 2025 using the FIT time domain solver with a hexahedral mesh with a density of 15 cells per wavelength, which satisfy the requirements in [58]. The aim of this part of the study is to assess the EMF exposure of each antenna design.

3.3.1 Flat phantom

To evaluate the EMF exposure for the antenna elements towards the torso and limbs a flat phantom is used as specified in [38]. The flat phantom is made up of a 2 mm thick shell with a low relative permittivity in the range $3 \leq \epsilon_r \leq 5$ and loss tangent less than 0.05 and a tissue equivalent liquid with frequency dependent relative permittivity and conductivity. At 3.5 GHz a relative permittivity of 37.9 and conductivity of 2.91 S/m shall be used as specified in [38]. The flat phantom can be seen in figure 3.15, where the 2 mm thick shell in blue can be seen and the tissue equivalent medium with a depth of 75 mm shown in yellow. Finally the density of the tissue equivalent medium was set to 1000 kg/m^3, in accordance with [38].

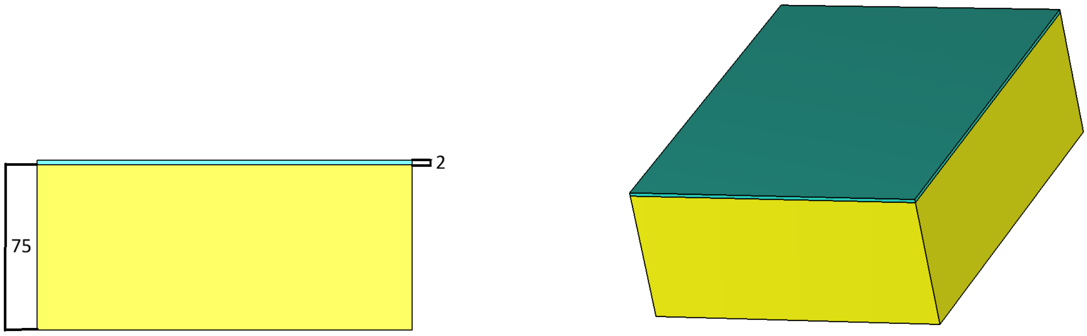

(a) Side view of the flat phantom.

(b) Perspective view of the flat phantom.

Figure 3.15: Flat phantom with the shell in blue and tissue equivalent medium in yellow.

The dimensions of the flat phantom have to be large enough to avoid any back reflections at the boundary and an extra 0.6λ to 1λ of space on either side of the UE model has been tested and verified to be enough. Since the EMF will decay rapidly inside the tissue equivalent medium, the maximum SAR value will be at the surface layer. However the tissue equivalent medium should be thick enough to ensure the absorption of the penetrated field within it. To ensure this, the depth of the tissue equivalent medium was chosen to be seven times the penetration depth of the electric field at 3.5 GHz which showed complete decay of the propagating field, well before the boundary of the phantom.

The EMF assessment was done for two different orientations of the UE in relation to the flat phantom. The first orientation, named herein as the back position orients the UE parallel to the flat phantom with the back side of the UE facing the shell of the flat phantom. This position is used to evaluate the local SAR exposure towards the torso of a user and should be done for a separation distance between the back of the UE and the surface of the flat phantom of 0 mm when testing for the ICNIRP limits. When testing for the FCC limits, the separation can be 5 mm [38]. Thus two positions will be tested, one at 0 mm and one at 5 mm separation. Figure 3.16 shows the back position with the Bezel antenna for a separation distance of 5 mm.

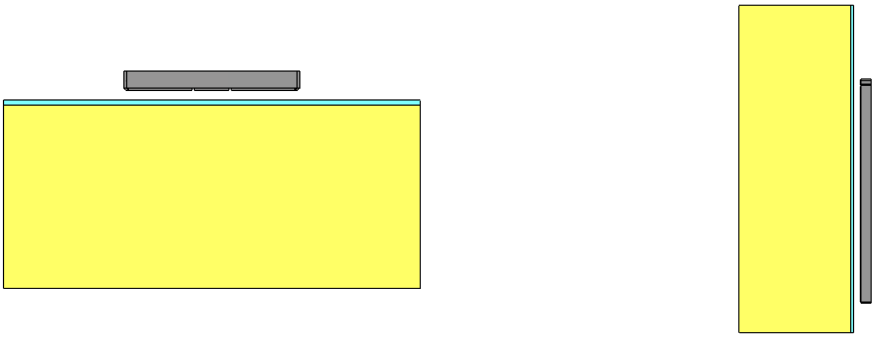

(a) Front view of back position with a separation of 5 mm shown

(b) Side view of back position with a separation of 5 mm shown

Figure 3.16: Views of the back position shown with the Bezel antenna.

The second orientation positions the top part of the UE orthogonal to the flat phantom shell at a separation distance of 0 mm as shown in figure 3.17 with the back of the UE facing the view. This orientation is used to evaluate the local SAR towards a users limbs or extremities, such as hands, arms and legs [38]. This position of the UE in relation to the flat phantom will be, herein referenced as the top position.

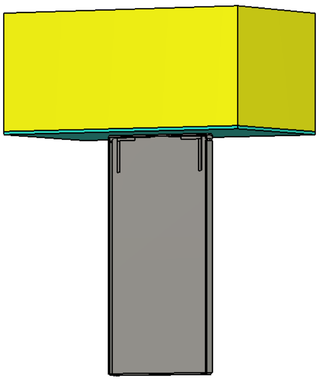

Figure 3.17: Perspective view of the top position shown with the bezel antenna.

For all positions with the flat phantom, the UE was assumed to be 0.5 mm further away from the phantom to account for any plastic covers or dielectric layers not part of the simulated structure.

3.3.2 SAM phantom

To evaluate the local EMF exposure to the head, the SAM phantom model is used, and is shown in figure 3.18 where the shell, shown in blue encompass the entire outer layer of the phantom.

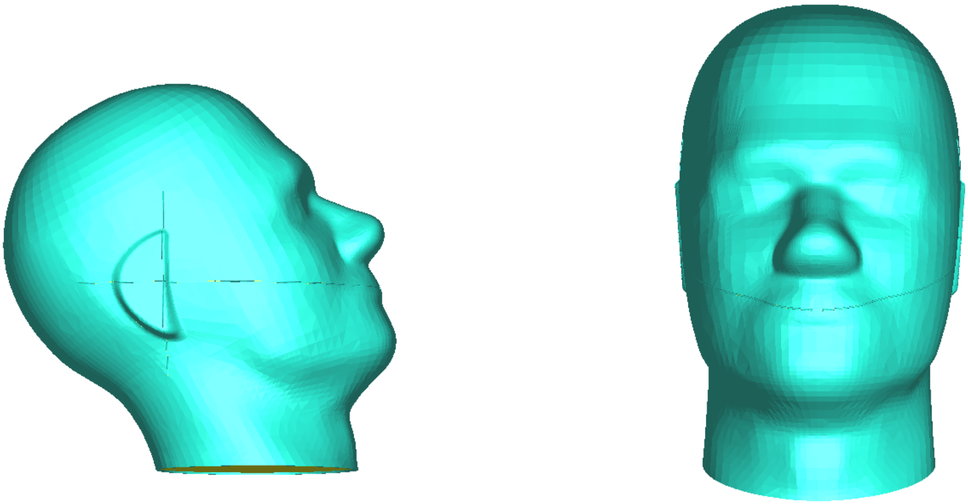

(a) Side view of the SAM phantom model.

(b) Front view of the SAM phantom model.

Figure 3.18: The SAM phantom model.

The evaluation of EMF exposure shall be performed for two positions according to [38], the cheek position and the tilt position referenced herein , shown in figure 3.19 and 3.20, respectively. The difference between the positions is a tilt angle of 15° away from the head in the tilt position [38]. The separation between the SAM phantom and the simulated UE will be set to 0.5 mm to account for any plastic layers that is not part of the simulated UE. The antennas should be evaluated for both the right ear (RE) and left ear (LE) if the antenna is asymmetrical around the centre axis of the UE, otherwise, evaluation to one ear is enough. For the case of the Bezel and CP patch antenna this is true, however due to time constraints only the right ear has been studied for the IFA, thus evaluation with the left ear is left for future work.

Figure 3.19: Schematic view of the cheek position, taken from [38].

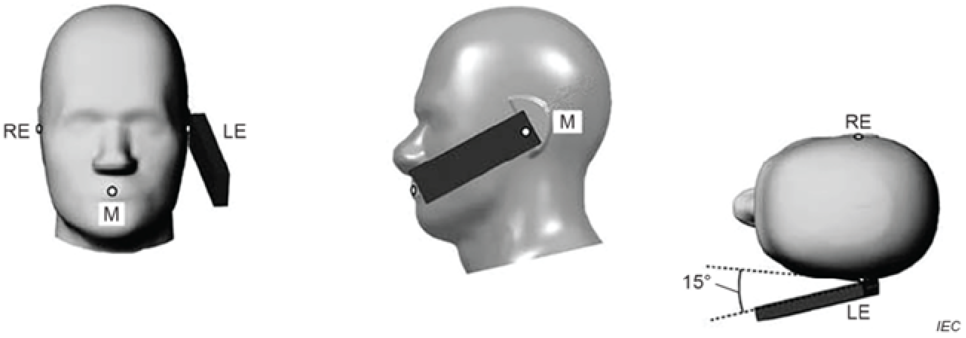

Figure 3.20: Schematic view of the tilt position, taken from [38].

All SAR values in this study are evaluated for an accepted power of 23 dBm as it is assumed that a dynamic tuner is available before the antenna ensuring that its perfectly matched. If stimulated power is required, it can be obtained from the accepted-power SAR via the reflection coefficient, as given by equation 3.1.

$$SAR_{stim} = SAR_{acc}(1 - |S_{11}|^2) \tag{3.1}$$

The SAR results obtained for an accepted power of 23 dBm can be scaled to higher transmit power levels due to the linear dependence of SAR on power. This linear relationship is particularly interesting, as regulatory SAR limits are specified as a six minute time averaged quantity. In practical operation, UE typically only transmits for part of the time and operates with a certain power duty cycle. Therefore, SAR compliance can be evaluated by scaling the peak SAR according to the transmit duty cycle. In the case of 5G time division duplex (TDD) for TN, power duty cycles can be as long as 25 % with shorter duty cycles measured [59].

3.4 Link budget

This section provides the methodology used to evaluate the link budget, beginning with a thorough description of the basis and assumptions for signal attenuators and noise in the link.

3.4.1 Losses

Firstly, the relevant losses needed to be determined and the basis for the assumptions are based on the 3GPP TR 38.821 report which assumes losses due to the atmosphere, scintillation, shadowing margin and polarization mismatch [6].

3.4.1.1 Atmospheric losses

At elevation angles above 10° the only contributions to atmospheric attenuation that needs considering are, absorption from gases, rain and cloud attenuation and, depending on conditions scintillation [60]. ITU-R P.618 outlines a complete method to estimate the attenuation due to precipitation and clouds by two ways, either by measured rainfall rates or by scaling measured attenuation data collected at a set elevation angle and frequency. Here it is chosen to do the former. The following methodology is drawn from [60].

To calculate the attenuation caused by rain, it is first important to note that it is statistically assessed, whereby the attenuation figure acquired is relevant for the specified worst case scenario regarding rain rate, here chosen for a rain rate which is only exceeded for 0.01% of a year in Gothenburg. To begin the slant range L_S from the UE position on the ground to top layer of the rain cloud h_R is defined as

$$L_S = \frac{h_R - h_s}{\sin\theta} \tag{3.2}$$

where θ is the elevation angle and h_s is the height above sea level for the UE. From the slant path length, the horizontal projection is obtained as

$$L_G = L_S \cos\theta \tag{3.3}$$

which is used to calculate the horizontal reduction factor $r_{0.01}$

$$r_{0.01} = \frac{1}{1 + 0.78\sqrt{\frac{L_G \gamma_R}{f}} - 0.38(1 - e^{-2L_G})} \tag{3.4}$$

where f is the frequency and γ_R is the specific attenuation which is empirically determined from the rain rate by two coefficients k and α as

$$\gamma_R = k(R_{0.01})^{\alpha} \tag{3.5}$$

The values for k and α are found in the ITU-R P.838 [61] and the rainfall rate for different regions can be found in ITU-R P.837 [62]. Importantly, the coefficients are polarization dependent as horizontal is attenuated more than vertical polarization due to the oblate shape of a falling raindrop. The 0.01% rain rate for the Gothenburg region is between 30 mm/h and 40 mm/h thus 35 mm/h is chosen.

To calculate the vertical adjustment factor $v_{0.01}$, several variables have to be defined along the way, firstly

$$\zeta = \arctan(\frac{h_R - h_s}{L_G r_{0.01}}) \tag{3.6}$$

for which an intermediate path length can be calculated as

$$L_R = \frac{L_G r_{0.01}}{\cos\theta} \qquad \zeta > 0 \tag{3.7a}$$

$$L_R = \frac{h_R - h_s}{\sin\theta} \qquad else \tag{3.7b}$$

Then for UEs located on a latitude above 36 deg, Gothenburg at 57.7 deg, the vertical adjustment factor can be calculated as

$$v_{0.01} = \frac{1}{1 + \sqrt{\sin\theta}[31(1 - e^{-\theta})\frac{\sqrt{L_G \gamma_R}}{f^2} - 0.45]} \tag{3.8}$$

Lastly the effective path length L_E can be calculated as

$$L_E = L_R v_{0.01} \tag{3.9}$$

From which the total attenuation exceeded for 0.01% of the year is

$$A_{0.01} = \gamma_R L_E \tag{3.10}$$

Scintillation is another atmospheric effect that unlike absorption and rain attenuation does have an impact on lower frequencies and behaves differently in the Ionosphere and Troposphere. Scintillations are fluctuations in the refractive index of the atmosphere which are caused by inhomogeneities in the atmosphere that manifest as rapid amplitude and phase fluctuations of the signal at the receiver. The most common way to characterize the intensity of fluctuations is through the so called scintillation index S_4

$$S_4 = [\frac{\langle I^2 \rangle \langle I \rangle^2}{\langle I \rangle^2}]^{1/2} \tag{3.11}$$

where I is the intensity of the signal [63]. Closely related and directly proportional to the loss incurred by scintillation is the peak-to-peak intensity of the fluctuations P_{fluc} which depends on the intensity distribution. The strength of the scintillation can be classified using the value of S_4 where $S_4 < 0.3$ is classified as weak, $0.3 < S_4 < 0.6$ is moderate and above $S_4 = 0.6$ its classified as strong. In the strong regime, the intensity follows a Rayleigh distribution, in the moderate regime it follows a Nakagami distribution, and in the weak a log normal distribution [63].

Scintillation is heavily location, time and solar dependent, varying strongly over the day with peak values after sunset and over solar cycles. Most importantly is that the equatorial regions, within ±20 latitude and the polar regions are affected the most whereas mid latitudes experience it so rarely that it can be neglected [63].

For Tropospheric propagation, the effects of scintillation can be neglected for frequencies below 6 GHz whereas for Ionospheric propagation the effects should only be considered up to 6 GHz [64]. To evaluate the loss incurred by Ionospheric propagation, one could go via the intensity distributions and treat it statistically or via the so called gigahertz model which allows for frequency scaling of statistical data collected for 4 GHz. The data is presented in figure 3.21 and the scaling is done by the factor $(f/4)^{-1.5}$ where f is the desired frequency. The corresponding loss is

$$L_{sc} = \frac{P_{fluc}}{\sqrt{2}} \tag{3.12}$$

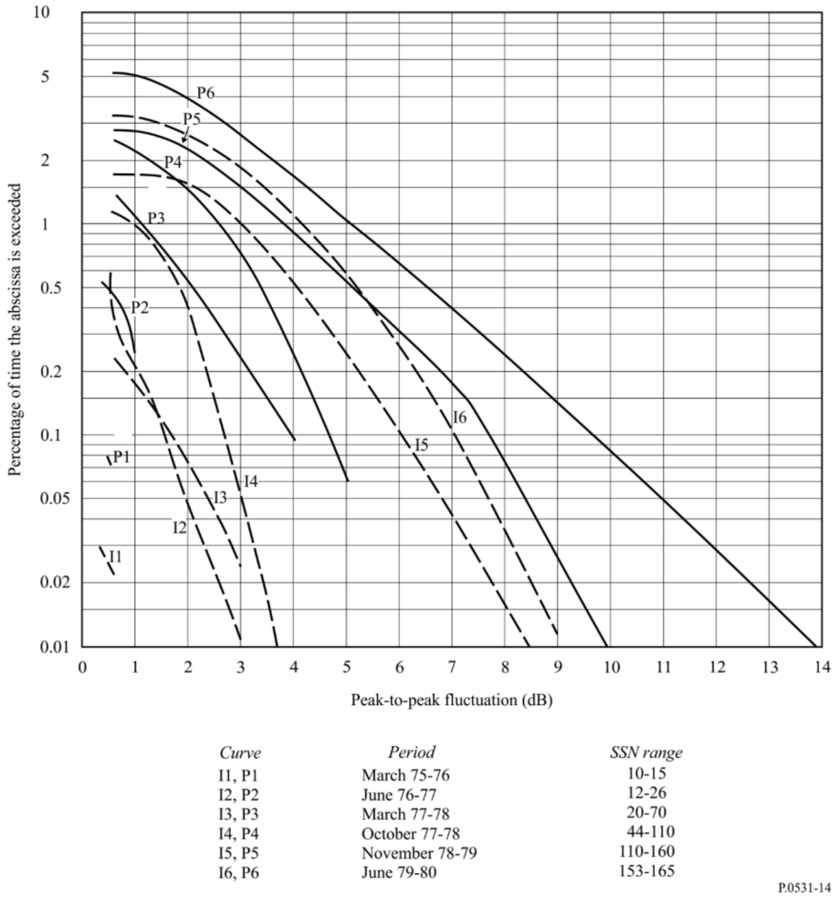

Curve	*Period*	*SSN range*
I1, P1	March 75-76	10-15
I2, P2	June 76-77	12-26
I3, P3	March 77-78	20-70
I4, P4	October 77-78	44-110
I5, P5	November 78-79	110-160
I6, P6	June 79-80	153-165

Figure 3.21: Annual statistics of peak-to-peak fluctuations observed at Hong Kong earth station (Curves I1, P1, I3-I6, P3-P6) and Taipei earth station (Curves P2 and I2) [63].

The loss determined from the gigahertz model is valid for equatorial regions, however for polar regions, with latitude greater than 60°, the following equation may be used to predict the peak-to-peak intensity

$$P_{fluc} = 27.5 \cdot S_4^{1.26} \tag{3.13}$$

under the assumption that $S_4 = 0.7$, i.e. strong regime [63][64].

Tropospheric scintillation can be dealt with using tabulated values that are elevation dependent, however assumed to be frequency invariant above 6 GHz for link model purposes [64].

3.4.1.2 Shadowing margin

As mentioned in previous chapters, the FSPL is dominating contribution to the path loss, however depending on the operational environment of the UE, shadow fading and clutter loss have significant effect. For line of sight (LOS) scenarios the clutter loss, that is the attenuation to the signal caused by nearby objects, can be neglected, however for non line of sight (NLOS) scenarios the clutter loss can exceed 30 dB [64].

Fading in general is the stochastic variation of the signal strength over time due to, either small scale phenomenon which vary with short distances and fast time frames or large scale phenomenon which vary with greater distances and slower time frames, typically over kilometres and seconds to minutes, respectively [65]. Shadow fading is then the time varying attenuation due to large objects that partially or completely block the signal and is modelled as a log-normal distribution. From table 6.6.2-1 through 6.6.2-3 in [64], nominal values for the variance are given for both LOS and NLOS scenarios. A shadow margin of 3 dB is chosen to cover the two sigma or 95-percentile of LOS scenarios which also aligns with the value used by 3GPP in [6].

3.4.1.3 Polarization loss

Losses due to polarization mismatches can be quite severe. An example of this is easily shown when considering equation 2.39 for the case of two orthogonal states of polarization along the x and y-axis, respectively. For an incoming wave, polarized along the x-axis with an antenna polarized along the y-axis, there will be no transmission of power. This mismatch can be quantified by a polarization loss factor (PLF) that relates the polarization of the incoming wave $\hat{\mathbf{P}}_\mathbf{i}$ to the polarization of the receiving antenna $\hat{\mathbf{P}}_\mathbf{r}$ as:

$$PLF = |\hat{\mathbf{P}}_\mathbf{i} \cdot \hat{\mathbf{P}}_\mathbf{r}|^2 \tag{3.14}$$

[66]. The polarization loss can thus be expressed in dB as

$$L_P = -10 * log_{10} PLF \tag{3.15}$$

An important consequence of this is that incident linear polarized wave on a circular polarized antenna, or vice versa only suffers a maximum of 3 dB polarization loss. The axial ratio can be correlated to the polarization loss, using equation 3.16, where R_w is the axial ratio of the incoming wave, R_a is the axial ratio of the receiver antenna and $\Delta\tau$ is the difference in tilt angle [67]. In this thesis the axial ratio of the incoming wave is the same as that of the UE antenna, the axial ratio of the receiving antenna is assumed to be ideal and thus 0 dB and $\Delta\tau$ is set to 0 for a more conservative assumption. Figure 3.22 shows the relation between axial ratio and polarization loss for three different assumptions of receiver antennas.

$$L_P = -10\log_{10}\left(\frac{1}{2} + \frac{4R_wR_a + (R_w^2-1)(R_a^2-1)\cos 2\Delta\tau}{2(R_w^2+1)(R_a^2+1)}\right) \tag{3.16}$$

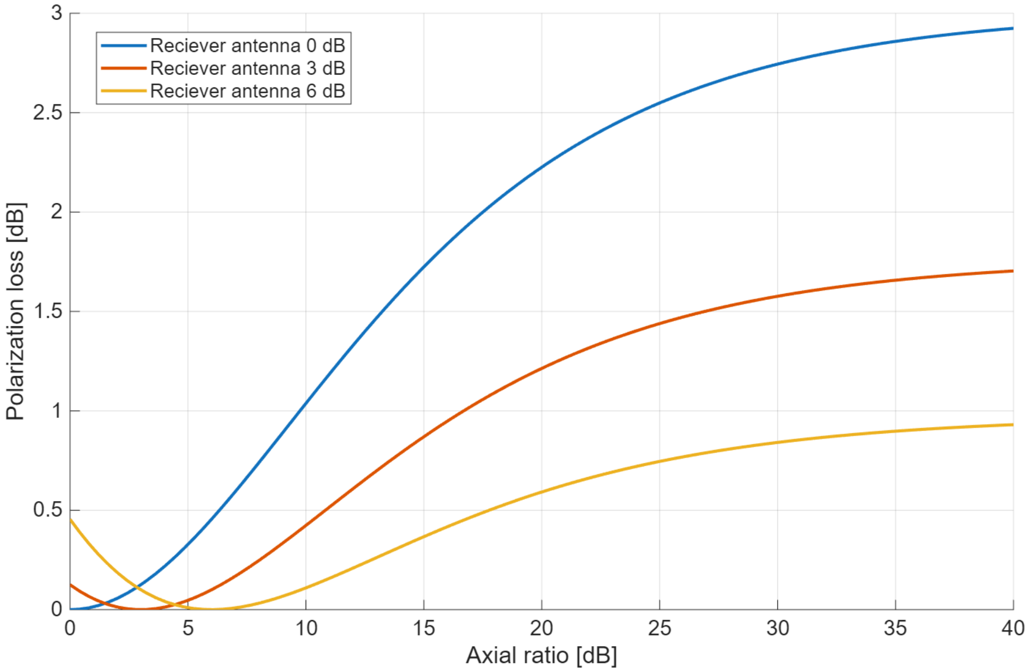

Figure 3.22: Polarization loss compared to the axial ratio for an receiving antenna with AR 0 dB, 3 dB and 6 dB

The aforementioned Faraday rotation will also influence the polarization mismatch. The Faraday rotation that a linearly polarized wave suffers is estimated for any given time as

$$\theta_F = 2.36 \cdot 10^{-14} \frac{BN_T}{f^2} \tag{3.17}$$

where B is the average magnetic field of the Earth, N_T is the TEC and f is the frequency. For a frequency of 3.5 GHz this can equate to several radians depending on the TEC [63]. For a system where both the transmit and receive antenna are linearly polarized, this rotation of the plane of polarization can cause a total mismatch. However if one, or both of the antennas are circularly polarized, this effect can be mitigated completely as the circular polarization is invariant to the rotation.

3.4.2 Noise

Thus far, losses which affect the power of the received signal has been covered, however noise has an equally important effect on the overall quality of the link. The exact G/T figures for commercially available satellite systems are not readily shared, however some data can be found in FCC fillings. One such FCC filling regarding the Starlink GEN 2 NGSO satellite systems outlines G/T figures for an Ku- and Ka-band based service links. The Ku-band antenna reports a minimum gain of 34 dBi and a maximum gain of 44 dBi, with the corresponding worst G/T figures at maximum slant range of 7 dB/K and 17 dB/k, respectively [68]. The Ka-band antennas reports a minimum respectively maximum gain of 34.5 dBi and 44.5 dBi with the corresponding worst slant range G/T figures of 10.5 dB/K and 20.4 dB/K, respectively [68].

Extracting the noise temperatures from these figures yields 501 K and 251 K for the Ku- and Ka-band system, respectively. 3GPP has similarly dimensioned a reference S-band satellite system with a receiving antenna of maximum 30 dBi gain and a corresponding G/T figure of 1.1 dB/K [6] which yields a noise temperature of 776 K. Assuming that each beam of the antenna has max gain and -3 dB contour, the corresponding noise temperature at the edge of the contour would be 389 K. Comparing the noise temperatures of the Starlink system to the 3GPP reference system, it is clear that the 3GPP assumption airs on the conservative side. This comparison is done in order to establish a basis for selection of an appropriate G/T, from which 1.1 dB/K will be used henceforth to better compare against 3GPP.

3.4.3 Scenario

Thus far all parts of the link budget have been covered, however in this section they are all put together to explain the scenario that will be used to evaluate the performance of the antennas.

Firstly, there are two use cases scenarios for the UE, one where the UE is oriented in free space with the top of the UE aligned with the zenith and one where the UE is in proximity to the head in a standard talk position. The talk position defined to be either the SAM Cheek or SAM Tilt position. For both the free space and talk position, a single satellite will be assumed and the link budget evaluated against the angular coverage that the link can sustain a $E_b/N_0 = 9.6$ for 100 kbps using QPSK, aligning with the 3GPP target of 100 kbps experience uplink data rate for satellite access in the 5G network [69]. This angular coverage will be analysed by assuming that the single satellite moves around in the area shown in figure 3.23, which is the upper hemisphere bounded by elevation angles between 30° and 90°.

The loss scenario considered will be representative for most regions on earth. Therefore, scintillation regarding the polar and equatorial regions are omitted as of now and the results from the gigahertz model for mid latitudes gives rise to a negligible amount of scintillation loss, thus 0 dB is assumed, which also aligns with 3GPP assumptions in [6]. The shadowing margin was, as discussed assumed to be 3 dB, the atmospheric losses was calculated to 0.2 dB at 3.5 GHz and finally a 3 dB polarization loss is assumed for the Bezel antenna and IFA. For the CP patch antenna the polarization loss is calculated by using the axial ratio of the antenna. For CNR calculation, the bandwidth of the UL was assumed to be 150 KHz to be able to handle the 100 kbps.

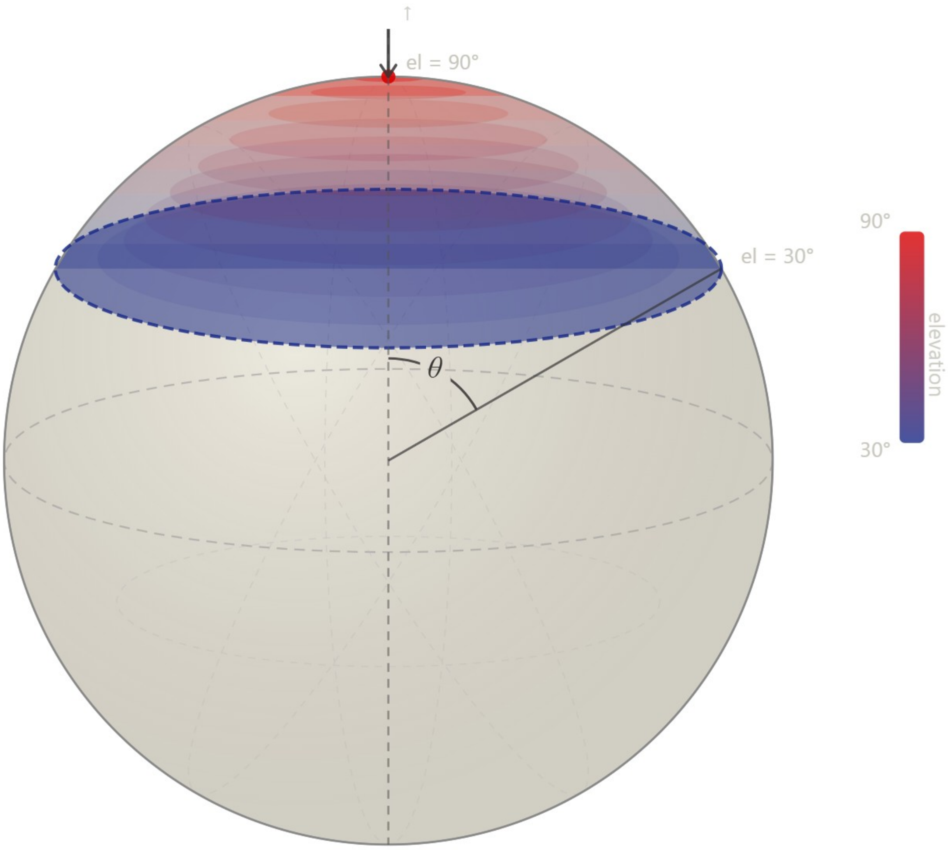

Figure 3.23: Schematic view of the angular range of interest.

4

Results

This chapter will provide the results of thesis in terms of antenna performance, EMF exposure testing and link budget analysis.

4.1 Antenna results

This section will provide the results for each of the designed antennas.

4.1.1 Bezel antenna

The simulated return loss and mutual coupling (isolation) between the antenna elements of the bezel antenna are presented in figure 4.1. At the centre frequency of 3.5 GHz, the antenna exhibits a return loss better than −24 dB and an impedance bandwidth of 197 MHz at the −10 dB level, spanning the frequency range from 3.4 GHz to 3.6 GHz. Furthermore, the isolation between the two elements remains better than −14 dB at 3.5 GHz. These results are obtained for a 180° phase offset between the antenna elements.

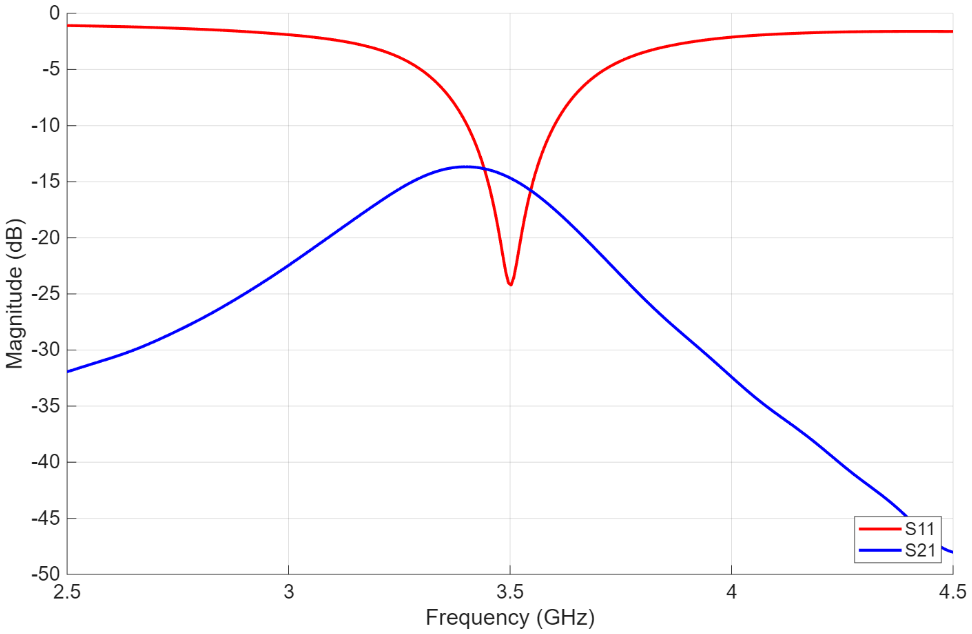

Figure 4.1: S_{11} and S_{21} plot for the Bezel antenna.

The radiation pattern for the Bezel antenna is shown in figure 4.2, where a peak realized gain of 5.28 dBi is shown.

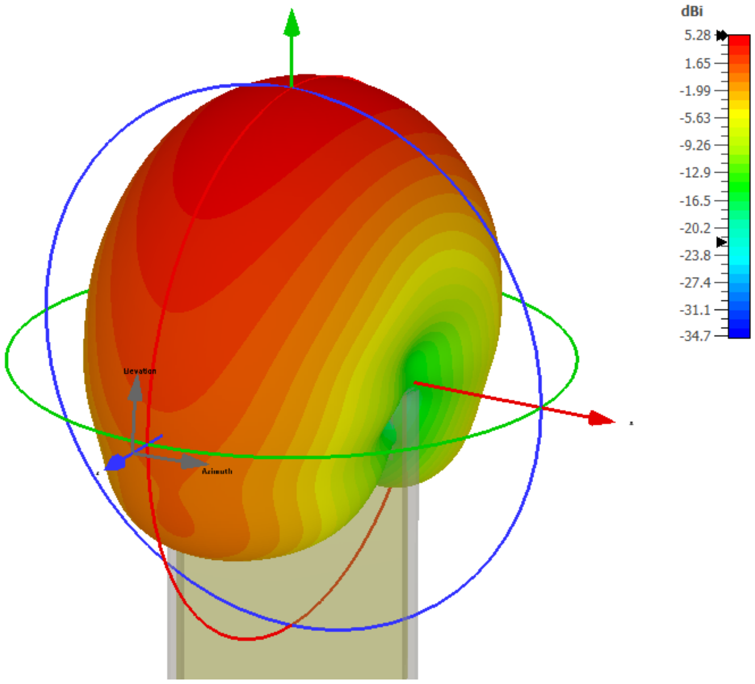

Figure 4.2: Perspective view of the radiation pattern for phase feed offset of 180°.

To further illustrate and for comparison between different phase feed offsets, figures 4.3 - 4.6 shows the radiation pattern for the phase feeding offset values of 0°, 45°, 90° and 135°. The radiation patterns for feeding offsets greater than 180 are mirrored versions of the shown patterns. These results shows that the antenna is able to effectively radiate at lower elevation angles as well as higher elevation angles due to the beam steering.

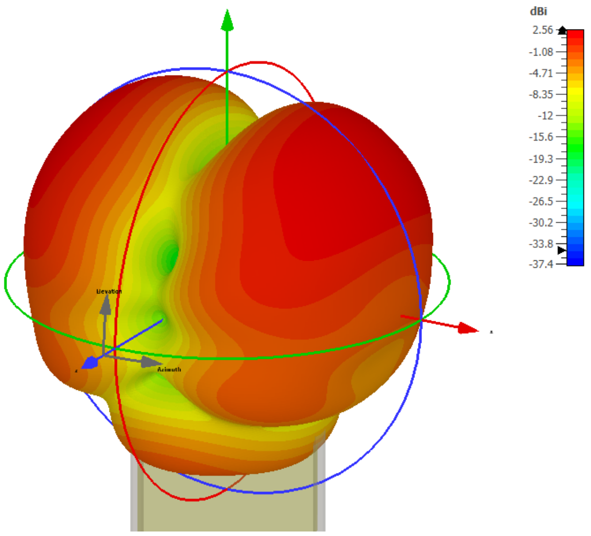

Figure 4.3: Perspective view of the radiation pattern for phase offset 0°.

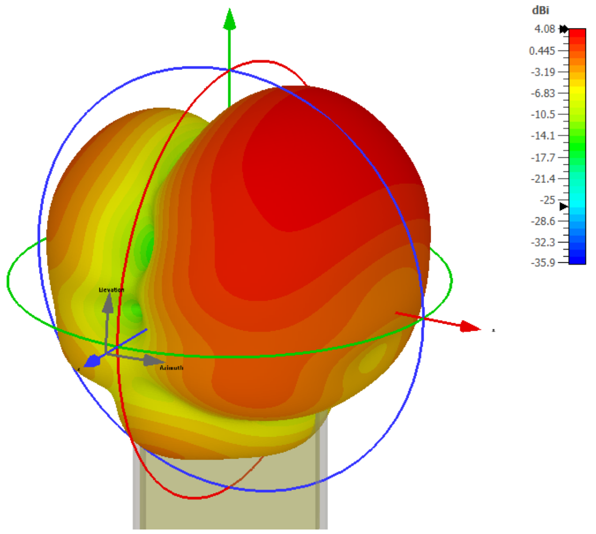

Figure 4.4: Perspective view of the radiation pattern for phase offset 45°.

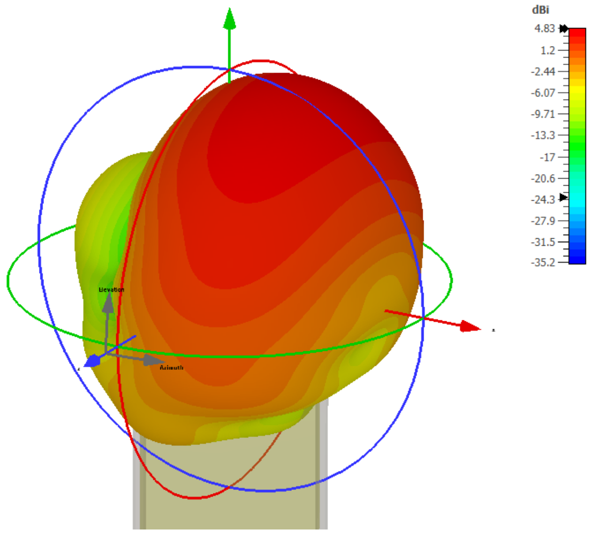

Figure 4.5: Perspective view of the radiation pattern for phase offset 90°.

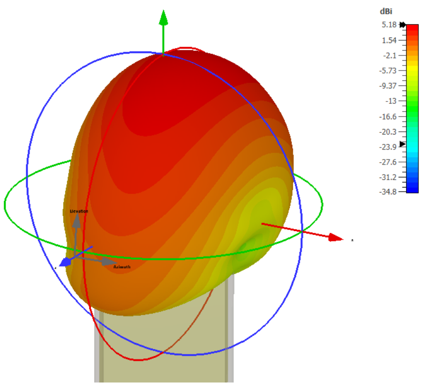

Figure 4.6: Perspective view of the radiation pattern for phase offset 135°.

Finally the influence of the SAM phantom model on the radiation pattern was investigated an the results are shown in figure 4.7. Since the EMF study assumes dynamic tuning capabilities on the antenna, the figures here are presented for IEEE Gain and not realized gain, to remove the impact of the matching. The cheek position shows a peak IEEE Gain of 4.51 dBi whereas the tilt position shows 0.92 dBi at a phase offset of 180°. These results show a severe degradation compared to the free space case in figure 4.2, however, the overall shape of the radiation pattern remains similar.

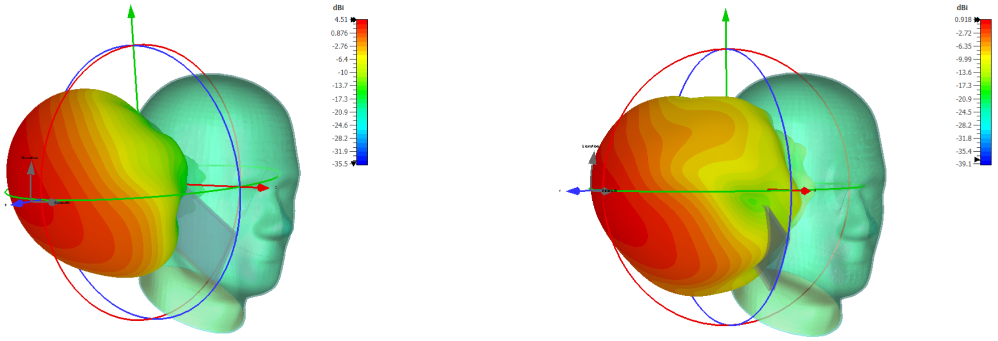

(a) Radiation pattern next to SAM phantom in cheek position

(b) Radiation pattern next to SAM phantom in tilt position.

Figure 4.7: Radiation pattern in proximity to the SAM phantom for the Bezel antenna.

4.1.2 Inverted F antenna

The simulated return loss for the IFA is presented in figure 4.8. The minimum return loss is aligned with the centre frequency of 3.5 GHz and is better than −21 dB with an impedance bandwidth of 410 MHz, spanning the interval 3.32 GHz to 3.73 GHz.

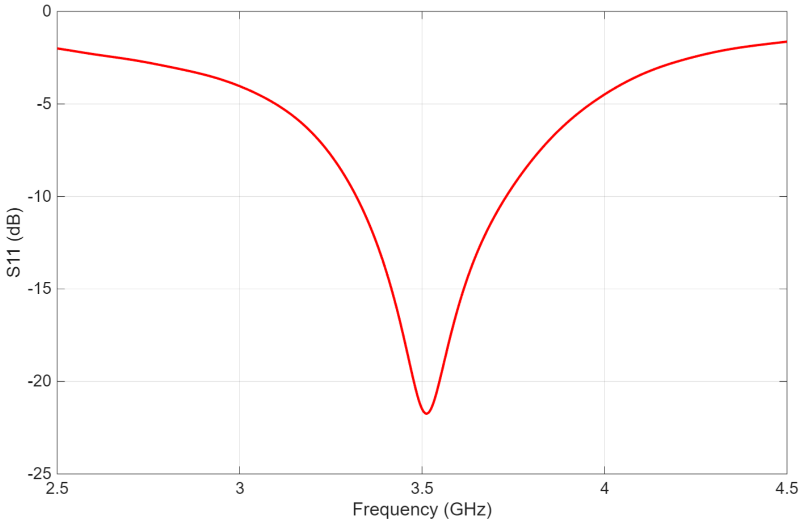

Figure 4.8: S_{11} plot for the Inverted F antenna.

The radiation pattern for the IFA is shown in figure 4.9, where the antenna displays a lower hemispherical radiation pattern with peak realized gain of 6.21 dB. The radiation pattern achieved serve as a complement to the ones achieved by the Bezel antenna, allowing deeper insight from the EMF evaluation and link budget.

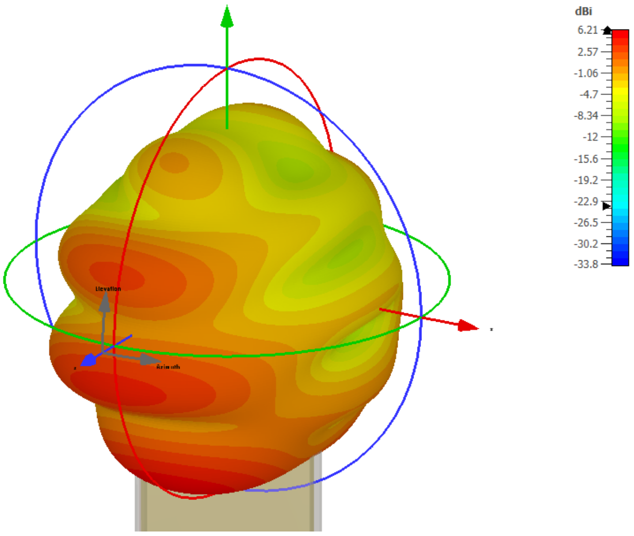

Figure 4.9: Isometric view of the radiation pattern for the inverted F antenna.

Finally the influence of the SAM phantom model on the radiation pattern was investigated an the results are shown in figure 4.10. The cheek position shows a peak Gain of 4.05 dBi whereas the tilt position shows 4.15 dBi. Unlike the Bezel antenna, the IFA shows less degradation to the peak gain and maintains its radiation pattern equally well.

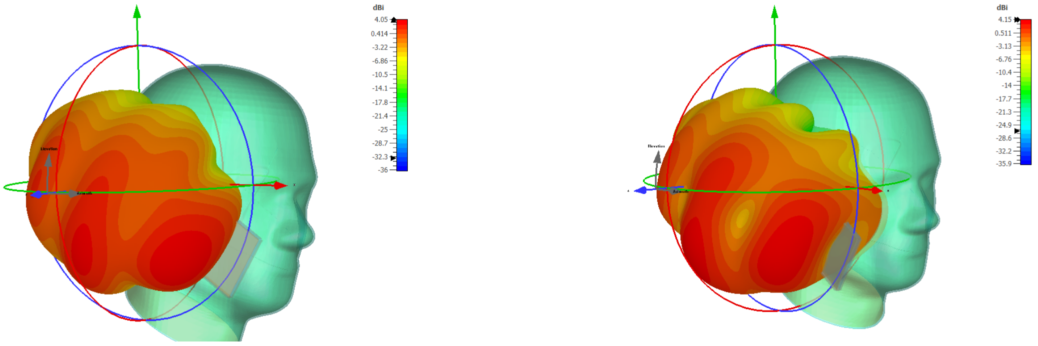

(a) Radiation pattern next to SAM phantom in cheek position

(b) Radiation pattern next to SAM phantom in tilt position.

Figure 4.10: Radiation pattern in proximity to the SAM phantom for the IFA.

4.1.3 Circular polarized patch antenna

The simulated return loss of the CP patch antenna is presented in figure 4.11. The return loss at the centre frequency measures −9.6 dB which is short of the desired

−10 dB. This is likely due to the choice of substrate with a high relative permittivity which incurs large dielectric losses. Benchmarking it against the −6 dB level, the impedance bandwidth measures 250 MHz from 3.35 GHz to 3.6 GHz.

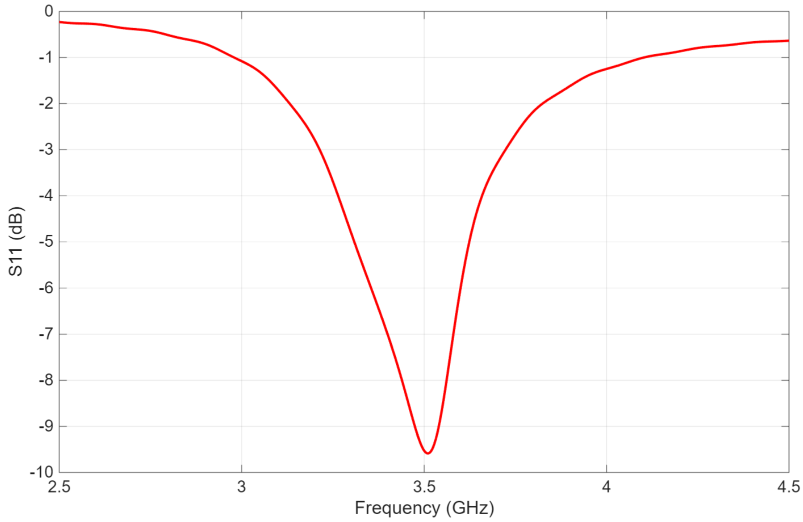

Figure 4.11: S_{11} plot for the CP patch antenna.

The corresponding axial ratio response is shown in figure 4.12, where a minimum axial ratio of 0.75 dB is obtained. The 3 dB axial ratio bandwidth measures 50 MHz, covering from 3.48 GHz to 3.53 GHz.

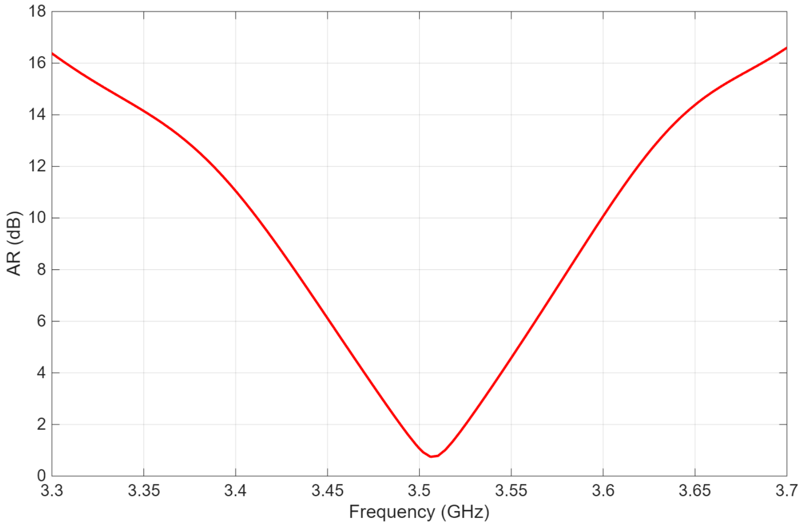

Figure 4.12: Axial ratio as a function of frequency for the CP patch antenna.

The angular dependence of the axial ratio is illustrated in figure 4.13 using a contour plot. The results reveal extended angular regions in which the axial ratio remains below 3 dB, indicating good circular polarization performance. Notably, these regions align with the main lobe direction as azimuth angles between 270° and 90° span the boresight direction. In this range and for positive elevation angles the axial ratio is consistently below or close to 3 dB.

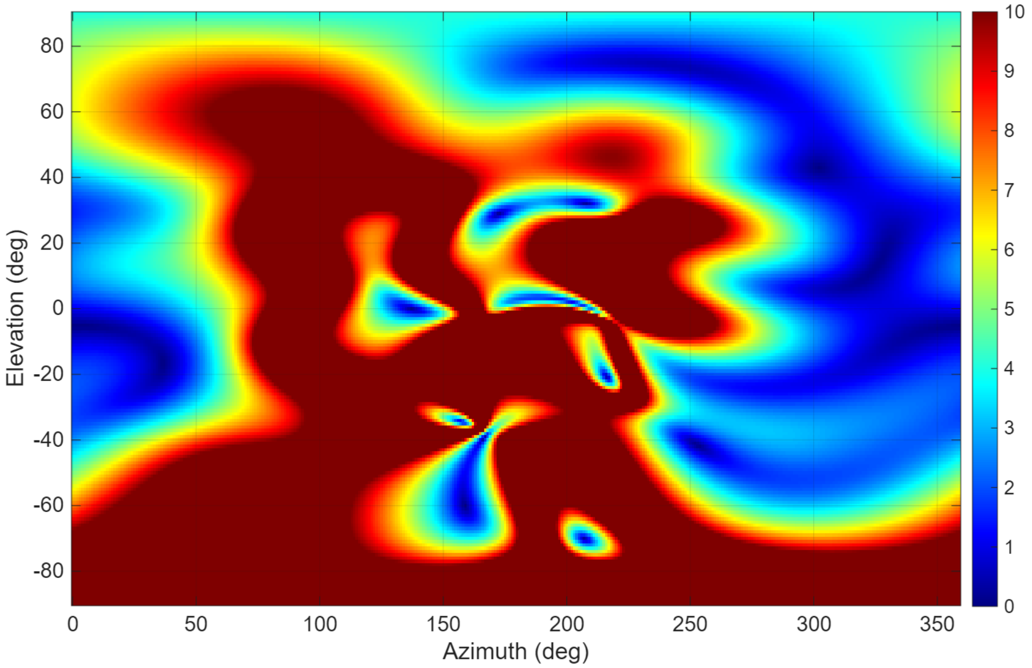

Figure 4.13: Contour plot of the axial ratio over the entire angular range caped to 10 dB.

In figure 4.14, the radiation pattern is shown with a peak realized gain of 3.72 dB.

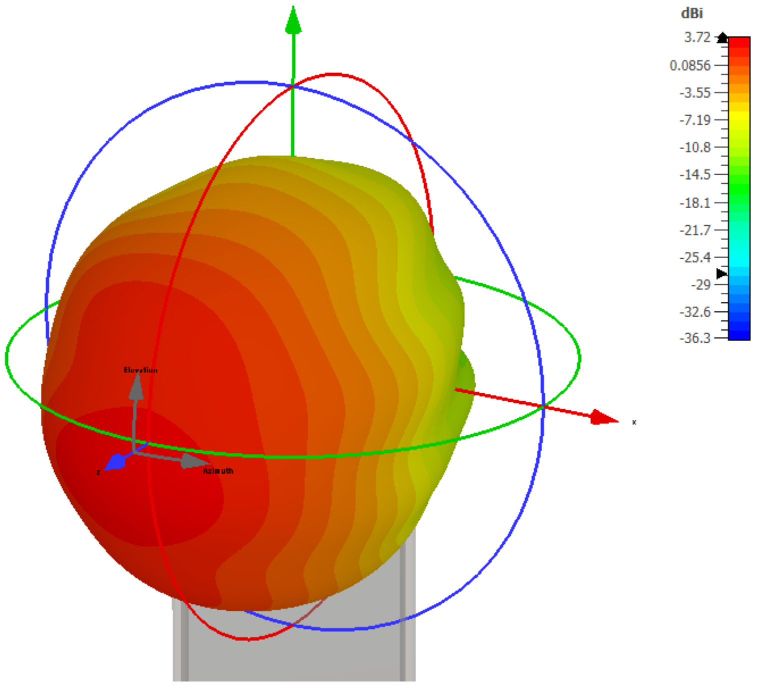

Figure 4.14: Perspective view of the radiation pattern from the CP patch antenna.

Finally the influence of the SAM phantom model on the radiation pattern was investigated an the results are shown in figure 4.7. The cheek position shows a peak

Gain of 4.5 dBi whereas the tilt position shows 3.9 dBi. Notably, the degradation compared to the two other antennas is negligible with a slight shift towards more omnidirectional radiation pattern.

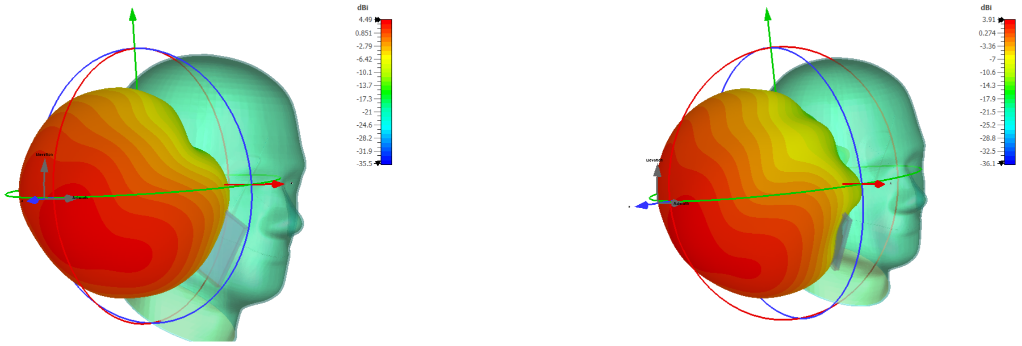

(a) Radiation pattern next to SAM phantom in cheek position

(b) Radiation pattern next to SAM phantom in tilt position.

Figure 4.15: Radiation pattern in proximity to the SAM phantom for the CP patch antenna.

4.2 EMF results

This section will provide the results for the EMF exposure evaluation for each of the studied antennas. The results are presented for each of the five positions and 100% power transmission for the entire averaging time, which is a very conservative assumption. Thus a discussion on the duty cycles needed for compliance and power alteration for 6 minute continuos transmission is provided.

Equally important is the assumptions made on the antenna itself, due to a simplified UE model, there is no account for efficiency loss that would be present in actual implementations. As a result, the total efficiencies of the designed antenna remain very good, reaching −1.1 dB (78%) for the Bezel antenna, −0.4 dB (91%) for the IFA and −3.8 dB (42%) for the CP patch antenna. A study covering major flagship phones on the market from 2024 operating in FR1 shows that the total radiated power (TRP) in free space for 3.5 GHz varies between 18.55 dBm and 9.53 dBm [70]. This means that, the antennas used in this thesis is several dB more efficient than real world examples, thus meaning that the results regarding EMF compliance, are on the conservative side. Consequently, the max power could potentially be increased by several decibels or the duty cycle enlarged, when accounting for higher losses in the UE designs. The use of additional dynamic time averaged power-control techniques may allow further short-term increases in instantaneous power by a few dB under certain user conditions while ensuring that the SAR remains below the applicable limit.

4.2.1 Bezel antenna

In table 4.1, the simulated EMF exposure for the Bezel antenna is shown for feeding of the two antennas 180° out of phase. The results are presented for both 23 dBm and 26 dBm. In table 4.2 the maximum duty cycle (DC) that's needed for compliance to the relevant limit for both power levels is shown. Looking at 23 dBm, the results show that the most restrictive duty cycle needed for compliance to the ICNIRP limits is 47.7% while the corresponding for compliance to the FCC limits is 11.3%, both of which are for operation in the proximity to the head as indicated by the SAM phantom. Comparing the results towards to limbs the torso, the results indicate that the Bezel antenna performs well, with required duty cycles far above the nominal values used in TDD 5G TN. The same goes for operation in proximity to the head, however it is noted that for the tilt position, the peak SAR is almost doubled compared to the cheek position. This behaviour is also consistent with the results obtained for the bezel position and back position, where more of the main beam is directed towards the phantom in the tilt and bezel case compared to the cheek and back case, respectively.

Scaling the results to 26 dBm, also shown in table 4.2 shows that the longest duty cycle for compliance with the ICNIRP limits is 23.85% while the corresponding duty cycle for compliance to the FCC limits is 5.65%. Both values are inside the nominal values used in TDD 5G TN, however, a duty cycle of 5.65% does impose limitations. This result indicates that a higher power class of UEs could be accessible from an EMF perspective, however with the low duty cycle needed for compliance with the FCC limits, it's not without drawbacks.

Table 4.1: SAR results for the Bezel antenna for the five positions, presented for

	23 dBm		26 dBm	
Position	SAR 1g	SAR 10g	SAR 1g	SAR 10g
Top	N/A	6.50	N/A	13.0
Back 0mm	N/A	2.13	N/A	4.26
Back 5mm	5.54	N/A	11.08	N/A
SAM Cheek	7.55	2.42	15.10	4.84
SAM Tilt	14.18	4.19	28.36	8.38

Table 4.2: Duty cycle needed for the compliance to the relevant limit for all five positions, for the Bezel antenna, presented for 23 dBm and 26 dBm.

	23 dBm		26 dBm	
Position	ICNIRP DC	FCC DC	ICNIRP DC	ICNIRP DC
Top	61.5%	61.5%	30.8%	30.8%
Back 0mm	93.9%	N/A	47.0%	N/A
Back 5mm	N/A	28.9%	N/A	14.5%
SAM Cheek	82.6%	21.2%	41.3%	10.6%
SAM Tilt	47.7%	11.3%	23.9%	5.7%

In figure 4.16 the distribution of the local 10 g SAR on the SAM phantom is shown in dB. The plot shows how the SAR is distributed across the phantom and importantly shows that the strength has decayed by around 20 dB towards the edges, which should minimize any back reflections which could artificially inflate peak values. The distributions for all remaining defined positions are found in appendix A

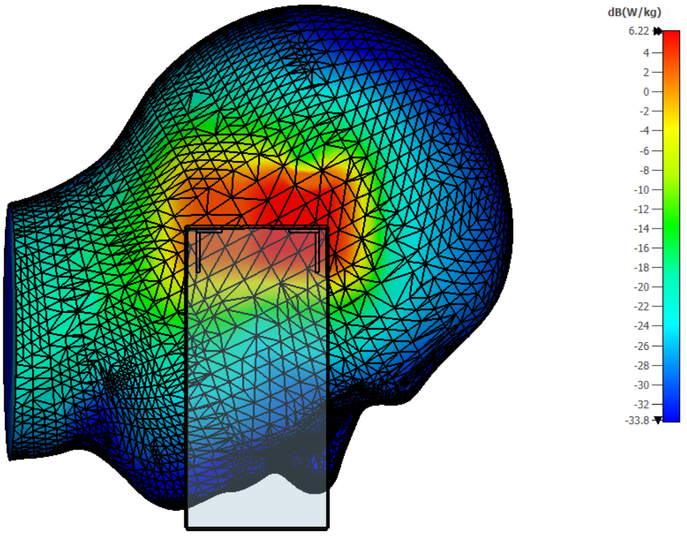

Figure 4.16: Local 10g averaged SAR distribution of the Bezel antenna for the tilt position.

An investigation into how the different phase feeds affected the peak SAR values was conducted for all positions, and the results are presented in table 4.3. The results show considerable differences in peak SAR with differences as large as over 90% in for the bezel position. This large discrepancy is explained by the shift in radiation pattern off the main axis and radiation performance at 3.5 GHz, as seen in the previous section, where specifically for the bezel position this has the greatest effect. The shift in radiation pattern is also the reason for the differences in the other positions as well, where notably, the tilt position suffers a 23.7% degradation in SAR performance between the best performing 180° that directs more of the radiation away from the head and worst performing 90° phase offset that directs more radiation towards the head. This is the second worst degradation after the bezel position, however since the peak SAR values presented in table 4.1 and 4.2 pertain to the 180° phase offset, the conclusions regard the bezel position remains. For the tilt position, it does mean that the potentially largest duty cycle needed is decrees to 38.6% for compliance to the ICNIRP head and torso limits at 23 dBm, or 9.2% for the FCC limits. Since the antenna is intended to work with beam steering, the unweighted averaged duty cycle becomes 42.1% for compliance to the ICNIRP limits and 9.9% for compliance to the FCC limits. Scaled to 26 dBm this means 21.05% and 4.95%, respectively which does pose a degradation to the system, however the main conclusion regarding the potential of a higher power class UE remains.

Table 4.3: Different phase feeding values for the bezel antenna and the peak SAR for each position.

	Tilt		Cheek		Back 0mm	Back 5mm	Bezel
Feeding offset	SAR 1g	SAR 10g	SAR 1g	SAR 10g	SAR 10g	SAR 1g	SAR 10g
45	17.32	4.93	8.16	2.64	1.66	5.5	3.36
90	17.57	5.18	8.76	2.86	1.88	6.2	4.62
135	16.20	4.84	8.46	2.76	2.07	6.19	5.87
180	14.18	4.19	7.55	2.42	2.12	5.52	6.46

4.2.2 Inverted F antenna

In table 4.4 the simulated EMF exposure for the IFA is shown for both 23 dBm and 26 dBm. In table 4.5 the necessary duty cycle needed for compliance to the ICNIRP and FCC limits, respectively are shown. The cases where no duty cycle is needed are marked with 100%. The results for 23 dBm shows that the longest duty cycle achievable for compliance is 30.9% according to the ICNIRP limits and it occurs for the back position at a separation of 0 mm. Similarly, for compliance to the FCC limits, a duty cycle of 32.2% is the longest possible. Scaling the results up to 26 dBm means that the longest possible duty cycles are reduced to 15.5% and 16.1% for compliance to the ICNIRP and FCC limits, respectively.

Table 4.4: SAR results for the IFA for the five positions, presented for

	23 dBm		26 dBm	
Position	SAR 1g	SAR 10g	SAR 1g	SAR 10g
Top	N/A	1.28	N/A	2.56
Back 0mm	N/A	6.47	N/A	12.9
Back 5mm	4.58	N/A	9.16	N/A
SAM Cheek	4.40	2.09	8.80	4.18
SAM Tilt	4.97	2.34	9.94	4.68

Table 4.5: Duty cycle needed for compliance to the relevant limit for all five positions, presented for

	23 dBm		26 dBm	
Position	ICNIRP DC	FCC DC	ICNIRP DC	ICNIRP DC
Top	100%	100%	100%	100%
Back 0mm	30.9%	N/A	15.5%	N/A
Back 5mm	N/A	34.9%	N/A	17.5%
SAM Cheek	95.7%	36.4%	47.9%	18.2%
SAM Tilt	85.5%	32.2%	42.8%	16.1%

The SAR results found in table 4.4 does indicate that for operation close to the head, as indicated by the SAM phantom is less sensitive then operation close to the torso, as indicated by the back position. Comparing this to the Bezel antenna, which is more sensitive in proximity to the head, a direct implication of the difference in radiation pattern is observed. Notable is that the results show full compliance to the limb limits, however, as most of the radiation is directed away from the top, the statement of fully compliant cant be fully argued. To further strengthen the EMF exposure evaluation for the limbs, especially for the IFA which directs most of the radiation downwards, testing for different hand held positions could be included in future work.

The required duty cycles obtained for compliance are comparable to the reference of 25% used in 5G TDD TN, with the results for 23 dBm, achieving longer and the results for 26 dBm, achieving shorter. In [59], comparable duty cycles are achieved for both voice over internet protocol (VoIP) and voice over LTE (VoLTE) in the uplink for 5G TN, giving some credence to the notion that a higher power class of UE is within the realm of possibility.

In figure 4.17, the distribution of the simulated local non-averaged SAR is shown in dB scale for the SAM Tilt position. The figure shows that the strength of the SAR has decayed by more than 20 dB, meaning that artificial inflation of peak values due to reflections at the boundary should be negligible. The remaining distributions for the defined positions are found in the appendix, and show similar characteristics.

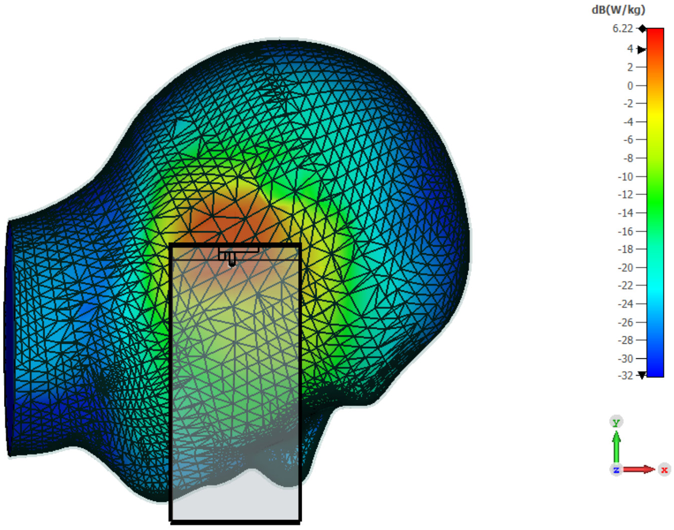

Figure 4.17: Local 10g averaged SAR distribution of the IFA for the SAM Tilt position.

4.2.3 Circular polarized patch antenna

Table 4.6 shows the simulated EMF exposure for the CP patch antenna with peak SAR values given for both 23 dBm and 26 dBm. The duty cycles needed for compliance to both the ICNIRP and FCC limits are given in table 4.7 and fully compliant positions are marked with 100%. The results for 23 dBm show that a duty cycle of 24.9% is needed for compliance with the ICNIRP limits and duty cycle of 16.7% for the FCC limits respectively. Scaling these results to 26 dBm gives duty cycles of

12.5% and 8.4%, respectively. Noteworthy is that for operation in normal talk positions, close to the head, the antenna is fully compliant and power could be increased by orders of magnitude. The problematic positions, from a regulatory standpoint is thus the back positions. Given the broadside radiation pattern with very minimal back lobes, this is to be expected, as the UE itself shields the user from the main lobe when the screen side is facing the user. Regarding the limb limits, the results show full compliance, however as is the case for the IFA, further studies with hand phantoms would strengthen the results regarding limb limits.

Table 4.6: Peak SAR values for the different position for the CP patch antenna presented for 23 dBm and 26 dBm accepted Power

	23 dBm		26 dBm	
Position	SAR 1g	SAR 10g	SAR 1g	SAR 10g
Top	N/A	0.74	N/A	1.48
Back 0mm	N/A	8.03	N/A	16.06
Back 5mm	9.57	N/A	19.14	N/A
SAM Cheek	0.09	0.04	0.18	0.08
SAM Tilt	0.16	0.07	0.36	0.14

Table 4.7: Duty cycle needed for compliance to the relevant limit for all five positions, presented for 23 dBm and 26 dBm.

	23 dBm		26 dBm	
Position	ICNIRP DC	FCC DC	ICNIRP DC	ICNIRP DC
Top	100%	100%	100%	100%
Back 0mm	24.9%	N/A	12.5%	N/A
Back 5mm	N/A	16.7%	N/A	8.4%
SAM Cheek	100%	100%	100%	100%
SAM Tilt	100%	100%	100%	100%

The CP patch antenna thus shows characteristics, that are somewhat different to the two other antennas. The required duty cycle is comparable to the Bezel antenna and thus shares the same takeaways regarding higher power class UE. However it differs in the sense that the Bezel antenna shows fairly uniform SAR values in the different positions compared to the limits, whereas the CP patch antenna only displays elevated SAR values for one orientation. It is another aspect that needs consideration, and a direct consequence of the difference in radiation characteristics.

In figure 4.18, the distribution of the simulated local 10 g averaged SAR is shown in dB scale for the SAM Tilt position. The distributions shows adequate decay in strength to avoid boundary reflections. The remaining distributions for the defined positions are found in the appendix and show similar characteristics.

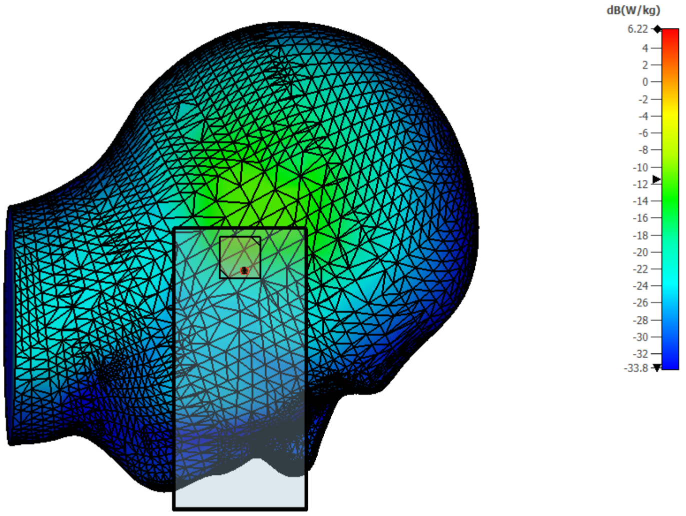

Figure 4.18: Local 10 g averaged SAR distribution of the CP patch antenna for the SAM Tilt position.

4.2.4 Max continuos power results

To put the results into another perspective, here in table 4.8, the maximum continuos 6 minute transmission power is shown for each antenna and position. Noteworthy is the amount of continuos power that can be sent for the talk positions with the CP patch antenna.

Table 4.8: Maximum power able to be transmitted for 100% of the time for all three antennas and positions, results given in dBm.

	Bezel antenna		IFA		CP patch	
Position	INCIRP	FCC	INCIRP	FCC	INCIRP	FCC
top	20.9	20.9	27.9	27.9	30.3	30.3
back 0mm	22.7	N/A	17.9	N/A	17.0	N/A
back 5mm	N/A	17.6	N/A	18.4	N/A	15.2
SAM Cheek	22.2	16.3	22.8	18.6	40.0	35.5
SAM Tilt	19.8	13.5	22.3	18.1	37.6	33

4.3 Link budget results

Figures 4.19 and 4.20 present the cumulative distribution functions of the CNR and E_b/N_0, respectively, evaluated over all azimuth angles and elevation angles above 30° for a UE transmit power of 23 dBm. Results are shown for the Bezel antenna, IFA, CP patch antenna, and an isotropic radiator of 0 dBi used as a reference.

The CNR distributions in figure 4.19 pertain to the free space case described in previous chapters and shows pronounced differences between antenna configurations.

The bezel antenna provides the highest CNR over the majority of angular directions, with its distribution shifted toward higher values. The IFA and CP patch antenna display similar levels of performance in terms of peak CNR. However the IFA shows a smaller angular dependence as indicated by the narrower distribution whereas the CP Patch antenna is more sensitive to the orientation of the UE in relation to the satellite as indicated by the wide distribution. The isotropic radiator results in a narrow, near-vertical distribution, confirming that the observed variations for the other antennas are primarily driven by their radiation characteristics.

A corresponding trend is observed in the E_b/N_0 CDF shown in figure 4.20. Since E_b/N_0 is derived from CNR using a fixed uplink data rate of 100 kpbs the relative ordering of the antennas remains unchanged. The bezel antenna achieves the highest E_b/N_0 across most angular directions, followed by the CP patch antenna and the IFA. The CP patch antenna exhibits a significant fraction of directions with low E_b/N_0, reflecting the impact of its boresight radiation pattern on link-level performance.The results show that for a BER of 10^{-5}, which corresponds to a E_b/N_0 of 9.6 dB the Bezel antenna achieves a data rate of 100 kbps for 55% percent of all angles in bounded upper hemisphere, whereas both the IFA and CP patch antenna never reach it at 23 dBm. Noticeable, the isotropic radiator never reaches this goal either. Further analysis of the results show that the 95th percentile peak data rate achievable at 23 dBm for the Bezel antenna is 224 kbps, 34 kbps for the IFA and 46 kbps for the CP patch antenna. The corresponding 5th percentile data rates for the three antennas are 25 kbps for the Bezel antenna, 6 kbps for the IFA and 2 kbps for the CP patch antenna. Dedicated Satellite phones can maintain calls with as low as 2.4 kbps [71], which means that even at 23 dBm, all three antennas show the possibility to maintain emergency service.

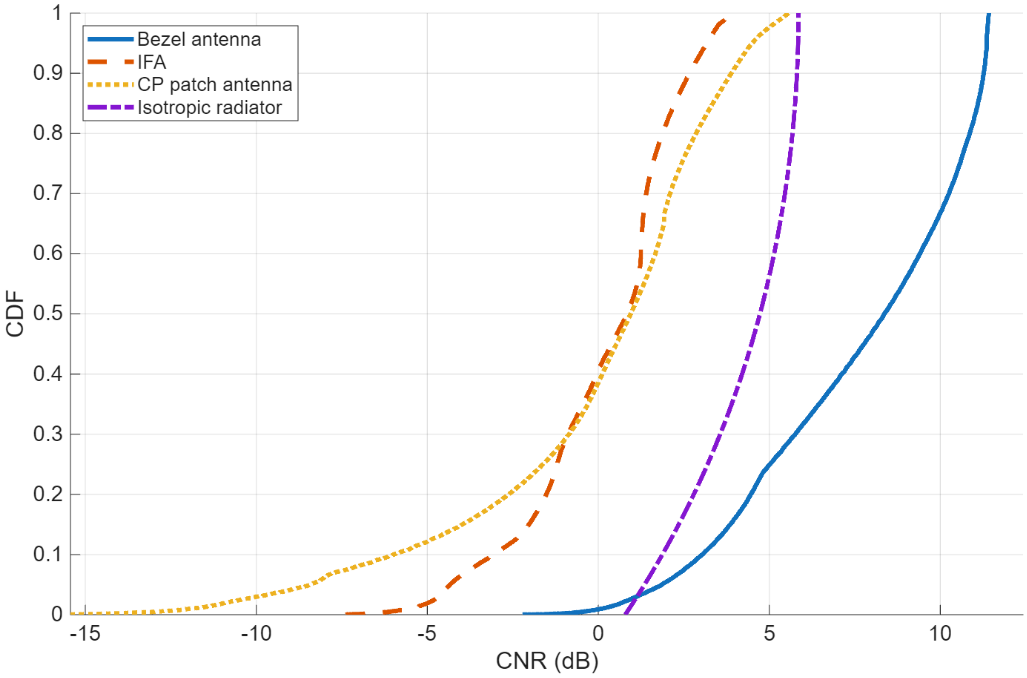

Figure 4.19: CNR results for all antennas and compared to a isotropic radiator for 23 dBm UE transmit power.

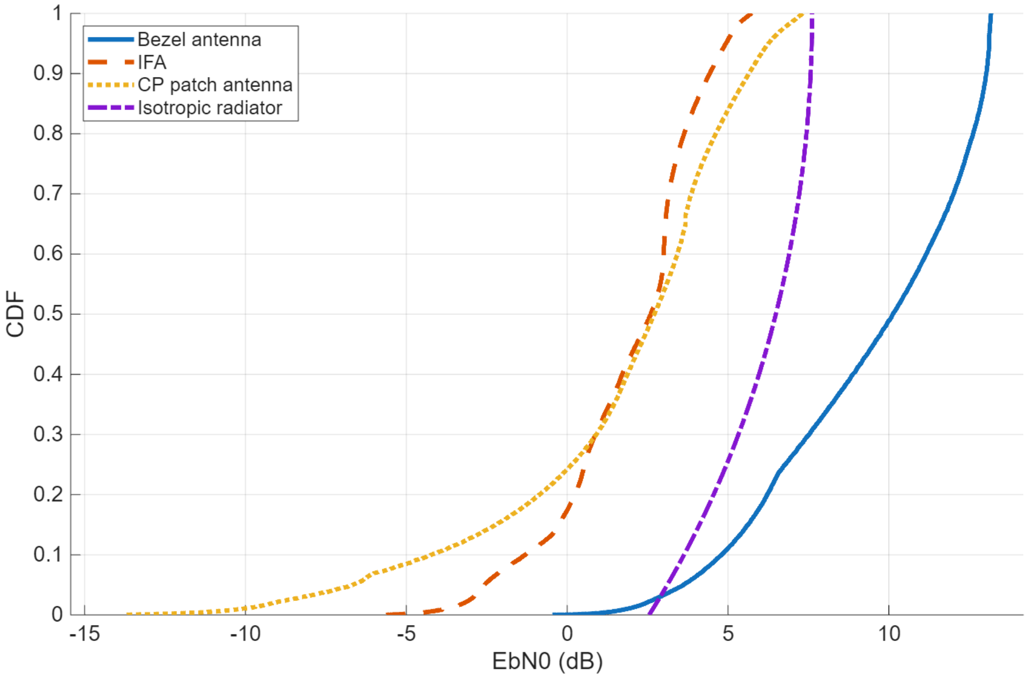

Figure 4.20: E_b/N_0 results for all antennas and compared to a isotropic radiator for 23 dBm UE transmit power.

Figures 4.21 and 4.22 show the corresponding CDFs of CNR and E_b/N_0 for an uplink transmit power increased to 26 dBm. Compared to the 23 dBm case, all antenna configurations experience a uniform rightward shift of approximately 3 dB in both CNR and E_b/N_0, consistent with the increase in transmit power. The angular range for which an E_b/N_0 of 9.6 dB is achieved is increased to 75% for the Bezel antenna, 4% for the CP patch antenna, 50% for the isotropic case and the IFA still does not achieve it. Correspondingly the peak data rates for all three antennas are doubled to 448 kbps, 68 kbps and 92 kbps for the Bezel antenna, IFA and CP patch antenna, respectively. The 5th percentile data rates is equally doubled to 50 kbps, 12 kbps and 4 kbps, respectively.

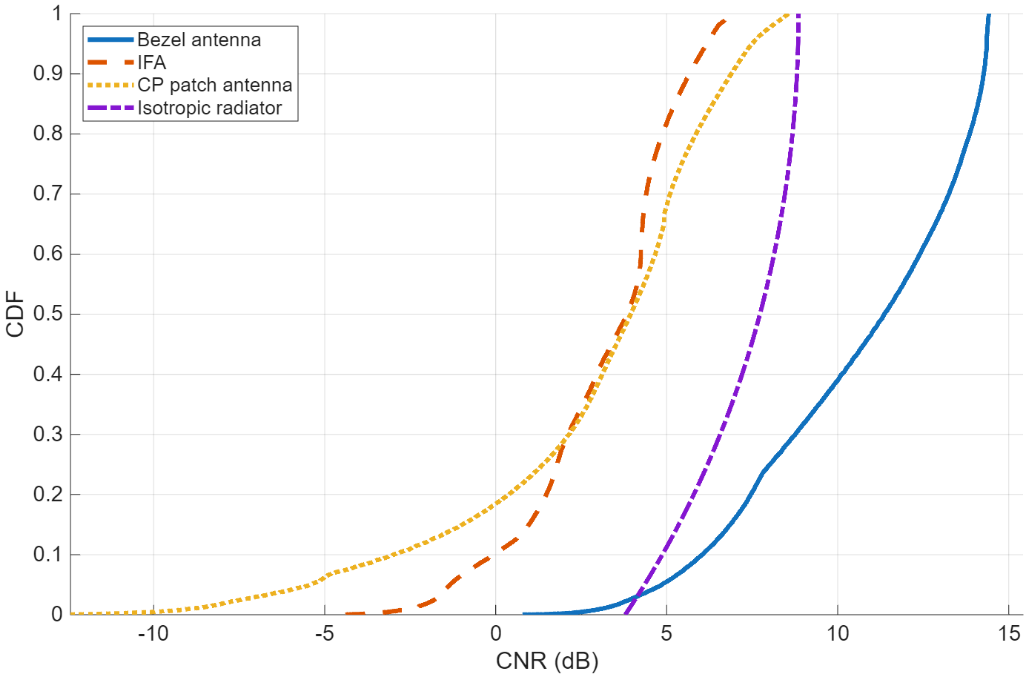

Figure 4.21: CNR results for all antennas and compared to a isotropic radiator for 26 dBm UE transmit power.

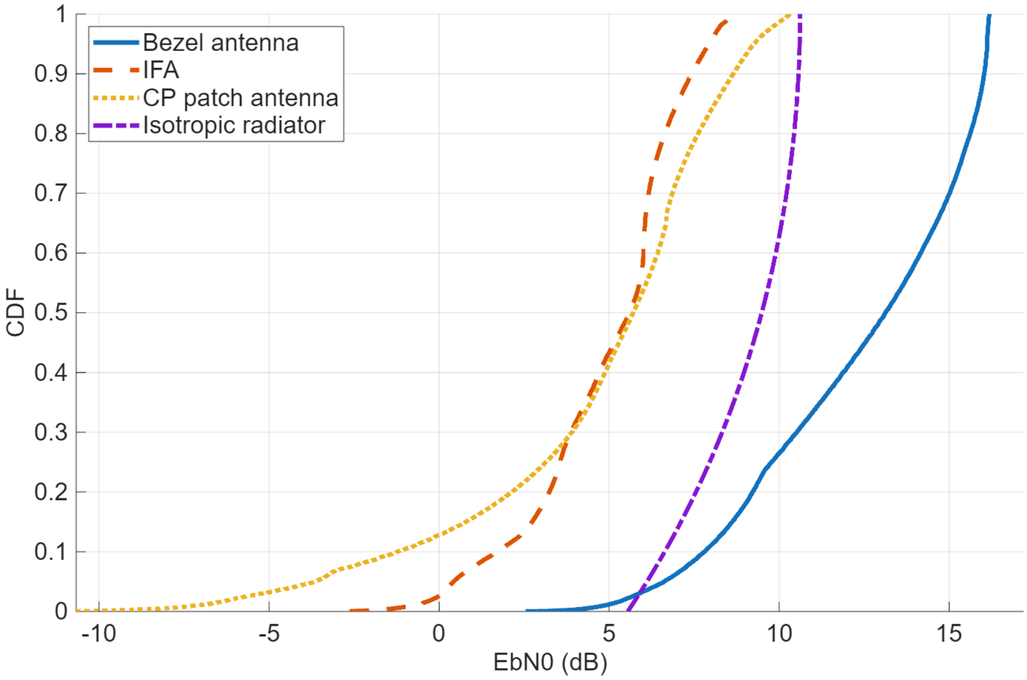

Figure 4.22: E_b/N_0 results for all antennas and compared to a isotropic radiator for 26 dBm UE transmit power.

In Figures 4.23 and 4.24, the influence of the SAM phantom on the link budget is presented for all antennas in the tilt position, as well as for the Bezel antenna in the cheek position. As illustrated in Figures 4.10 and 4.15, no significant positional dependence in the phantom-induced degradation is observed for the IFA and CP patch antennas. However, the Bezel antenna exhibits a notable discrepancy between the two positions. At a transmit power of 23 dBm, none of the evaluated antennas achieve the target throughput of 100 kbps across any proportion of the angular range.

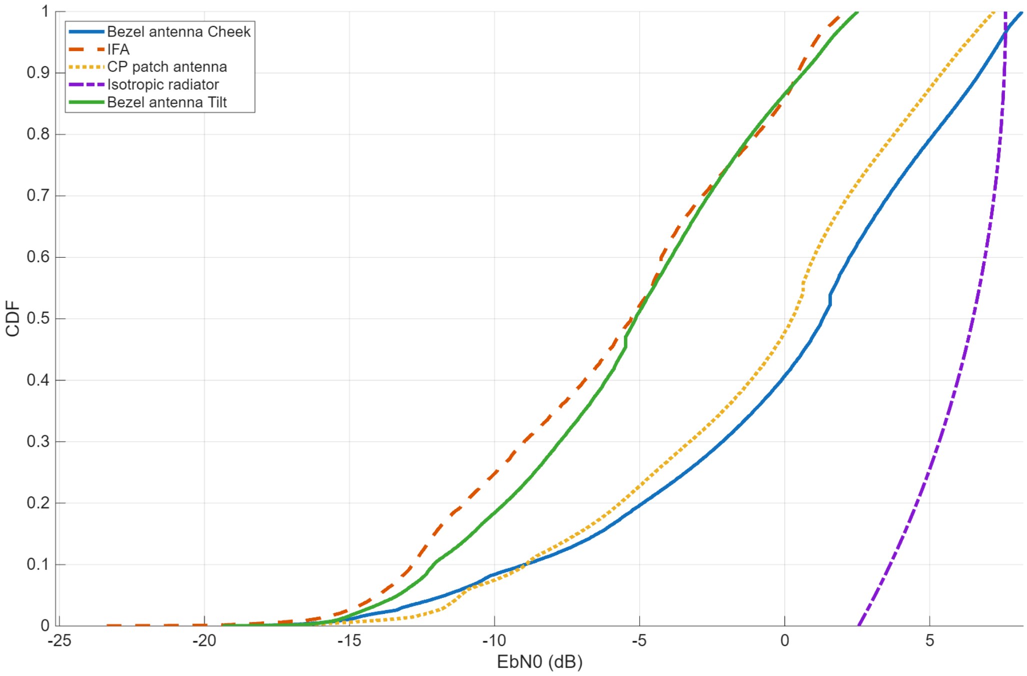

Figure 4.23: $E_b/N0$ for the antennas when in proximity to the SAM phantom for 23 dBm.

At 26 dBm, both the Bezel antenna in the cheek position and the CP patch antenna satisfy the 100 kbps threshold for 10% and 4% of the sampled angles, respectively. Notably, the CP patch antenna exhibits negligible performance degradation in the presence of the phantom, while the IFA experiences marginal degradation. In contrast, the Bezel antenna undergoes substantial attenuation, particularly pronounced in the tilt position, whereas the IFA and CP patch antenna show no statistically discernible difference in performance between the tilt and cheek positions.

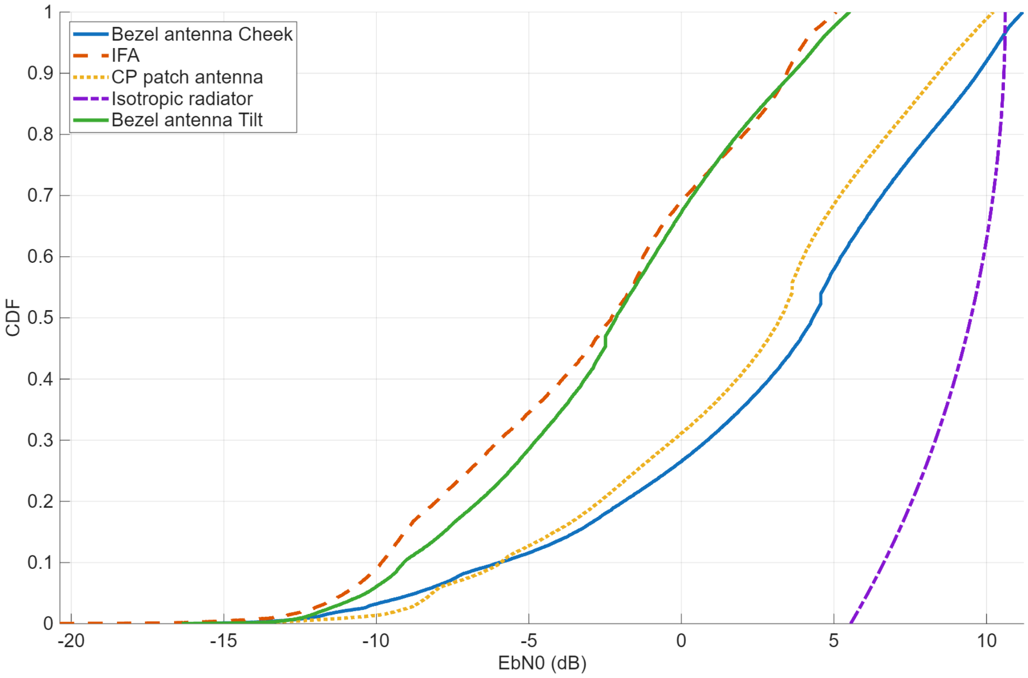

Figure 4.24: $E_b/N0$ for the antennas when in proximity to the SAM phantom tilt position for 26 dBm.

5

Conclusion

This chapter discusses the results and puts them in perspective relative to the methodology used as well as proposing ideas for future work.

5.1 Discussion

This thesis has taken a holistic perspective rarely seen in literature to the evaluation of UE antenna implementations for NTN connectivity. Rather than treating antenna design, EMF exposure compliance, and link budget performance as separate concerns, all three dimensions have been studied in concert for three distinct antenna architectures: a Bezel antenna, an IFA, and a CP patch antenna. This integrated perspective reflects the complex reality that OEM and standards bodies face when designing and regulating UE for NTN scenarios, where the satellite geometry, user behaviour, and regulatory constraints are fundamentally different from those of terrestrial networks.

The three antenna types embody three qualitatively different strategies. The Bezel antenna exhibits a skyward oriented radiation pattern, favouring the upper hemisphere and making it inherently well suited to satellite communication where the satellite is always above the horizon. The IFA, by contrast, redirects most radiated energy downward, away from the satellite. The patch antenna radiates in broadside fashion, concentrating energy in a plane perpendicular to the antenna aperture, which under the assumed free space orientation corresponds to a lateral direction. These three patterns effectively span the principal radiation directions, upward, downward, and lateral, and as a consequence produce markedly different performance profiles across the EMF and link budget metrics. This complementarity of the antenna set is a deliberate strength of the study as it allows general design principles to possibly be inferred rather than conclusions that apply to one particular implementation alone, although some characteristics are antenna specific.

Viewing the three performance dimensions simultaneously reveals a set of inherent trade-offs that no single antenna fully resolves. The Bezel antenna demonstrates the most promising link budget results across the upper hemisphere, with the additional practical advantage of lending itself to integration into the device chassis, a form factor benefit of considerable commercial relevance. However, it also incurs the highest SAR levels in the talk positions, and consequently requires the most restrictive duty cycle limitations of the three designs. It should be noted that the absolute EMF levels reported here are a product of conservative modelling assumptions, nevertheless, the relative relationships between antennas and evaluation positions remain informative and physically meaningful. The IFA and CP patch antenna perform comparably in terms of link budget, though with complementary distributions: the IFA shows an advantage in the lower percentiles of the upper hemisphere, while the CP patch outperforms in the upper percentiles, consistent with their respective radiation patterns. In terms of SAR, both require less restrictive duty cycles than the Bezel antenna in the worst case, though the margin is modest, particularly for the CP patch. Notably, despite the CP patch antenna's significantly inferior link budget performance relative to the Bezel, it offers no compelling advantage in absolute SAR levels, making it a poor compromise between performance and exposure when considered in isolation. Its meaningful advantage lies specifically in the talk positions, where its broadside radiation pattern directs energy away from the head, resulting in substantially lower peak SAR values compared to the other antennas. Across all three antennas, the EMF exposure results are broadly comparable in magnitude, with the IFA showing a marginal advantage overall, however the differ greatly for which usage scenario they incur their peak SAR values, which is an interesting insight and a by-product of their respective radiation patterns.

Closer examination of the link budget results reveals several notable observations. First, the radiation pattern demonstrates a substantial influence on link performance, as anticipated. Notably, the Bezel antenna is the only design to exceed the benchmark established by the isotropic radiator. Second, the results indicate that sustaining the targeted uplink data rate of 100 kbps for 99% of the time demands high antenna performance, both in terms of gain and radiation pattern characteristics, at a transmit power of 23 dBm. This suggests that the system operates under significant power constraints and would benefit considerably from a 3 dB increase in transmit power. The sensitivity to transmit power is particularly well illustrated by the isotropic radiator, which achieves 100 kbps over 0% of the upper hemisphere at 23 dBm, rising to just under 50% at 26 dBm. Third, the results at both the 5th and 95th percentiles warrant further discussion. At the 5th percentile, the achievable bit rates are sufficient to sustain emergency communications, including text messaging, geolocation, and heavily compressed voice calls across all three antenna configurations. This is directly relevant to ongoing discussions regarding the use of existing LTE-capable devices for satellite-based emergency services, as well as the 3GPP-specified purpose-built NTN-capable UE [72]. The limitations of the LTE-enabled approach become apparent when comparing the 95th percentile performance of the IFA and CP patch antenna against that of the Bezel antenna, which represents a more purpose-built design. At 23 dBm, the Bezel antenna achieves a peak data rate exceeding 200 kbps at the 95th percentile, approaching the threshold for the 300 kbps uplink rate identified as necessary for adequate time-to-content in web browsing [73]. The peak achievable data rate at 26 dBm for the 95th percentile even surpasses the 384 kbps rates of the early 3G/UMTS network and is close to the 500 kbps needed for SD-quality video conferencing with Microsoft teams[74]. This highlights that purpose built UE could be used to extend coverage to remote and hard to reach air or maritime corridors and not just as emergency backup [75].

A secondary observation, arising from the broader research context, concerns the implications of operating at higher frequencies relative to the L- and S-band ranges specified by 3GPP for NTN. Two aspects merit attention. First, antenna dimensions are substantially reduced at 3.5 GHz compared to designs targeting frequencies below 2.2 GHz, which is of considerable practical significance given the severe space constraints within modern UE. Second, the FSPL increases by approximately 6 dB at the design frequency relative to the n255 band. Although similar power constraints apply at lower frequencies, a more detailed comparative analysis, taking spectrum availability into account would be valuable in determining the overall suitability of higher frequency bands for NTN uplink applications.

Finally, the implications of circular polarization versus linear polarization merit consideration, particularly given that a substantial portion of the literature surveyed focuses on CP antenna designs. While the potential to recover 3 dB in polarization loss is advantageous in power limited systems, CP generation introduces increased antenna complexity. A common observation from the reviewed works, as well as from the CP patch antenna evaluated here, is that CP generation typically relies on finely tuned mechanisms and exhibits narrow axial ratio bandwidths over limited angular ranges. The link budget results for the Bezel antenna suggest that LP remains a viable option for UE terminals, and that improvements in radiation pattern control or increases in transmit power may offer greater performance gains than the adoption of CP. However, since there are many design that show promising results in terms of CP generation, it would be of great interest to further study such designs using the holistic approach taken here to draw more robust conclusions regarding the polarization choice as there are many advantages to CP. From a spectral efficiency perspective, dual-polarization capability, whether LP or CP, would nonetheless be highly beneficial and also worth further research.

5.2 Conclusions

The thesis has presented a holistic system level approach to UE antenna design for NTN that links together EMF exposure evaluation, with results from an uplink analysis to the specific antenna design. The results show that the choice of UE antenna greatly impacts the link performance and therefore needs consideration when designing the complete NTN communications system. The results also show that any considerations to the power class of the UE can not be decoupled from the fundamental antenna design. Finally the results shows that all three antennas are able to function with emergency text and voice messaging in mind, however also show that greater care to parameter such as radiation pattern and peak realized gain, has to be considered if extended coverage with even 3G uplink speeds are to be realized.

5.3 Future work

Several directions for future work have already been identified throughout the thesis, including the adoption of additional body postures and device orientations in the EMF exposure evaluation to broaden the conclusions, as well as further investigation into optimal frequency bands and polarisation strategies for NTN operation. The following sections outline additional areas where the methodology and findings of this thesis can be extended.

As discussed in the literature review, UE antenna design for NTN applications is subject to severe constraints imposed by the limited available volume within a handset form factor. Much of the existing research consequently focuses on multiband operation, pattern reconfigurability, or miniaturisation as primary design objectives. Future work would benefit from studying antenna architectures that simultaneously satisfy a broader set of requirements, for instance, designs capable of operating across both TN and NTN frequency bands without hardware switching, or antennas that can dynamically adapt their radiation pattern in response to the instantaneous satellite elevation angle. The latter capability is of particular interest. A pattern reconfigurable antenna that steers its main lobe toward the serving satellite could substantially improve link budget performance across the full range of elevation angles, while simultaneously offering the possibility of reducing off-axis radiation toward the user's body, with potential EMF compliance benefits. Investigating such designs within the holistic evaluation framework introduced in this thesis would be a natural and valuable extension.

The link budget analysis presented in this thesis is based on a single satellite scenario, which, while tractable and well defined, represents a conservative and geometrically limited view of NTN system performance. A more complete picture would be obtained by incorporating the downlink direction, which introduces a distinct noise and interference environment at the UE receiver, as well as by modelling multiple interference sources arising from co-channel systems operating in shared frequency bands. Furthermore, extending the analysis to a full satellite constellation, such as the SpaceX Starlink or Eutelsat OneWeb LEO networks would enable a more realistic assessment of coverage continuity, handover frequency, and aggregate link throughput. A multi satellite analysis of this kind would also allow the computation of outage probabilities as a function of antenna type and device orientation, providing a statistically robust characterisation of NTN connectivity that a single satellite model cannot offer. Such results would be of direct utility to standardisation bodies seeking to define minimum performance requirements for NTN-capable UE.

A broader objective for future work is the generalisation of the evaluation methodology developed in this thesis into a reusable and scalable framework, such that any candidate antenna design can be rapidly assessed within a standardised link-level context. This would involve the abstraction of the antenna characterisation, EMF assessment, and link budget computation into a modular pipeline, potentially supported by electromagnetic simulation tools and parameterised channel models. Such a framework would lower the barrier to antenna evaluation for NTN scenarios, enabling device manufacturers and researchers to benchmark new designs against a common set of criteria.

Bibliography

[1] ”5G Explained,” Ericsson. [Online] Available:`https://www.ericsson.com/en/5g`

[2] K. Kim et al.,”NTN Evolution in 3GPP 5G Advanced” 2025 16th International Conference on Information and Communication Technology Convergence (ICTC), Jeju, Korea, Republic of, 2025, pp. 1330-1331, doi: 10.1109/ICTC66702.2025.11388010.

[3] G.Auer, F.Kronestedt, S.Lindqvist, ”Delivering cost efficient 5G high speed internet in rural areas,” Ericsson, [Online], Mar. 31, 2025. Available: `https://www.ericsson.com/en/reports-and-papers/ericsson-technology-review/articles/delivering-cost-efficient-5g-user-experience-in-rural-areas`

[4] J. Krause, ”Non-Terrestrial Networks (NTN),” 3GPP,[Online], May. 14 ,2024. Available: `https://www.3gpp.org/technologies/ntn-overview`

[5] ”Network standardization,” Ericsson, [Online]. Available: `https://www.ericsson.com/en/standardization/network-standards`

[6] 3GPP TR 38.821 16.0.0: ”Solutions for NR to support non-terrestrial networks (NTN) (release 16),” 2019. [Online]. Available: `https://atisorg.s3.amazonaws.com/archive/3gpp-documents/Rel16/ATIS.3GPP.38.821.V1600.pdf`

[7] P. Joshi, D. Colombi, B. Thors, L. -E. Larsson and C. Törnevik, "Output Power Levels of 4G User Equipment and Implications on Realistic RF EMF Exposure Assessments," in IEEE Access, vol. 5, pp. 4545-4550, 2017, doi: 10.1109/ACCESS.2017.2682422.

[8] Pastukh, A.; Tikhvinskiy, V.; Dymkova, S.; Varlamov, O, ”Challenges of Using the L-Band and S-Band for Direct-to-Cellular Satellite 5G-6G NTN Systems,” in Technologies 2023, 11, 110. https://doi.org/10.3390/technologies11040110 `https://www.mdpi.com/2227-7080/11/4/110`

[9] R. Haas. (2025). Orbits and spacecrafts [PowerPoint slides]. Available `https://chalmers.instructure.com/courses/35756/files/4192138?module_item_id=608087`

[10] ESA, 2020, "Types of orbits". Available `https://www.esa.int/Enabling_`

Support/Space_Transportation/Types_of_orbits#GEO

[11] J.E. Draim. "Satellite continuous coverage constellations"m U.S Patent 4 809 935, Mar. 7,1989. Available: https://patentimages.storage.googleapis.com/47/7a/20/5fdfadfb873511/US4809935.pdf

[12] Space Foundation Editorial Team. "Types of Orbtis". Spacefoundation.org. Accessed Jan. 20,2026. [Online.] Available: https://www.spacefoundation.org/space_brief/types-of-orbits/

[13] "Oneweb LEO Constellation". Eutelsat.com. Accessed Jan. 21, 2026. [Online.] Available: https://www.eutelsat.com/satellite-network/oneweb-leo-constellation

[14] Reznik, S V and Reut, D V and Shustilova, M S, Comparison of geostationary and low-orbit “round dance” satellite communication systems, IOP Conference Series: Materials Science and Engineering, vol 971, nr 5, pp. 045-052, Nov. 2020, doi:10.1088/1757-899X/971/5/052045

[15] "Transparent vs. Regenerative Repeater: Key Differences in Satellite Technology", rfwirelessworld.com. Availabe: https://www.rfwireless-world.com/terminology/transparent-vs-regenerative-repeaters

[16] "Computation slant range d between a satellite and ground terminal". space.stackexchange.com. Accessed Feb. 19, 2026. [Online.] Available: https://space.stackexchange.com/questions/64106/computation-slant-range-d-between-a-satellite-and-a-ground-terminal

[17] W.Damm. Signal-to-Noise, Carrier-to-Noise, EbNo [PowerPoint slides]. Available https://noisecom.com/Portals/0/webinars/SN%20CN%20EbNo.pdf#:~:text=C/N%20is%20the%20ratio%20of%20the%20relative,for%20the%20quality%20of%20a%20communication%20channel.

[18] Oi Shan Wong, Mark A. Gregory, Shuo Li, Integration of non-terrestrial network for 5G NR and future 6G: LEO satellite-to-device performance and interference analysis, Computer Networks, Volume 275, 2026, 111870, ISSN 1389-1286, https://doi.org/10.1016/j.comnet.2025.111870.

[19] Wikipedia contributors,Eb/N0, 2025. https://en.wikipedia.org/wiki/Eb/N0. [Online], accessed 19 April 2026.

[20] R. Haas. (2025). Noise on satellite links [PowerPoint slides]. Available https://chalmers.instructure.com/courses/35756/files/4192137?module_item_id=608086

[21] "Antenna Temperature". antennat-thepry.com. Accessed Apr. 21, 2026. [Online.] Available: https://www.antenna-theory.com/basics/temperature.php

[22] DETERMINATION OF THE G/T RATIO FOR EARTH STATIONS OPERATING IN THE FIXED-SATELLITE SERVICE, Rec ITU-R S.733-2, International Telecommunication Union, Geneva, Switzerland, 2000.

[23] R. Haas. (2025). Atmospheric attenuation [PowerPoint slides]. Available `https://chalmers.instructure.com/courses/35756/files/4213962?module_item_id=611510`

[24] Wikipedia commons. "File:Atmospheric electromagnetic transmittance or opacity.jpg — Wikimedia Commons, the free media repository" (2025) Avilable `https://commons.wikimedia.org/wiki/File:Atmospheric_electromagnetic_transmittance_or_opacity.jpg`

[25] ITU, 2005," Specific attenuation model for rain for use in prediction methods". Available `https://www.itu.int/dms_pubrec/itu-r/rec/p/r-rec-p.838-3-200503-i!!pdf-e.pdf`

[26] D. M. Pozar, "Microwave engineering, theory and techniques", 4th ed. Singapore: Wiley, 2012.

[27] P.-S. Kildal, Foundations of Antenna Engineering: A Unified Approach for Line-of-Sight and Multipath. Kildal Antenn AB, 2015.

[28] R. Garg, et al. "Microstrip Antenna Design Handbook". Norwood, MA, USA. Artech House, 2000, pp. 1-5, 266-270. [Online.] Available: `https://uodiyala.edu.iq/uploads/PDF%20ELIBRARY%20UODIYALA/EL37/Microstrip%20Antenna%20Design%20Handbook.pdf`

[29] Alfred-Abam, Fubara Paul, Gyang Olubodun, Fiyinfoluwa. (2023). Full-Wave Numerical Analysis of Dual-Band EPatch Antenna and Reactive Loading Technique to Ascertain the Impedance Driving Point Function. International Journal of Wireless and Microwave Technologies. 13. 26-38. 10.5815/ijwmt.2023.03.03.

[30] "Microstrip (Patch) Antenna", antenna-theory.com Accessed: Feb. 15, 2026. [Online.] Available: `https://antenna-theory.com/antennas/patches/antennaTest.php`

[31] Y. Wang, L. Sun, Z. Du and Z. Zhang, "Antenna Design for Modern Mobile Phones: A Review," in Electromagnetic Science, vol. 2, no. 2, pp. 1-36, June 2024, doi: 10.23919/emsci.2023.0052.

[32] "Inverted-F Antenna (IFA/PIFA) Design: A Complete Guide to 2.4 GHz, Dual-Band, and Mobile Applications". raypcb.com. Accessed Apr. 21, 2026. [Online.] Available: `https://www.raypcb.com/inverted-f-antenna/`

[33] Alan Bensky, Chapter 3 - Antennas and transmission lines, Editor(s): Alan Bensky, Short-range Wireless Communication (Third Edition), Newnes, 2019, Pages 43-83, ISBN 9780128154052, `https://doi.org/10.1016/B978-0-12-815405-2.00003-8`.

[34] "EMF Policy". gsma.com. Accessed Apr. 20, 2026. [Online.] Available: `https://www.gsma.com/solutions-and-impact/connectivity-for-good/public-policy/regulatory-environment/emf-and-health/emf-policy/`

[35] ICNIRP, “Guidelines for Limiting Exposure to Electromagnetic Fields (100 kHz to 300 GHz),” Health Physics, vol. 118, no. 5, pp. 483–524, May 2020, doi:

`https://doi.org/10.1097/hp.0000000000001210`.

[36] Federal Communications Commission, “Radio Frequency Safety,” Federal Communications Commission, Oct. 02, 2017. [Online.] Available: `https://www.fcc.gov/general/radio-frequency-safety-0`.

[37] "47 CFR § 1.1310 - Radiofrequency radiation exposure limits", Cornell Law School, Apr. 1, 2020. [Online.] Available: `https://www.law.cornell.edu/cfr/text/47/1.1310`

[38] "IEC/IEEE International Standard - Measurement procedure for the assessment of specific absorption rate of human exposure to radio frequency fields from hand-held and body-mounted wireless communication devices – Part 1528: Human models, instrumentation, and procedures (Frequency range of 4 MHz to 10 GHz)," in IEC/IEEE 62209-1528:2020 , vol., no., pp.1-284, 19 Oct. 2020, doi: `https://doi.org/10.1109/IEEESTD.2020.9231298`.

[39] I, Gremyr, B.Bergquist, M.Elg, Quality management an introduction. 1st ed.,Lund: Studentlitteratur AB, 2020.

[40] P. Li, Y. Zhang, X. Qin, K. Wei, P. Liang and Y. Li, "Wideband Widebeam Circular-Polarized Antenna Using Asymmetrical Tri-Dipoles for Direct Satellite-to-Handset Communications," in IEEE Transactions on Antennas and Propagation, vol. 72, no. 8, pp. 6270-6277, Aug. 2024, doi: 10.1109/TAP.2024.3420086.

[41] Y. Zhang, K. Wei, P. Liang and Y. Li, "Direct Satellite-to-Handset Terminal Antennas with Hemispherical Coverage based on Three-Magnetic-Current Model," 2025 IEEE International Symposium on Antennas and Propagation and North American Radio Science Meeting (AP-S/CNC-USNC-URSI), Ottawa, ON, Canada, 2025, pp. 2817-2819, doi: 10.1109/AP-S/CNC-USNC-URSI55537.2025.11266053

[42] P. Li, M. Hu, Y. Zhang, P. Liang, K. Wei and Y. Li, "Wide-Beam Metallic Bezel Antenna for Direct Satellite-to-Handset Communications," in IEEE Transactions on Antennas and Propagation, vol. 73, no. 10, pp. 7370-7378, Oct. 2025, doi: 10.1109/TAP.2025.3581705.

[43] H. Tan, C. Deng, Y. Zhang and H. Gao, "An Endfire Circularly Polarized Antenna for GNSS Mobile Phone Application," 2024 IEEE International Workshop on Radio Frequency and Antenna Technologies (iWRFAT), Shenzhen, China, 2024, pp. 77-79, doi: 10.1109/iWRFAT61200.2024.10594632.

[44] H. Zhu, N. Ma, D. Sun, Y. Gao and S. Gao, "A Tri-Band Frequency-Reconfigurable Endfire Circularly Polarized Antenna in Metal-Rimmed Phones for Satellite Communications," in IEEE Transactions on Antennas and Propagation, vol. 74, no. 1, pp. 184-194, Jan. 2026, doi: 10.1109/TAP.2025.3630652.

[45] H. Zhu, D. Zhou, N. Ma and S. Gao, "Endfire Circularly Polarized Antenna for Satellite Communication in Metal-Rimmed Mobile Phones," 2024 14th International Symposium on Antennas, Propagation and EM Theory (ISAPE), Hefei,

China, 2024, pp. 01-04, doi: 10.1109/ISAPE62431.2024.10840913.

[46] M. Y. Liang, X. Y. Li, X. T. Tian, H. B. Zhang and H. H. Zhang, "Satellite Communication Smartphone Circularly Polarized Antenna," 2024 14th International Symposium on Antennas, Propagation and EM Theory (ISAPE), Hefei, China, 2024, pp. 1-2, doi: 10.1109/ISAPE62431.2024.10840822.

[47] S. Rao and Y. Wang, "Shared-Aperture Design of the Cellular Antenna and Satellite Communication Antenna With Circular Polarization in S-Band for Metal-Bezel Smartphones," in IEEE Transactions on Antennas and Propagation, vol. 72, no. 5, pp. 3938-3949, May 2024, doi: 10.1109/TAP.2024.3380371.

[48] S. Rao, Y. Wang, F. Xu, J. Wang and Y. Shi, "Mobile Antenna With a Booster Antenna to Enhance Gain in the Endfire Direction for Satellite Communication in Nona-Band Metal-Bezel Phone," in IEEE Transactions on Antennas and Propagation, vol. 74, no. 1, pp. 1079-1084, Jan. 2026, doi: 10.1109/TAP.2025.3618856.

[49] R. Li, Z. Zhou, H. Fang and Y. Cui, "A Multi-Antenna System for 6G/5G/4G Mobile Terminals," 2024 IEEE 10th International Symposium on Microwave, Antenna, Propagation and EMC Technologies for Wireless Communications (MAPE), Guangzhou, China, 2024, pp. 1-3, doi: 10.1109/MAPE62875.2024.10813737.

[50] T. Jadhav and S. Deshpande, "Miniaturized Planar Inverted-F Antenna with Metallic Cross Branch for Mobile Communication," 2019 International Conference on Intelligent Computing and Control Systems (ICCS), Madurai, India, 2019, pp. 617-620, doi: 10.1109/ICCS45141.2019.9065390.

[51] L. Sun, Y. Li, Z. Zhang and Z. Feng, "Low-Profile Compact Circularly Polarized Slot-Etched PIFA Using Even and Odd Modes," in IEEE Transactions on Antennas and Propagation, vol. 67, no. 6, pp. 4189-4194, June 2019, doi: 10.1109/TAP.2019.2905988.

[52] L. Sun and H. Wang, "Circularly-Polarized Antenna Design in Mobile Phones by the Combination of Common and Differential Modes," 2024 IEEE MTT-S International Wireless Symposium (IWS), Beijing, China, 2024, pp. 1-3, doi: 10.1109/IWS61525.2024.10713522.

[53] M. Wang, L. Chang, Q. Li and A. Zhang, "Modified Inverted-L Antenna With Improved Upper Hemisphere Ratio and Ground-Independent Performance for Augmented Mobile Satellite Service," in IEEE Transactions on Antennas and Propagation, vol. 73, no. 8, pp. 6020-6025, Aug. 2025, doi: 10.1109/TAP.2024.3524719.

[54] W. -Y. Li, W. Chung, A. Miura and H. Tsuji, "Internal Dual-Resonance High-Gain 1.5 Wavelength Loop Antenna for FDD Satellite Phone Applications," 2018 IEEE International Symposium on Antennas and Propagation USNC/URSI National Radio Science Meeting, Boston, MA, USA, 2018, pp. 1775-1776, doi: 10.1109/APUSNCURSINRSM.2018.8608438.

[55] H. Zhang and L. Chang, "Dual-Band Circular-Polarized Ceramic Patch Antenna With Wide-Angle Axial Ratio for Direct Satellite-To-Handset Communications," 2025 IEEE International Workshop on Radio Frequency and Antenna Technologies (iWRFAT), Shenzhen, China, 2025, pp. 239-242, doi: 10.1109/iWRFAT65352.2025.11102877.

[56] Z. Liang, S. Lv, Y. Li, J. Liu and Y. Long, "Compact Folded Slot Antenna and Its Endfire Arrays With High Gain and Vertical Polarization," in IEEE Antennas and Wireless Propagation Letters, vol. 19, no. 5, pp. 786-790, May 2020, doi: 10.1109/LAWP.2020.2980249.

[57] Alnas, J.; Giddings, G.; Jeong, N. Bandwidth Improvement of an Inverted-F Antenna Using Dynamic Hybrid Binary Particle Swarm Optimization. Appl. Sci. 2021, 11, 2559. https://doi.org/10.3390/app11062559

[58] IEC INTERNATIONAL STANDARD Determination of RF field strength, power density and SAR in the vicinity of base stations for the purpose of evaluating human exposure, IEC 62232, Ed. 4, 2025

[59] Vermeeren, G., Verloock, L., Aerts, S., Martens, L., & Joseph, W. (2024). In Situ Assessment of Uplink Duty Cycles for 4G and 5G Wireless Communications. Sensors, 24(10), 3012. https://doi.org/10.3390/s24103012

[60] Propagation data and prediction methods required for the design of Earth-space telecommunication systems, Rec ITU-R P.618-14, International Telecommunication Union, Geneva, Switzerland, Aug. 2023.

[61] Specific attenuation model for rain for use in prediction methods, Rec ITU-R P.838-3, International Telecommunication Union, Geneva, Switzerland, 2005.

[62] Characteristics of precipitation for propagation modelling, Rec ITU-R P.837-8, International Telecommunication Union, Geneva, Switzerland, Sep. 2025.

[63] Ionospheric propagation data and prediction methods required for the design of satellite services and systems, Rec ITU-R P.531-12, International Telecommunication Union, Geneva, Switzerland, Sep. 2013.

[64] "Technical Specification Group Radio Access Network; Study on New Radio (NR) to support non-terrestrial networks (Release 15)", TR 38.811 V15.1.0, 3GPP, Jun 2019. [Online.] Available: `https://hscc.csie.ncu.edu.tw/38811.pdf`

[65] G.Lasser, M.Karlsson. (2024) "Fading systems". [PowerPoint]. Available: `https://chalmers.instructure.com/courses/10471/pages/lectures-pages?module_item_id=95222`

[66] Nikolova. (2025) "Polarization and Related Antenna Parameters". [PDF]. Available: `https://www.ece.mcmaster.ca/faculty/nikolova/antenna_dload/current_lectures/L05_Polar.pdf`

[67] Mathematical model of average and related radiation patterns for point-to-point fixed wireless system antennas for use in interference assessment in the

frequency range from 1 GHz to 86 GHz, Rec ITU-R F, International Telecommunication Union, Geneva, Switzerland, Jan. 2019.

[68] SpaceX Services, Inc., “Application for Modification of Authorization for the SpaceX NGSO Satellite System (Gen2 System), Technical Attachment,” Federal Communications Commission (FCC), IBFS File No. SAT-LOA-20200526-00055, May 26, 2020. [Online.] Available: `https://fcc.report/IBFS/SAT-LOA-20200526-00055/2378671`

[69] "Service requirements for the 5G system" (Release 18), TS 22.261 v18.16.0, 3GPP, Jan, 2025. [Online.] Available: `https://www.etsi.org/deliver/etsi_ts/122200_122299/122261/18.16.00_60/ts_122261v181600p.pdf`

[70] H. Gao, X. Chen, Y. Liu and G. F. Pedersen, "Antenna Performance Over-the-Air Testing of 5G Commercial Smartphones," in IEEE Transactions on Instrumentation and Measurement, vol. 73, pp. 1-8, 2024, Art no. 5502008, doi: 10.1109/TIM.2024.3373106.

[71] "iridium", sigidwiki.com. Accessed May. 11, 2026. [Online.] Available: `https://www.sigidwiki.com/wiki/Iridium`

[72] S.Song et al, "Satellite direct-to-device communication: two approaches for 3GPP global connectivity". Ericsson.com. Accessed May. 7, 2026. [Online.] Available: `https://www.ericsson.com/en/reports-and-papers/ericsson-technology-review/articles/satellite-direct-to-device-communication`

[73] "Uplink speed and slow time-to-content", Ericsson.com. Accessed May. 7, 2026. [Online.] Available: `https://www.ericsson.com/en/reports-and-papers/mobility-report/articles/uplink-speed-and-slow-time-to-content`

[74] "Microsoft teams bandwidth requirement", Microsoft.com. Accessed May. 8, 2026. [Online.] Available: `https://learn.microsoft.com/en-us/answers/questions/4384253/microsoft-teams-bandwidth-requirement`

[75] UMTS Forum, "3G/UMTS Towards mobile broeadband and personal internet", 3GPPP.com. Accessed May. 7 , 2026. [Online.] Available: `https://www.3gpp.org/ftp/pcg/pcg_15/docs/pdf/PCG15_22.pdf`

A

Appendix 1

Found here in the appendix are the remaining SAR distributions for all phantom models which are included to support the validity of the numerical evaluation. These supplementary results document the spatial variation of energy absorption across different simulation conditions and enable a more detailed examination of localized absorption characteristics, but also show that the phantom models used are adequately sized to avoid reflections from the boundary.

In figure A.1 through A.3 the distribution of the local 10 g SAR is shown for the SAM phantom using the cheek position for all three antennas. The results show that the SAM phantom adequately decays the EM wave inside the tissue.

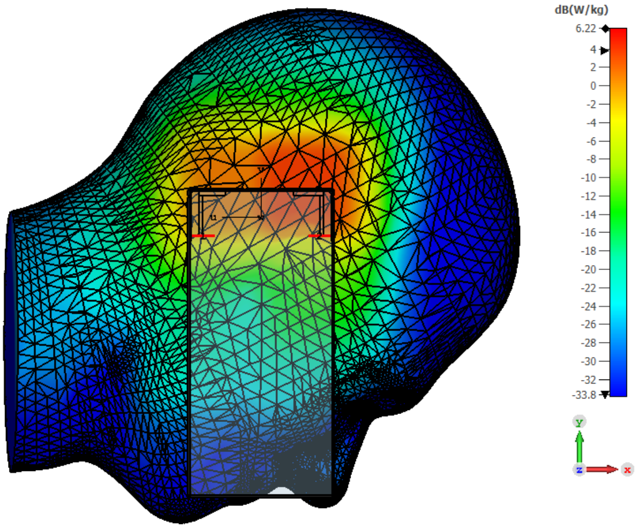

Figure A.1: Local 10 g averaged SAR distribution of the Bezel antenna for the Cheek position.

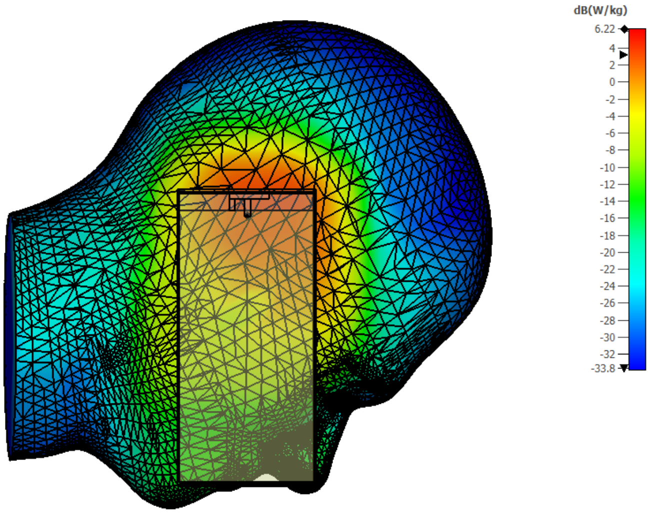

Figure A.2: Local 10 g averaged SAR distribution of the IFA for the Cheek position.

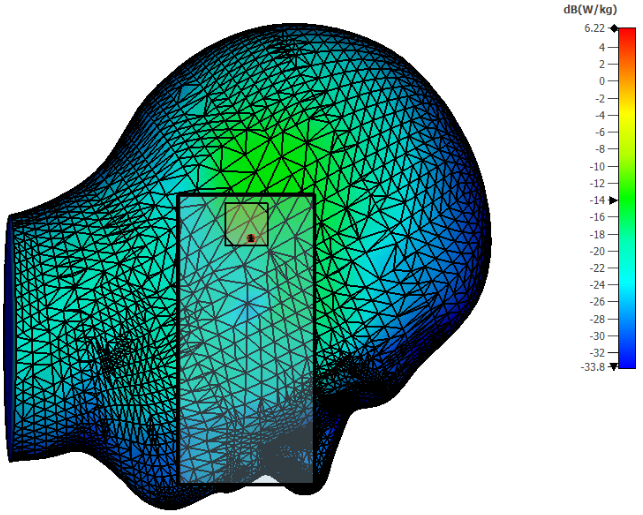

Figure A.3: Local 10 g averaged SAR distribution of the CP patch antenna for the Cheek position.

Found here in figure A.4 through A.6 are the SAR distributions for the back and top position for the Bezel antenna. Figures A.4 and A.6 are shown for the 10 g averaged SAR while figure A.5 is shown for 1 g averaged SAR, as per the limits. All figures show an adequate decay of the SAR, reaching values below −20 dB from the peak SAR found in the proximity of the antenna elements.

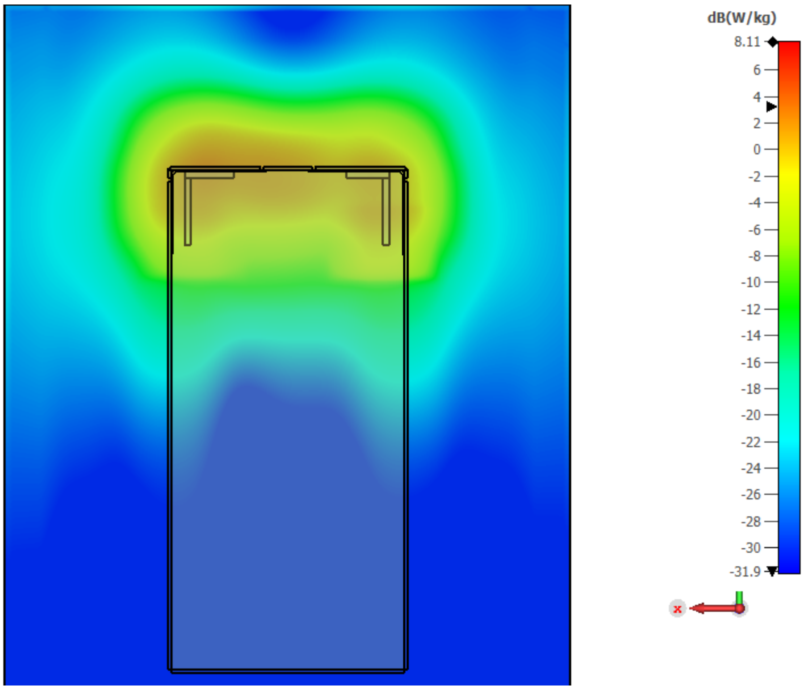

Figure A.4: Local 10 g averaged SAR distribution of the Bezel antenna for the back position with 0 mm separation.

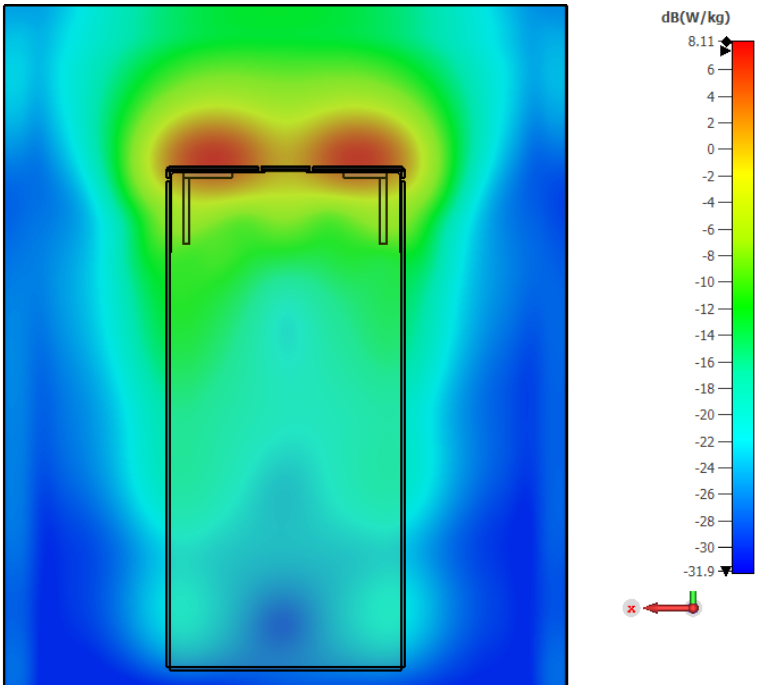

Figure A.5: Local 1 g averaged SAR distribution of the Bezel antenna for the back position with 5 mm separation.

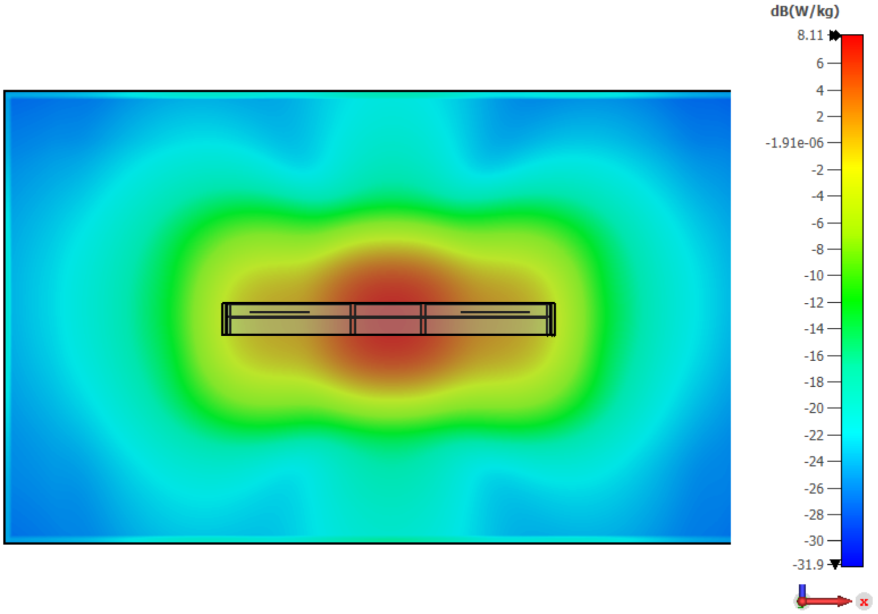

Figure A.6: Local 10 g averaged SAR distribution of the Bezel antenna for the bezel position.

Found here in figure A.7 through A.9 are the SAR distributions for the back and top position for the IFA. Figures A.7 and A.9 are shown for the 10 g averaged SAR while figure A.8 is shown for 1 g averaged SAR, as per the limits. All figures show an adequate decay of the SAR, reaching values below −20 dB from the peak SAR found in the proximity of the antenna elements.

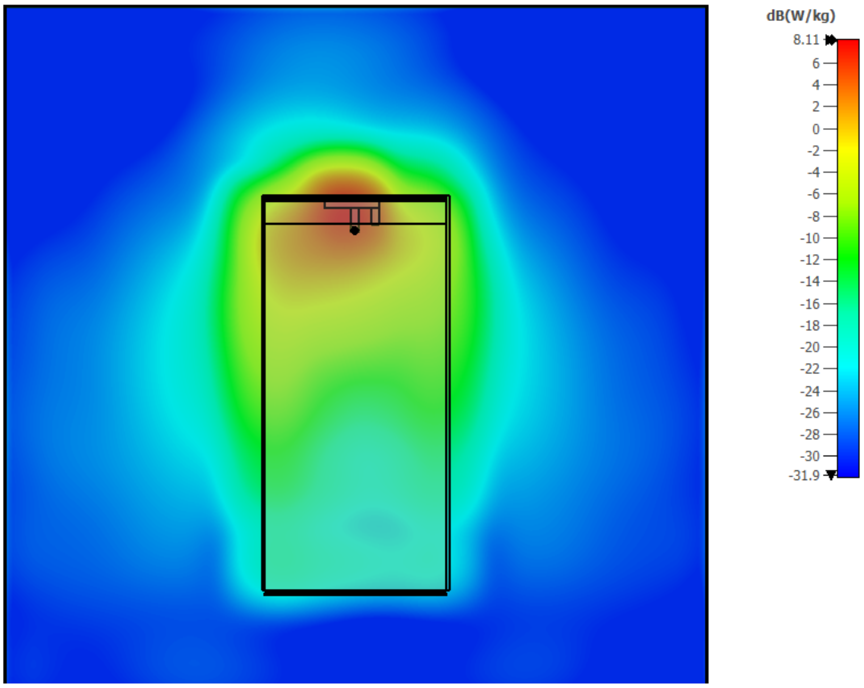

Figure A.7: Local 10 g averaged SAR distribution of the IFA for the back position with 0 mm separation.

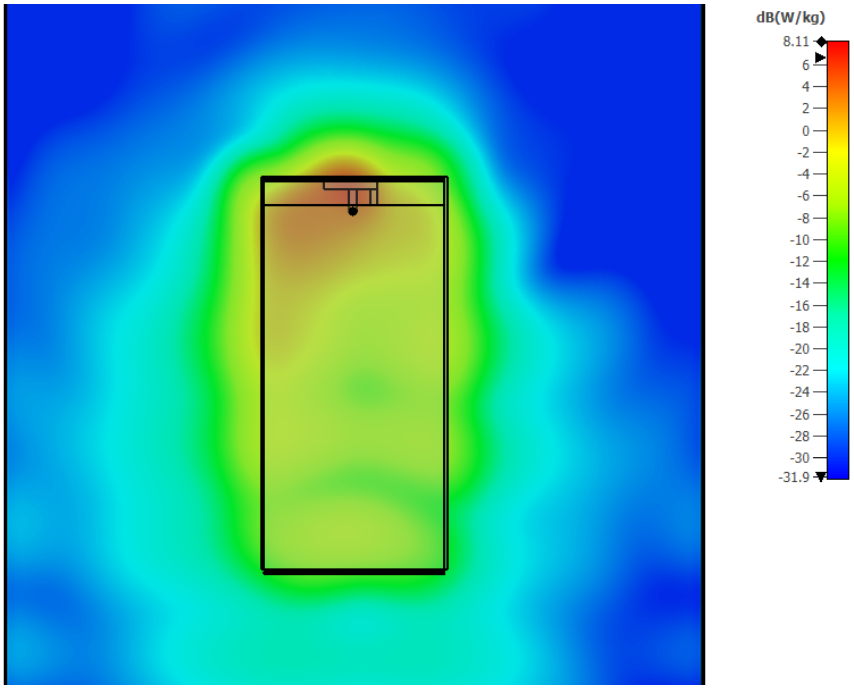

Figure A.8: Local 1 g averaged SAR distribution of the IFA for the back position with 5 mm separation.

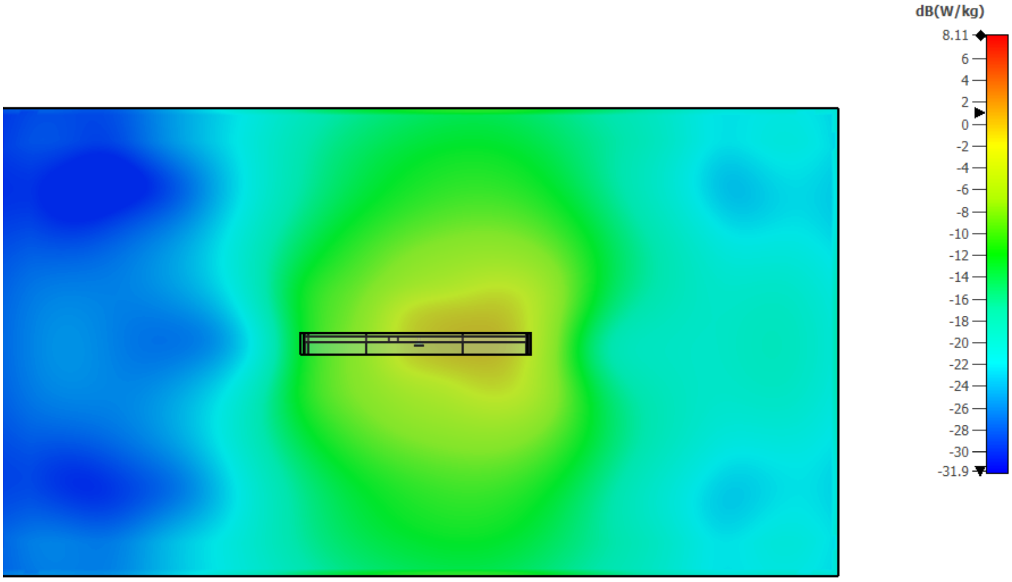

Figure A.9: Local 10 g averaged SAR distribution of the IFA for the top position.

Found here in figure A.10 through A.12 are the SAR distributions for the back and top position for the CP patch antenna. Figures A.10 and A.12 are shown for the 10 g averaged SAR while figure A.11 is shown for 1 g averaged SAR, as per the limits. All figures show an adequate decay of the SAR, reaching values below −20 dB from the peak SAR found in the proximity of the antenna elements. Notable is that in figure A.12, the phantom used is of different dimensions compared to the others to account for the broadside beam, thus extending further in the same direction. While this does not reach values that have decayed by more then −20 dB, the values across the entire phantom are in the equivalent range.

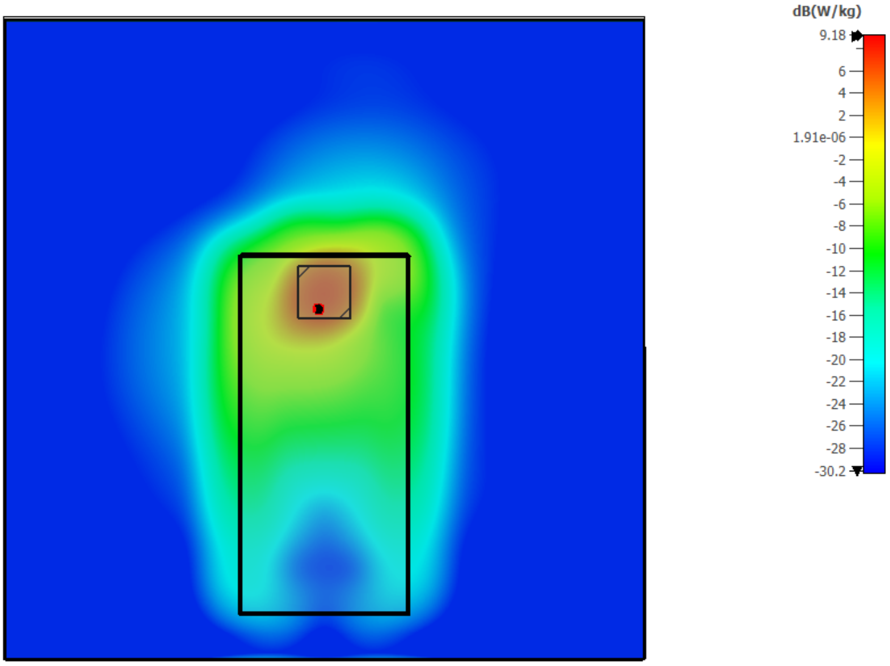

Figure A.10: Local 10 g averaged SAR distribution of the CP patch antenna for the back position with 0 mm separation.

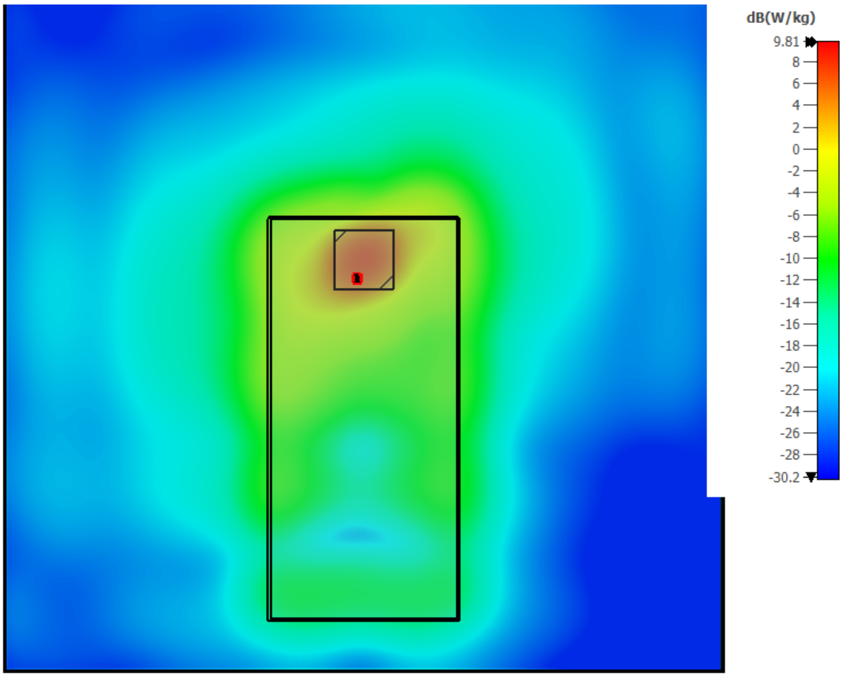

Figure A.11: Local 1 g averaged SAR distribution of the CP patch antenna for the back position with 5 mm separation.

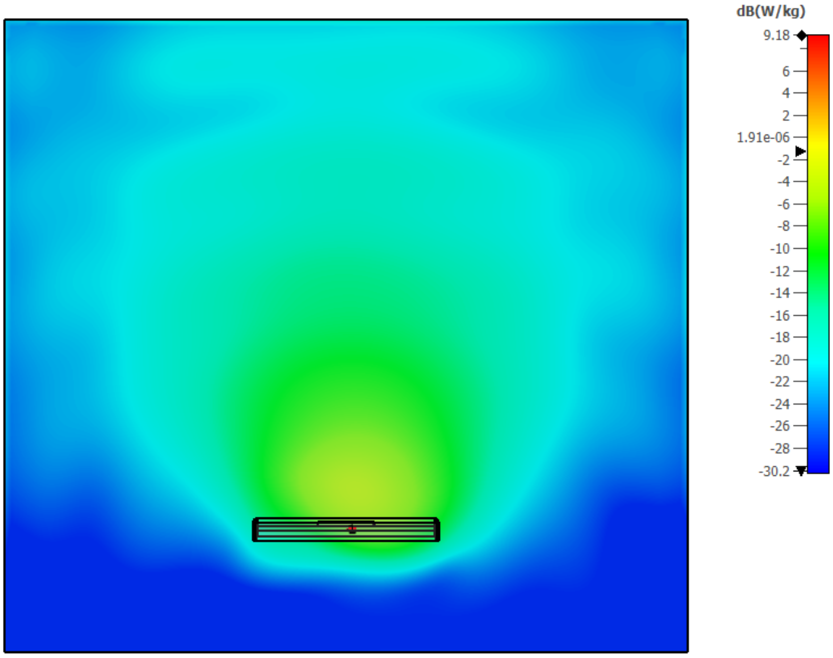

Figure A.12: Local 10 g averaged SAR distribution of the CP patch antenna for the bezel position.

DEPARTMENT OF ELECTRICAL ENGINEERING
CHALMERS UNIVERSITY OF TECHNOLOGY
Gothenburg, Sweden
www.chalmers.se

CHALMERS
UNIVERSITY OF TECHNOLOGY